INVESTIGATION OF LATERAL FORCES IN DYNAMIC MODE USING COMBINED AFM/STM

A DISSERTATION SUBMITTED TO

THE DEPARTMENT OF PHYSICS

AND THE INSTITUTE OF ENGINEERING AND SCIENCE

OF BILKENT UNIVERSITY

IN PARTIAL FULFILLMENT OF THE REQUIREMENTS

FOR THE DEGREE OF

DOCTOR OF PHILOSOPHY

By

MEHRDAD ATABAK

September, 2007

I certify that I have read this thesis and that in my opinion it is fully adequate, in scope and in quality, as a dissertation for the degree of doctor of philosophy.

Prof. Dr. Ahmet Oral (Supervisor)

I certify that I have read this thesis and that in my opinion it is fully adequate, in scope and in quality, as a dissertation for the degree of doctor of philosophy.

Prof. Dr. Şefik Süzer

I certify that I have read this thesis and that in my opinion it is fully adequate, in scope and in quality, as a dissertation for the degree of doctor of philosophy.

Assoc. Prof. Dr. Oğuz Gülseren

I certify that I have read this thesis and that in my opinion it is fully adequate, in scope and in quality, as a dissertation for the degree of doctor of philosophy.

Assist. Prof. Dr. Hakan Özgür Özer

I certify that I have read this thesis and that in my opinion it is fully adequate, in scope and in quality, as a dissertation for the degree of doctor of philosophy.

Assist. Prof. Dr. Ceyhun Bulutay

Approved for the Institute of Engineering and Science:

Prof. Dr. Mehmet B. Baray
Director of the Institute

ABSTRACT

INVESTIGATION OF LATERAL FORCES IN DYNAMIC MODE USING COMBINED AFM/STM

MEHRDAD ATABAK
PhD in Physics
Supervisor: Prof. Dr. Ahmet Oral
September, 2007

In this Ph.D. work, we constructed a fiber optic interferometer based non-contact Atomic Force Microscope (nc-AFM) combined with Scanning Tunneling Microscope(STM) to study lateral force interactions on Si(111)-(77) surface. The interferometer has been built in such a way that its sensitivity surpasses that of the earlier versions used in normal force measurements. The improvement in the resolution of the interferometer has allowed us to use sub-Angstrom oscillation amplitudes to obtain quantitative lateral force measurements. We have observed single and double atomic steps on Si(111)-(77) surface in topography and lateral stiffness images. This information allowed us to measure the lateral forces directly and quantitatively. We have also carried out lateral force-distance spectroscopy experiments, in which we simultaneously measured the force gradient and tunneling current, as the sample is approached towards the tip. The lateral force?distance curves exhibit a sharp increase of the force gradient, just after the tunnel current starts to increase, while the sample is approaching to the tip. We observed only positive force gradients.

In separate experiments, we imaged the Cu-TBPP molecules deposited on Cu(100) surface in normal and torsional mode in dynamic force microscope using STM feedback, with a homemade tungsten cantilever. Our experiments have shown the possibility of manipulating molecules on surface using a vibrating cantilever. However the forces involved in these experiments are not quantitatively measured due to limitations of the method.

Keywords: Scanning Probe Microscopy, Scanning Tunnelling Microscopy, noncontact Atomic Force Microscope, Cantilever, Lateral noncontact Force Microscopy, Fiber Interferometer.

ÖZET

YATAY KUVVETLERİİN DİNAMİK KİPTE ATOMİK KUVVET MİKROSKOBU/TARAMALI TÜNELLEME MİKROSKOBU İLE İNCELENMESİ

MEHRDAD ATABAK
Fizik, Doktora
Tez Yöneticisi: Prof. Dr. Ahmet Oral
Eylul, 2007

Bu doktora çalışmasında uç ile yüzey arası yatay kuvvetleri küçük genlikle titreştirerek ölçebilen fiber optik interefrometre kullanan Yüzeye Değmeden Atomik Kuvvet Mikroskobu (YD-AKM)/Taramalı Tünelleme Mikroskobu(TTM) imal edilerek, bununla Si(111)-(7×7) yüzeyinde yatay kuvvetler incelenmiştir. Geliştirilen interferometre daha önce dik kuvvet ölçmede kullanılana göre çok daha hassastır. Elde edilen bu yüksek ölçüm hassasiyeti nedeniyle yay Angstrom alti genliklerle titreştirilerek yatay uç-yüzey etkileşimleri nicemsel olarak ölçülebilmiştir. Si(111)-(7×7) yüzey topografi ve yatay esneklikte görüntülerinde tek ve çift atomik basamakları nicemsel olarak gözlenmiştir. Uç yüzeye yaklaştırılarak uç-yüzey yatay yay etkileşim yay sabiti ve tünel akımı uzaklığın fonksiyonu olarak ölçülmüştür. Yatay yay sabitinde tunel akımından sonra hızlı bir yükselme gözlenmiştir. Deneylerimizde yalnızca pozitif yatay yay sabiti gözlenmiştir.

Diğer deneylerimizde ise yatay kuvvetleri yayın bükülmesini ölçerek çalışan bir dinamik kuvvet mikroskobu ve elde yapılan bir tungsten yay kullanılarak Cu-TBPP moleküllerininin Cu(100) yüzeyi ile olan etkileşimleri incelenmiştir. Deneylerimiz Cu-TBPP moleküllerininin titreıen yay kulllanılarak Cu(100) yüzeyinde hareket ettirilebileceğini göstermiştir. Fakat Basel Üniversitesindeki bu düzenek ile bu kuvvetleri nicemlendirmek mümkün olamamıştır.

Anahtar sözcükler: Taramalı Uç Mikroskobu, Taramalı Tünelleme Mikroskobu, yüzeye değmeden Atomik Kuvvet Mikroskobu, yay, yatay yüzeye değmeden Atomik Kuvvet Mikroskobu, fiber intereferometre.

Acknowledgement

It is my pleasure to express my deepest gratitude to my advisor Prof. Dr. Ahmet Oral for his guidance, moral support, friendship and assistance during my Ph.D. thesis. I am indebted for his efforts and enthusiasm. I also express my deep appreciation to Dr. Özgür Özer who made me familiar with Ultra High Vacuum techniques and Atomic Force Microscopy while I was his assistant during his Ph.D. work.

I would like to thank the members of my Ph.D. dissertation committee for reading the manuscript and commenting on the thesis.

I would like to thank our group members Münir Dede, Dr. Özhan Ünverdi, Sevil Özer, and Aslı Elidemir, Dr. Rizwan Akram, for creating a fruitful, enjoyable, and unique working environment. I would like to acknowledge NanoMagnetics Instrument Ltd., former and current company members, Muharram, Göksel, Özge, Özgür, Volkan, Koray, for close collaboration and assistance whenever I needed.

I also would like to acknowledge ESF Nanotribo Program and Prof. Ernst Meyer to give me the opportunity to perform series of experiment in University of Basel, Switzerlands.

I would like to express my spacial thanks to Aşkin Kocabaş for his enthusiasm to create scientific discussions, and supplying me an extra pair of hands in my difficult times during experiment preparation. I also thank to Seçkin for helping my to model the Fabry-Perot interferometer. I would like to thank Dr. Aykutlu Dânâ for his valuable comments on my experiments. I appreciate the help of the physicist Murat Güre and the technician Ergün Karaman.

I am indebted to my family for their continuous support, care, and encouragement.

And finally, I thank my dearest *Mehrnaz*, as she means so much for me. I would like to devote this work to her and my family.

Contents

List of Figures

Chapter 1

Introduction

1.1 Overview

Technology today is an essential part of our economic, physical and social environment, and its importance will continue to grow. Within the past 30 years, the transformation of scientific knowledge into commercial products has reached a pace unimaginable in the 1960s. A prominent example illustrating this transfer of basic scientific knowledge in to industry is the laser, which was invented in 1958. It has transformed our lives from medicine to the DVD players. The inventions of Scanning Tunnelling Microscope(STM) [1, 2] in 1982 and Atomic Force Microscope(AFM) [3, 4] in 1986 have also opened a new phase in surface science, helping scientists to solve longstanding problems on the atomic structure of surfaces. STM is not only a surface imaging technique; it also presents the possibility of interacting with the surface of a sample at the atomic scale, by manipulating atoms and molecules on the specimen. A number of different systems have been investigated at low temperature, room temperature, ultra high vacuum, high pressures etc. The ability of a STM to interact with surfaces has lead to attempts to reduce the size of electronic components to the atomic scale using the STM to etch surfaces, and produce, for example, single electron transistors. More recently, STM has been used to investigate the quantization of

charge through single atom contacts at low temperatures [6]. While STM has enabled the surfaces of many materials to be imaged and manipulated. There are still some questions are still unanswered. The role of forces in STM imaging was indicated by the observation of anomalous corrugation heights on close packed metal surfaces [12] and the reduction of the measured apparent tunnel barrier heights. Clearly, manipulation of adsorbates on a surface requires a force to move the adsorbate. However, the theoretical description of STM is based on the simple model proposed by Tersoff and Hamann [7, 8],which considers the overlap of the tip and surface wave functions, but ignores other interactions that might be occurring at short distances. The possible influence of van der Waals forces is not considered and the influence of attractive bonding forces is similarly ignored. Invention of the Atomic Force Microscopy (AFM) in 1985 by Binnig, Gerber and Quate [3] opened up the possibility of not only imaging surfaces using forces, but also measuring interaction forces directly. In its simplest form, AFM works by measuring the deflection of a lever due to the interaction between a sharp tip on the lever and the sample surface. The force on the lever is measured using the Hooke's Law. It has an advantage over the STM, because it can image both insulating and conducting surfaces. Different forces involved in the interactions have led to the development of a wide range of scanning probe techniques. Magnetic, electrostatic, friction and van der Waals forces can all be measured using a suitably prepared AFM cantilever. There are two basic operating modes for AFM, contact and noncontact mode. In contact mode AFM, the tip is in contact with the surface, and only the repulsive forces can be measured. Contact mode AFM has shown images with atomic scale corrugations on layered materials [71], but atomic scale defects were not observed. It was concluded that while the images had atomic periodicity, they were not true atomic resolution [11]. In noncontact AFM(nc-AFM), attractive forces can be measured. Atomic resolution imaging in nc-AFM only came after Albrecht *et al.* [12] developed a new method of operating AFMs, called frequency modulation(FM). In this technique, the cantilever is kept oscillating at the resonant frequency and a frequency demodulator measures the change in frequency shift due to tip-sample forces. This method increased the sensitivity of the measurements, without reducing the measurement bandwidth. The first atomic resolution nc-AFM image was taken on Si(111)-(7x7) surface by

Giessibl [13] in 1995 using this technique.

With the advent of the Atomic Force Microscopy it also became possible to study lateral forces between the tip of a force microscope and atomic-scale features on the surface of a sample. Although the surface force apparatus(SFA) [59] and the Quartz-Crystal Microbalance(QCM) [5] are accurate enough to measure forces down to the scale of atomic friction, they suffer from the limitation of comparatively large areas of contact, typically of several square micrometers or more. Both instruments trace the forces that arise during the collective motion of such large contacts. Whereas AFM allows nanoscale or atomic scale force measurements, After the invention of AFM, Mate and colleagues quickly adapted the AFM to measure lateral forces and they demonstrated the atomic-scale stick-slip motion of a sharp tungsten tip over a Highly Oriented Pyrolytic Graphite (HOPG) surface [14]. On the atomic scale, the tip apex moved over individual rows of carbon atoms and dissipated energy much like playing the strings of a guitar. This experiment initiated a new approach in nanotribology.

1.2 The Aim of the Dissertation

The main aim of the dissertation was to build a flexible scanning tunnelling and atomic force microscope which is capable of performing quantitative lateral and normal force as well as tunnelling measurements. The ultimate goal of building this apparatus is the measurement of forces while manipulating molecules or atoms across the sample surface. To achieve this goal, the we use sub-Ångstrom oscillation amplitudes. This would mean that the either lateral or normal force gradients acting on the tip could be easily measured, since there is a simple relation between the measured change in the lever's oscillation amplitude and the force gradient acting on the tip. Although the calculations by Perez and coworkers [15, 16] show that the contrast seen in nc-AFM atomic resolution images of Si(111)-(7x7) was due to a short range vertical covalent bonding type interaction, there is no theoretical report about the behavior of tip-sample forces in simultaneous STM and non contact lateral force AFM. This thesis is devoted to the

construction of lateral nc-AFM using small oscillation amplitudes to investigate the lateral forces quantitatively. These measurements will provide new insight for the lateral interaction forces of individual bonds. This apparatus can shed light into forces involved in atomic manipulation experiments. The rest of the thesis is arranged as follows:

Chapter 2 gives a review of the progress made to date in the fields of STM and AFM, highlighting the developments in atomic resolution imaging and force measurements,atomic and molecular scale manipulation. In this chapter, challenges in the field of nanotribology and atomic scale lateral force measurements, are also reviewed.

Chapter 3 gives details of the design, construction and development of the new combined STM and dual fibre interferometer based AFM. Noise in the instrument is analyzed and the progress to reduce the noise level is explained and to improve the sensitivity of the instrument. Chapter 4 presents the results achieved in lateral AFM atomic resolution imaging using small oscillation amplitudes on the Si(111)-(7x7) surface as well as lateral force-vertical distance spectroscopy made with the apparatus. In addition, the results of lateral force in investigation of molecules on Cu(111) will be presented. In chapter 5 conclusions are drawn from the work presented and further work is proposed.

Chapter 2

Background

Nanoscience has developed extremely fast in the last two decades. Scanning Probe Microscopes have helped its progress. Electronic devices on the nanometer scale are expected to replace those on the micrometer scale, with their faster response times and smaller volumes. Scanning Tunnelling Microscopy has been proven to be a key tool in nanodevice technology. It has been widely used to investigate the manipulation of single atoms, image atomic scale defects, sub-monolayer epitaxy processes etc. Moreover, it has also been used for atomic manipulation at liquid-helium temperatures. In 1990 Don Eigler manipulated Xe atoms on a substrate with single atoms by using an STM tip [17]. Since then, many other scientists have performed atomic manipulation experiments on various surfaces. In one of the recent works Fishlock *et al.* have shown that it is possible to move alkaline atoms on a copper surface even at room temperature using the STM tip like a cue directing billiard balls [18].

Although STM has been used very effectively in atomic manipulation processes, there were problems in controllably positioning atoms on surfaces. In manipulation with STM, as in the experiment done by Eigler *et al.* [19] with a Xe atom adsorbed on Ni(110) surface, the STM tip is first positioned above the Xe atom to move the adsorbed atom along the substrate surface. The force interaction between the tip and the atom, which is due to van der Waals forces,

is increased by approaching the tip towards the atom. The appropriate adjustment of the tip-adsorbate force interaction for the sliding process is critical. On the one hand, this interaction has to be strong enough for the adsorbed atom to overcome the lateral forces so that it can move to other lattice sites. On the other hand, the tip-adsorbate interaction has to be kept considerably smaller than the adsorbate-substrate interaction in order to prevent transfer of the adsorbate from the substrate to the tip. Hence, one needs to measure the force interaction in such a system to reliably control the manipulation process. It is necessary to understand the underlying mechanisms of manipulation, measure the forces between the probe tip and adsorbate atoms and to have an idea on the frictional forces. With these requirements, Atomic Force Microscopy has come into the stage, with its capability of measuring forces between the tip and surface atoms.

The invention of AFM in 1986 mainly come from the argument that forces play an important role in the STM imaging. Especially, on close packed metal surfaces such as Cu(111) and Al(111), and the layered materials like graphite the measured corrugation heights were almost ten times greater than the predicted value by theoretical studies. This deviation from the expected results were usually attributed to the existence of a strong force interaction between the tip apex and the surface atoms, causing some relaxation on either the tip or the sample atoms. A few years after the invention of STM, Binnig and coworkers came up with the idea of using the force itself to control parameter in such a scanning microscope and in 1986 constructed the first AFM [4].

2.1 Scanning Tunnelling Microscopy

The phenomenon of tunnelling has been known for more than eighty years-ever since the formulation of quantum mechanics. As one of the main consequences of quantum mechanics, a particle such as an electron, which can be described by a wave function, has a finite probability of entering a classically forbidden region. Consequently, the particle may tunnel through a potential barrier which separates two classically allowed regions. Tunnelling phenomena has been first proposed

by Oppenheimer [20] in 1928 as a result of his theoretical studies on the ionization of hydrogen atoms in a constant electric field. Esaki [21] and Giaver [22] were the first two scientists who observed electron tunneling experimentally in p-n junctions and in planar metal-oxide-metal junctions, respectively. Tunnelling of Cooper pairs between two superconductors was predicted by Josephson [23]. These three scientists shared the Nobel Prize in Physics in 1973, for their contributions to the investigation of tunnelling phenomena.

Devices such as Metal-Insulator-Metal (MIM) diodes, hot electron transistors, superconducting quantum interference devices(SQUID), which use tunnelling through an insulating barrier like oxides, were developed in 1970s. However, barriers such as oxides, do not permit either to change the width of the barrier or to reach the surface of each electrodes for surface investigations. In that respect vacuum tunnelling, which is the most important feature of scanning tunneling microscope, has certain advantages.

The predecessor of STM is the Topographiner developed by Young *et al.* [24]. The basic principle of this was the field emission. It is very similar to the scanning tunneling microscope as far as its operation is concerned, i.e. it uses a sharp tip and the scanning is achieved by piezoelectric translators. The field emission current is kept constant by adjusting the relative position of the tip to the surface. However the lateral and vertical resolutions were limited to 4000 Å and 30 Å respectively, due to relatively large distance between tip and surface of several hundred Å ngström, in the field emission regime.

Teague [25] and Poppe [26] have observed vacuum tunneling in 1978 and 1981 respectively. However Binnig and Rohrer were the first to use vacuum tunnelling for a microscope. In 1982 Binnig, Rohrer and coworkers [1,2] have constructed the first scanning tunnelling microscope by observing vacuum tunnelling on platinum samples with a tungsten tip. For this invention, Binnig and Rohrer shared the Nobel Prize in Physics in 1986 with Ruska.

Scanning Tunnelling Microscopy is a powerful and a unique tool for the investigation of structural and electronic properties of surfaces. In order to understand what is measured by STM and interpret the images, several theories were

developed by scientists. Before trying to understand the theory of STM, good understanding of the basic principles of vacuum tunnelling is necessary. In vacuum tunneling the vacuum region acts as a barrier to electrons between the two metal electrodes. In the case of STM, these electrons correspond to the surface and the tip. Fig.2.1 shows this potential barrier schematically. The transmission probability for a wave incident on a one-dimensional barrier can easily be calculated. The solutions of Schrödinger's equation inside a rectangular barrier in one dimension have the form

$$\psi = e^{\pm \kappa z} \tag{2.1}$$

$$\kappa^2 = \frac{2m(V_B - E)}{\hbar^2} \tag{2.2}$$

where E is the energy of the state, and V_B is the barrier potential . In general V_B may not be constant across the gap, but for the sake of simplicity let us assume a rectangular barrier. In the simplest case V_B is the vacuum level, so for states at the Fermi level, $V_B - E$ is just the work function.

The transmission probability, and hence the tunnelling current, decays exponentially with barrier width d as

$$I_t \propto e^{-kd} \tag{2.3}$$

For tunnelling between two metals with a given voltage difference V across the gap, only the states within eV above the Fermi level can contribute to the tunnelling. Other states cannot contribute either because there are no electrons to tunnel at higher energy, or because there is not any empty state to tunnel into at lower energy.

2.1.1 STM Imaging

The basic idea underlying STM is quite simple. As illustrated in Fig. 2.2 sharp tip is brought close enough to the surface. At a convenient operating voltage,

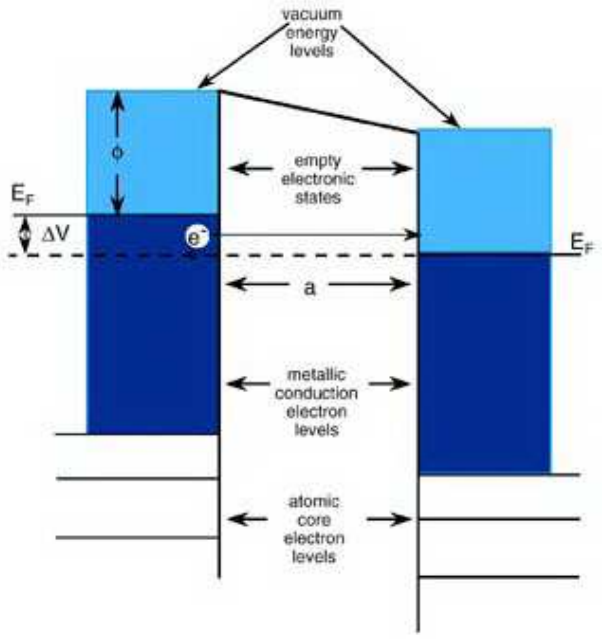

Figure 2.1: A one-dimensional tunnelling barrier.

typically 2 mV to 2 V, a measurable tunnelling current, typically between 0.1 nA and 10 nA, is obtained. There are basically two modes of operation of STM. The first and the mostly used one is the constant current mode, in which the tip is scanned over the surface, while the tunnelling current is kept constant by changing the vertical position of the tip with a feedback control circuit. The control circuit achieves this by applying suitable voltages to the z-Piezo. The applied voltage to the piezoelectric crystal simply gives the trajectory of the tip over sample. If a line scan in x-direction is extended to many lines in y direction, an image which consists of a map $z(x, y)$ of the tip position versus lateral position (x, y) is obtained. In the second mode, namely the constant height mode, the tip is kept nearly at a constant height during the scan and the tunnelling current is monitored. The control circuit only keeps the average current constant, I_t is plotted against (x, y) to form the image.

Each mode has its own advantages. Constant current mode can be used to scan surfaces which are not atomically flat. On the other hand, the constant height mode allows for much faster scanning of atomically flat surfaces, since only

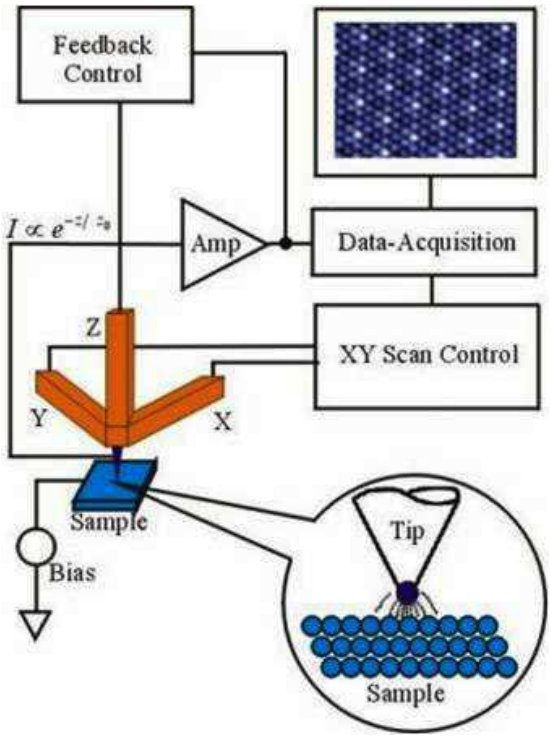

Figure 2.2: The schematic view of STM principle

the control electronics, not the z-Piezo, must respond to the structure passing under the tip. Fast imaging is important in certain application where researchers can study processes in real time, minimizing image distortion due to piezoelectric creep and thermal drift.

2.1.2 Theory of STM

If the resolution of STM is of the order of a few Ångstrom or larger, it is adequate to interpret the image as a surface topograph. However, if the concern is on atomic resolution images, it is not even clear what is meant by a topography. The most reasonable definition is that the topography is a contour of constant charge density from Tersoff-Hamann theory. This contradicts the principle of vacuum tunnelling which says only the electrons near the Fermi level contribute to tunnelling, even though all the electrons below the Fermi level contribute to the

charge density. The following theory developed by the Tersoff and Hamann [7,8] is explanatory even in case of atomic resolution. In first order perturbation theory, the tunnelling current is

$$I = \frac{2\pi e}{\hbar} \sum_{\mu,\nu} \{f(E_\mu)[1 - f(E_\nu)] - f(E_\nu)[1 - f(E_\mu)]\} |M_{\mu\nu}|^2 \delta(E_\nu + V - E_\mu) \quad (2.4)$$

where $f(E)$ is the Fermi function, V is the applied voltage, $M_{\mu\nu}$ is the tunneling matrix element between states ψ_μ and ψ_ν of the respective electrodes, and E_μ is the energy of the state ψ_μ. For most of the purposes, the Fermi functions can be replaced by their zero-temperature values which are unit step functions. In this case, the above equation, in the limit of small voltage, reduces to

$$I = \frac{2\pi}{\hbar} e^2 V \sum_{\mu,\nu} |M_{\mu\nu}|^2 \delta(E_\mu - E_F) \delta(E_\nu - E_F) \quad (2.5)$$

This equation is quite simple. The problem is to evaluate the tunneling matrix elements. Bardeen [27] showed that, under certain assumptions, the tunneling matrix elements can be expressed as

$$M_{\mu\nu} = \frac{\hbar^2}{2m} \int d\mathbf{S} \cdot (\psi_\mu^* \nabla \psi_\nu - \psi_\nu \nabla \psi_\mu^*) \quad (2.6)$$

where the integral is over any surface lying entirely within the barrier region. If we choose a plane for the surface of integration, and neglect the variation of the potential in the region of integration, then the surface wave function at this plane can be conveniently expanded in the generalized plane-wave form

$$\psi = \int d\mathbf{q} a_\mathbf{q} e^{-\kappa_q z} e^{i\mathbf{q}\cdot\mathbf{x}} \quad (2.7)$$

where z is height measured from a suitable origin at the surface, and

$$\kappa_q^2 = \kappa^2 + |\mathbf{q}|^2 \quad (2.8)$$

A similar expansion applies for the other electrode, replacing $a_\mathbf{q}$ with $b_\mathbf{q}$, z with $z_t - z$, and $\mathbf{x}$ with $\mathbf{x} - \mathbf{x}_t$. Here $\mathbf{x}_t$ and z_t are the lateral and vertical components of the position of the tip, respectively. Then, substituting these wave functions into Eq. 2.6, the matrix elements can be obtained as

$$M_{\mu\nu} = -\frac{4\pi^2\hbar^2}{m} \int d\mathbf{q} a_\mathbf{q} b_\mathbf{q}^* \kappa_q e^{-\kappa_q z_t} e^{i\mathbf{q}\cdot\mathbf{x}_t} \quad (2.9)$$

Thus given the wave functions of the surface and tip, a simple expression for the tunnelling matrix element and tunnelling current can be found. However, the atomic structure of the tip is generally not known. What would be the criteria in the estimation of the atomic structure of the tip. There are two important points to be considered in this respect. First, the aim is maximum possible resolution, hence the smallest possible tip. Therefore, the ideal STM tip would consist of a mathematical point source of current, whose position is denoted $\mathbf{r}_t$. In that case, Eq. 2.8 for the tunneling current reduces to [27, 28]

$$I \propto \sum_{\nu} |\psi_\nu(\mathbf{r}_t)|^2 \delta(E_\nu - E_F) \equiv \rho(\mathbf{r}_t, E_F). \tag{2.10}$$

Thus the ideal STM would simply measure $\rho(\mathbf{r}_t, E_F)$, namely the local density of states at E_F(LDOS). LDOS is evaluated for the bare surface. It doesn't depend on the complex tip-sample system. The only dependence related to the tip is its position. However, Tersoff-Hamann Theory is valid only for large tip-sample separations. For small separations, a detailed analysis of the tip sample interaction is necessary, in order to interpret the images. Because interaction is strong enough to affect the measurements. Various studies on this subject [28, 30, 31] have shown that the complex interacting system of the tip and the sample affects the corrugation amplitude.

2.1.3 Scanning Tunnelling Spectroscopy

Scanning tunneling spectroscopy provides information complementary to the information obtained in conventional STM topographic imaging. By measuring the detailed dependence of the tunnelling current on the applied voltage at specific locations of the sample, it is possible to obtain a measure of the electronic density of states of the sample on an atomic scale. If both the energies and the spatial locations of the electronic states are known, direct comparisons with the theory can be made. However, a general theory for the use of STM for the spectroscopy of electronic surface states has not yet been developed. Since the electronic states of the tip and their interaction with the sample surface have to be considered for each sample-tip combination, the evaluation of a general theory is quite difficult.

Tunneling spectroscopy in planar junctions was studied long before STM [34]. However, the development of spatially-resolved spectroscopy with STM stimulated the interest in this area. Because of the difficulty of calculating tunneling current $I(\mathbf{r}_t, V)$ in general, the studies mostly focused on $I(V)$, without considering the dependence to the position of the tip. Selloni *et al.* [33] suggested that the results of Tersoff and Hamann [8] could be qualitatively generalized for modest voltages as

$$I(V) \propto \int_{E_F}^{E_F+V} \rho(E)\, T(E,V)\, dE, \tag{2.11}$$

where $T(E,V)$ is the barrier transmission coefficient, and $\rho(E)$ is the local density of states given by Eq. 2.10 at or very near the surface, and assuming a constant density of states for the tip. However, this simple model does not come up with a straightforward interpretation for the tunnelling spectrum [32]. In particular, the derivative dI/dV has no simple dependence on the density of states $\rho(E_F + V)$. It can be said that a sharp feature in the density of states of the sample (or tip), at an energy $E_F + V$, will lead to a feature in $I(V)$ or its derivatives at voltage V. However, there is a problem with the statements above. The problem is the strong voltage-dependence of the transmission coefficient, $T(E,V)$, which results in a distortion of features in the spectrum [33]. Stroscio, Feenstra, and coworkers [35] proposed a simple solution to this problem. To eliminate the exponential dependence of $T(E,V)$ on V, they normalize dI/dV by dividing it by I/V. Therefore the quantity $d\ln I/d\ln V$ is mostly used for identification of density of states in the STM results.

There is an important problem in tunnelling spectroscopy studies. The electronic density of states of the tip is usually unknown, so it is not so simple to extract the knowledge of the electronic structure of the surface from the spectroscopy measurements. This problem can be overcome by using the same tip, consequently having a constant background during all measurements. In accordance with the modes of STM imaging, there are various types of scanning tunnelling spectroscopy. These are constant current, constant separation, and variable separation spectroscopy. In constant current spectroscopy, tracing the bias voltage in the specified interval, typically between two values symmetric with respect to zero is necessary, the zero value of the voltage causes the tip to crash

into the sample. Therefore, this mode is experimentally difficult to perform. Constant separation spectroscopy is experimentally most preferred one. At a constant separation, the applied voltage is varied over the specified interval while simultaneously measuring the tunnelling current. However, in order to correlate the tunnelling spectra with the topograph of the surface, the spectroscopy must be carried out simultaneously with the topographic imaging. This was first achieved experimentally by Hamers *et al.* [36], and called spatially resolved spectroscopy. Spatially resolved spectroscopy is more complex and experimentally more difficult to achieve, not only because of the necessity of a more complicated control circuit, but due to the need for very stable STM tips, which are very difficult to prepare.

2.1.4 STM on Semiconductors

Scanning Tunnelling Microscope can be used to image only metals, semiconductors, and doped insulators, since its operating principle is the tunnelling of electrons. Since its invention, STM has became a widely used instrument to investigate semiconductor surfaces. This is not just because of the power of STM or the necessity to investigate the topographic and electronic properties of these surfaces on an atomic scale, but due to a property of these surfaces that makes them very suitable samples for STM measurements. This property is the reconstruction of bulk terminated semiconductor surfaces. Reconstruction of the surface results in large corrugation on the surface, as large as a few Å. These large corrugation amplitudes are very easy to detect with STM and can easily be converted into an illustrative gray scale STM image. There are other features of semiconductor surfaces, such as dimers and steps, which have relatively larger scales, that can also be easily resolved. On the other hand, the reconstructed semiconductor surface may exhibit considerable local differences in the electronic structure. .

In the last 30 years, semiconductor technology has continued its fast progress. Silicon based integrated circuits have been developed with extremely high yield. However, the technological thirst for faster and smaller devices enforces scientific

research on semiconductors. SiGe and GaAs heterostructures have begun to form the basis of high-speed semiconductor technology. It is well understood that, to increase the quality and speed of heterostructure based devices, very thin layers, sometimes only a few monolayers of atomic structures are necessary. This can be achieved with Molecular Beam Epitaxy and related techniques . However, almost all semiconductor surfaces contain single steps separated by a few hundreds of Ångström. Thus without processing of the surface, it is impossible to obtain atomically flat layers having homogenous thicknesses. This problem brings the necessity to investigate the semiconductor surfaces and epitaxial growth at an atomic level. The aim is to decrease the number of steps, which will allow homogenous growth of layers on substrates. By using STM it is possible to observe the mechanisms of growth, and to understand the growth conditions giving the best surfaces. By association of MBE and STM systems, even real-time images of epitaxial growth can be acquired [38].

2.2 Atomic Force Microscopy

Atomic Force Microscope is invented by Binnig,Gerber and Quate in 1986 as a tool for studying insulating and conducting surfaces. Basic ingredients of an Atomic Force Microscope is shown in Figure 2.3. In fact, the concept of using a force to image a surface is a general one, and can be applied to magnetic and electrostatic forces as well as the interatomic interaction between the tip and the sample. Whatever the origin of the force, all force microscopes have five essential components:

i)A sharp tip integrated to a cantilever spring,

ii)A way of sensing the cantilever deflection,

iii) A feedback system to keep an the deflection at constant level,

iv) A mechanical scanning system (usually piezoelectric crystal based system),

v) A control and image acquisition system that converts the measured data

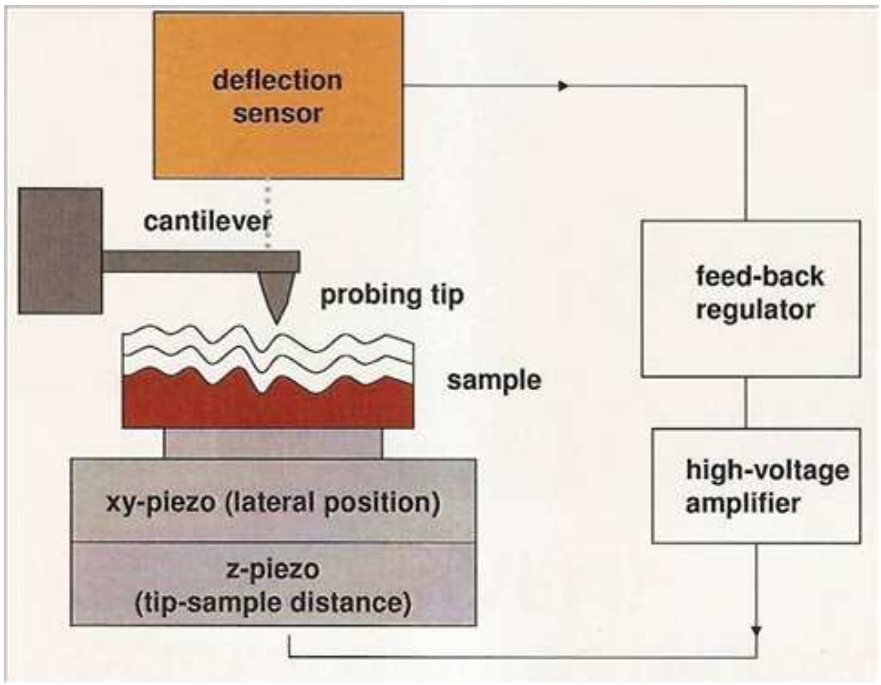

Figure 2.3: The schematic view of an Atomic Force Microscope.

into an image.

The scanning, feedback and display systems are very similar to those used for STM. An AFM can be operated in three modes: contact mode, non-contact mode and intermittent-contact mode. Figure 2.4 shows the operation regions. In contact mode, the tip is in contact with the sample, and repulsive forces between the tip and sample are measured. The total tip-surface force is the sum of both large range van der Waals (vdW) and short range chemical interactions. For distances below 2 Å, the chemical interaction is dominated by the Pauli repulsion and starts to balance the attractive vdW force. Atomic resolution images of layered material such as graphite and boron nitride have been reported [40] but the images do not show individual surface defects, which are routinely observed with the STM. Furthermore, these images persist at large forces (100 nN), where the contact area is predicted to be of the order of 100 $Å^2$. These results suggest that both tip and sample are deformed by the repulsive interaction and that the tip is far from being single atom tip which needed for real atomic resolution. The

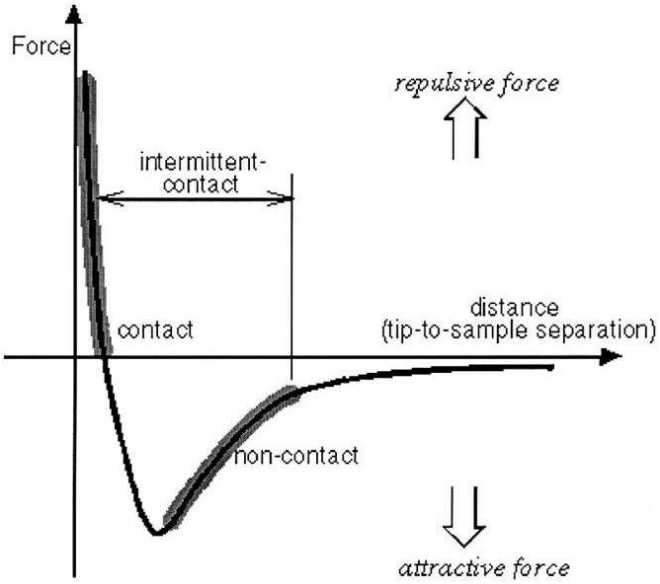

Figure 2.4: Interatomic force vs. distance

tip-sample force gradient results in a modification of the effective spring constant of the cantilever. In non-contact AFM mode, the tip is not in contact with the sample, and long-range interaction forces, e.g. vdW, electrostatic, and magnetic force can also be probed. Unlike the contact mode, this method is sensitive to force gradient, rather than the interaction forces between tip and sample. The cantilever is driven to vibrate at its resonance frequency by means of a piezo-electric element, and changes in the resonant frequency as a result of tip-sample interaction are measured. The force gradient between tip and sample, $F' = -\frac{\partial F_z}{\partial z}$, results in a modification of the effective spring constant of the cantilever

$$k_{eff} = k - F^{'} \tag{2.12}$$

where k is the spring constant of cantilever in the absence of tip-surface force interaction. An attractive tip-surface interaction with ($F^{'} > 0$) will therefore soften the effective spring constant ($k_{eff} < k$), whereas a repulsive tip-surface force interaction ($F^{'} < 0$) will strengthen the effective spring constant ($k_{eff} > k$). The change of the effective spring constant, in turn, a shift in the resonant

frequency ω of the cantilever according to

$$\omega = (\frac{k_{eff}}{m})^{1/2} = [\frac{(k - F^{'})}{m}]^{1/2} = (\frac{k}{m})^{1/2}(1 - \frac{F^{'}}{k})^{1/2} = \omega_0(1 - \frac{F^{'}}{k})^{1/2} \quad (2.13)$$

where m is an effective mass and ω_0 is the resonance frequency of the cantilever in the absence of force gradient. If $F^{'}$ is small relative to k then the Eq. (2.12) can be approximated by

$$\omega \approx \omega_0(1 - \frac{F^{'}}{2k}) \quad (2.14)$$

and therefore

$$\frac{\Delta\omega}{\omega_0} \approx -\frac{F^{'}}{2k} \quad (2.15)$$

and attractive force ($F^{'} > 0$) will therefore lead to a decrease of the resonant frequency ($\omega < \omega_0$), whereas a repulsive force ($F^{'} < 0$) will lead to an increase ($\omega > \omega_0$). The above approximation can be to applied to small cantilever oscillation amplitude A, compared to the length scale of the tip-surface interaction force. However most non-contact AFMs operate at very large oscillation amplitudes, 1-60 nm!. If the maximum restoring force is greater than the maximum attractive force, $kA \gg F_{max}$, and the cantilever is driven at its resonance frequency with large oscillation amplitude, the shift of resonance frequency $\triangle\omega$ can be described by the following perturbation equation:

$$\frac{\triangle\omega}{\omega_0}kA = \oint \frac{d\varphi}{2\pi}F(\overline{z} + Acos\varphi)cos\varphi \quad (2.16)$$

where the force F is integrated over one oscillation cycle and $\overline{z}$ is the time averaged position of the tip.

Different methods are used for measurement of the resonance frequency shift, Δf. A method which is called slope detection method, the cantilever is driven by means of a piezoelectric element with a typical amplitude at the tip on the order of 1-10 nm at a determined frequency ω_d, the amplitude change or phase shift of the vibration as a result of the tip-surface force interaction is measured with the deflection sensor and a lock-in amplifier. A feedback loop adjusts the tip-surface separation by maintaining a constant force gradient. Another method which is proposed by Albrecht *et al.* [12] in 1991 is called frequency modulation (FM) technique, oscillation of the cantilever is maintained at resonance by

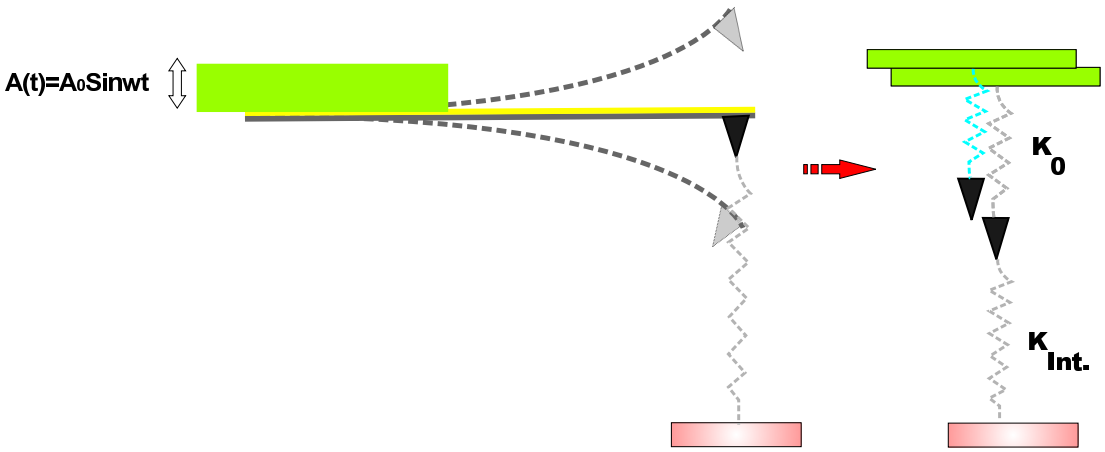

Figure 2.5: The schematic view of tip sample interaction in dynamic mode

a feedback loop using the signal from deflection sensor. Change in the oscillation frequency, caused by variations of the force gradient of the tip sample interaction, are directly measured by a frequency counter or FM discriminator. To achieve the highest possible detection sensitivity for a given free oscillation amplitude A_0, the cantilever should have a small spring constant k and a high resonance frequency f_0, in addition, a high Q-factor for the cantilever is desirable, which can only be achieved in the vacuum condition. Oral *et al.* [41] proposed a new method using sub-Ångstrom oscillation amplitude of the order of 0.25Å and below-resonance which enables the researchers direct measurement of force gradients acting on the tip due to tip- surface interaction. In this limit, the measurement is linear and quasi-static. This technique overcomes some of the limitations of the nc-AFMs, which use large amplitude frequency modulation techniques. While providing high resolution images these techniques have limitation to give quantitative spectroscopic data in atomic manipulation experiments and in measuring the nature of dissipative processes. This is because the measured parameter(frequency shift, Δf) is not related to the interaction energy or force in a simple manner at large oscillation amplitudes. Mathematical deconvolution is needed in order to extract the force, which relies on a number of assumptions such as the harmonic motion of the lever, a conservative interaction potential and general reversibility of the interaction. In small amplitude nc-AFM technique, the maximum possible energy

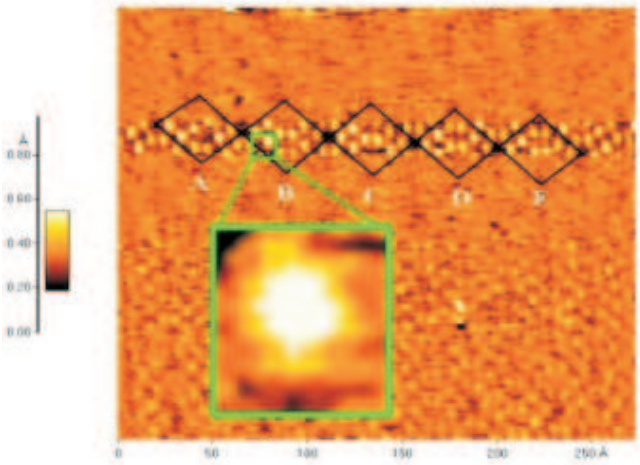

Figure 2.6: The first atomic resolution image obtained in UHV using nc-AFM. Image of Si (111)-(7×7) surface [13]

input into the tip-sample interaction region is of the order of only $10^{-3}eV$ per cycle as opposed to several eV in the case of large amplitude, resonance enhancement technique. In addition, a high Q-factor cantilever and vacuum condition is no longer a necessary, therefore this technique promises to explore and map the mechanics of matter at the nano-and atomic scale even in ambient condition and under liquids [42, 44].

In intermittent-contact atomic force microscopy, which is similar to nc-AFM, the cantilever tip is brought closer to the sample so that the bottom of its travel it just barely hits, or taps, the sample. In intermittent contact atomic force microscopy the cantilevers oscillation amplitude changes in response to tip-to-sample spacing similar to nc-AFM. An image representing surface topography is obtained by monitoring these changes. Some samples are best handled using IC-AFM instead of contact or non-contact AFM. IC-AFM is less likely to damage the sample than contact AFM, because it eliminates lateral forces (e.g. friction) between the tip and the sample. In general, it has been found that IC-AFM is more effective than nc-AFM for imaging larger scan sizes that may include greater variation in sample topography.

2.2.1 Nature of contributing forces in AFMs

Unlike the tunneling current, which has very strong distance dependence, F_{ts} has long and short range contributions. We can classify the contributions by their range and strength. In vacuum, there are van der Waals, electrostatic and magnetic forces with a long range (up to 100 nm) and chemical forces with a short range (fractions of nm). In ambient conditions, meniscus forces formed by adhesion layers on tip and sample (water and hydrocarbons)may also be present.

The van der Waals interaction is caused by fluctuations in the electric dipole moment of atoms and their mutual polarization. For a spherical tip with radius R next to a flat surface (z is the distance between the plane connecting the centers of the surface atoms and the center of the closest tip atom), the van der Waals potential is given by [59]:

$$U_{vdW} = -\frac{A_H R}{6z}. \tag{2.17}$$

The Hamaker constant A_H depends on the tip and the sample material, (atomic polarizibility and density). For most solids and interactions across vacuum, A_H is of the order of 1 eV. The van der Waals interaction can be quite large, the typical radius of an etched metal tip is 100 nm and with z=0.5 nm, the van der Waals energy is about 30 eV, and the corresponding force is about 10 nN.

When the tip and sample are both conductive and have an electrostatic potential difference, electrostatic forces are important. For a spherical tip with radius R, the electrostatic force is given by [60]:

$$F_{electrostatic}(z) = -\frac{\pi\epsilon_0 RUV^2}{z}. \tag{2.18}$$

Like the van der Waals interaction, the electrostatic interaction can also cause large forces- for a tip radius of 100 nm, U= 1 V and z=0.5 nm, the electrostatic force is about 5.5 nN. Electrostatic forces can also arise in the imaging of ionic crystals, where the envelope of the electrostatic field has an exponential distance dependence.

Chemical forces are more complicated. Reasonable empirical model potentials for chemical bonds are Morse potential [59],

$$V_{Morse} = -E_{bond}[2e^{-\kappa(\kappa-\sigma)} - e^{-2\kappa(z-\sigma)}] \tag{2.19}$$

and the Lennard-Jones potential:

$$V_{Lennard-Jones} = -E_{bond}(2\frac{z^6}{\sigma^6} - \frac{z^{12}}{\sigma^{12}}) \tag{2.20}$$

The potential describe a chemical bond with bonding energy E_{bond} and equilibrium distance σ . The Morse potential has an additional parameter, namely, a decay length κ. While the Morse potential can be used for a qualitative description of chemical forces, it lacks an important property of chemical bonds. The bonding strength of chemical bond, especially covalent bonds, shows an inherent angular dependent .

2.2.2 Sensitivity of AFMs

From Hooke's Law (F=-k.x) we can see that the smallest force that can be measured depends on the spring constant of the lever, k, and the sensitivity of the displacement detection system to lever motion. The better the sensitivity of the deflection detection system, the smaller the displacement that can be measured, and hence the smaller the force that can be measured for a given lever spring constant. Therefore the lever and the displacement detection system are the most crucial factors for the sensitivity of an AFM. Initially cantilevers were home made, with the first one being a piece of gold foil with a diamond fragment glued on it, to act as a tip. However, as Binnig*et al.* [3] suggested, microfabrication became a simple and convenient way to mass produce levers with built in tips. Cantilever beam and V- shaped cantilevers can be microfabricated from silicon, silicon oxide, or silicon nitride with integral tips, and the force constant and resonant frequency can be reproducibly microfabricated. For contact force microscopy, levers with low force constants ($< 1N/m$) are used to prevent sample damage and to give good sensitivity for the force measurement. Whereas, levers with force constants of a few tens of N/m are needed for noncontact force microscopy. This is to

prevent 'snap in', and to increase the resonance frequency of the levers used in FM-AFM work, which improves the system's displacement sensitivity. For any deflection detection system, the noise in the system limits its force sensitivity. The noise can come from several parts of the deflection detection system. For an STM based system the noise is predominantly $1/f$ noise. For an interferometer based system, the main sources of noise are the shot noise in the photodetectors and laser noise due to variations in the power and the phase of the laser. The noise due to thermal oscillations of the lever may also be significant for levers with low spring constants. In Chapter 3, the sources of noise and attempts towards reducing the noise to achieve the best force gradient sensitivity will be explained. Several different methods of measuring lever displacement measurements have been employed in AFMs. In the first AFM built by Binnig *et al.* [3], an STM was used to measure lever displacement. The STM tip was situated just above the cantilever, directly behind the tip. Since the tunnelling current varies exponentially with distance, the STM is a very sensitive method to measure deflections of the lever. Deflections of less than 10^{-2} Å can be measured. However, problems associated with keeping the cantilever and tip clean reduced the reliability of this method in air. There are strong interactions between the lever and the STM tip during tunnelling, which reduce the lever's resonant frequency, and may alter its deflection. Since the STM tip must remain in close proximity to the cantilever this method is not well suited to use in nc-AFM where large vibration amplitudes are often used. Neubauer *et al.* [44] used the back of a cantilever as one plate in a capacitor. As the lever bends the change in its position results in a change in the capacitance. The variation of the capacitance is measured and used to calculate the deflection of the lever. This technique relies on a uniform smoothness and distance between the plates. The sensitivity of this technique is around $10^{-2}\frac{\mathring{A}}{\sqrt{Hz}}$. Optical techniques are generally more reliable and easier to implement than STM, and they are also less sensitive to the roughness of the lever. There are several different optical methods that have been used to measure cantilever displacement. In the beam deflection method introduced by Meyer and Amer [42], a focused laser beam is reflected off the back of the cantilever, and the position of the beam is monitored using a position sensitive photodiode. As the lever bends, the reflected beam moves across the photodiode, one segment

collects more light than the other, and a differential amplifier produces an output current proportional to the lever displacement. If a quadrant photodiode [47] is used, then information about movement of the lever parallel to the surface can be obtained along with topographic information. The torsion of the lever can be related to the friction forces on the tip. This detection method is independent of optical path length changes, but not to the thermal or mechanical drift in the direction perpendicular to the optical beam. The minimum detectable signal using beam deflection is about $4 \times 10^{-3} \frac{\mathring{A}}{\sqrt{Hz}}$.

Sarid *et al.* [61] used the sensitivity of a laser diode to optical feedback to measure cantilever displacement. The laser diode is placed close to the back of the lever, and, as the lever moves, the combined reflectivity of the front face of the laser cavity and the lever changes. The light reflected back into the laser diode changes the output power of the laser. This is measured by a photodetector which is integrated into the laser diode. This technique removes the need for extra optical components and alignment of the laser diode with the lever is straight forward. However, the non linear nature of the laser optics means that this method is only suitable for measuring small lever displacements accurately. The minimum detectable signal using this system is about $3 \times 10^{-3} \frac{\mathring{A}}{\sqrt{Hz}}$.

In a heterodyne interferometer, as used by Martin *et al.* [43], the laser beam is split into two components by a beam splitter. One of the beams which acts as, the reference beam, follows a fixed path to the photodetector. The other beam passes through an acousto-optic modulator and has its frequency shifted. This signal beam is reflected from the back of the lever and into the photodetector, where it interferes with the reference beam. As the lever bends, the path of the signal beam changes, so its phase relative to the reference beam changes. This is detected and used to calculate the displacement of the lever. Heterodyne interferometers have a sensitivity of about of $5 \times 10^{-5} \frac{\mathring{A}}{\sqrt{Hz}}$, and are insensitive to changes in the optical path length.

A typical homodyne interferometer used as a displacement sensor in an AFM consists of a laser diode coupled to a single mode fiber optics cable [48]. The end of the fibre is positioned a few microns from the back of the cantilever. The

laser beam is split into two equal parts by a 2×2 directional fiber coupler. One half of the light goes to a reference photodiode and the other half goes down the fiber to the lever. About 4%. of the light is internally reflected from the fiber-air interface, and the rest is directed at the back of the lever. Some of the light reflected from the back of the lever re-enters the fiber. This signal passes back through the directional coupler, and the interference signal of the two beams is detected at the signal photodiode. The output of the signal photodiode can be used directly as the force signal, but better sensitivity is achieved by dividing or subtracting the output of the signal photodiode by the output of the reference photodiode. This cancels out laser noise from the signal. The small cavity improves the D.C. stability of the interferometer. This type of interferometer has a sensitivity of $1 \times 10^{-4} \frac{\mathring{A}}{\sqrt{Hz}}$. Schönenberger and Alvarado [62] used a differential interferometer, which makes use of beam polarization. A laser beam consisting of two mutually orthogonal polarization states is split into two spatially separate beams, the reference and sensor beams, by passing it through a calcite crystal. Both beams are reflected from the back of the cantilever. The reference beam is reflected from the fixed base of the cantilever, while the sensor beam is reflected from the lever just behind the tip. The two reflected beams are detected by photodiodes, and the displacement of the lever is calculated from their phase difference. The output from the differential system has a large common mode rejection that cancels out most of the laser noise. The sensitivity of this interferometer is about $6 \times 10^{-4} \frac{\mathring{A}}{\sqrt{Hz}}$. Jarvis *et al.* [49] used a combination of heterodyne and differential interferometers, which used two orthogonally polarized beams, one frequency shifted with respect to the other. This give the system the benefits of both types of interferometer, and a sensitivity of $1 \times 10^{-4} \frac{\mathring{A}}{\sqrt{Hz}}$.

Silicon exhibits a strong piezoresistive effect, and this has been used to make cantilevers with a built in displacement sensors [95]. A U-shaped lever with a piezoresistor built into both legs can be easily microfabricated. The lever is used as part of a Wheatstone bridge, and the change in resistance of the cantilever as it bends, is used to measure its deflection. This type of deflection detection removes the need for a laser or any optics, and is simple to implement since it requires no alignment. The sensitivity of piezoresistive levers is of the order of

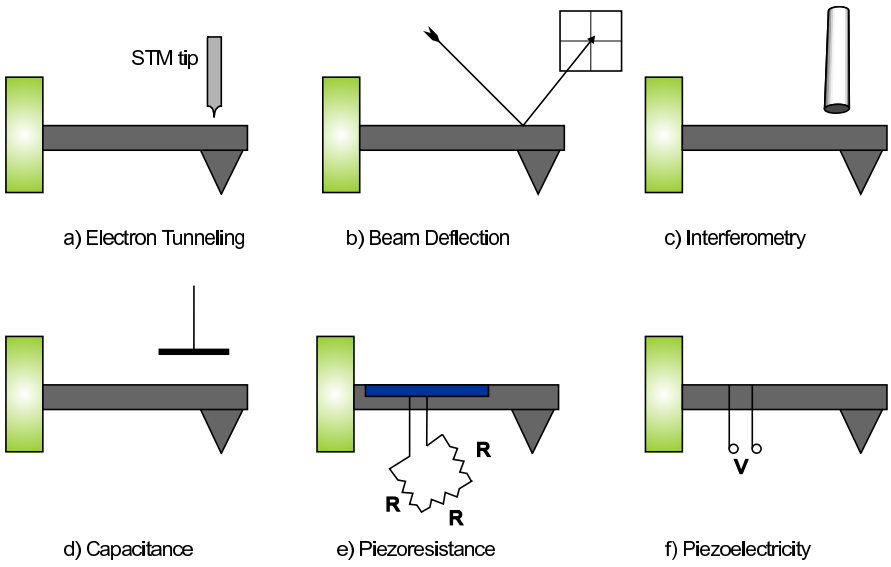

Figure 2.7: The methods of cantilever deflection measurement

$1 \times 10^{-3} \frac{\mathring{A}}{\sqrt{Hz}}$. Giessibl and coworkers [13] use qPlus sensor made from a quartz tuning fork. The qPlus sensor has stiffness of about $1800 N/m$. One of the prongs is fixed to a large substrate and a tip is mounted to the free prong. Because the fixed prong is attached to a heavy mass, the device is mechanically equivalent to a traditional cantilever. Bending the free prong of the tuning fork create current proportional to its displacement. The sensitivity of The qPlus sensor is of the order of $3 \times 10^{-4} \frac{\mathring{A}}{\sqrt{Hz}}$ at room temperature. The Schematic view of different methods of cantilever deflection measurement is shown in Fig. 2.7.

2.3 Pathway from atomic resolution imaging to single atom manipulation

2.3.1 Atomic resolution imaging using STM

The STM allowed the first atomic resolution real space images of surfaces to be taken. Demonstrating this ability, Binnig and Rohrer [1, 2] showed an atomic

resolution image of the Si(111)-(7×7) surface reconstruction. It had not been possible to unambiguously identify the exact reconstruction until the STM was used to image the surface and show where individual adatoms were positioned. Atomic resolution images of close packed metal surfaces soon followed. Au(111) was imaged by Hallmark *et al.* [96], and Winterlin *et al.* [29] imaged Al(111). Both of these surfaces were found to have corrugation heights of 0.3 Å. For these surfaces the corrugations of the Fermi level LDOS are too small to be seen experimentally, and He scattering experiments show a corrugation height an order of magnitude smaller than that seen in the STM images. Winterlin *et al.* [29] attribute the fact that atomic resolution can be seen on close packed surfaces due to adhesive tip-surface interactions causing an elastic deformation of the end of the tip. Besides imaging metal surfaces, STMs were used to image graphite and semiconductor surfaces, such as GaAs(110), and Si(100). Graphite was one of the first substrates to be imaged using STM in air [2]. The problem with the images of graphite was that the surface corrugations seen were much larger than the 0.8 Å expected from calculations, and the tunnel barrier height was much lower than expected. Tersoff [8] attributed the huge corrugations in layered materials to an anomalous corrugation of the contours of constant LDOS at the Fermi level due to the special electronic structure of layered materials. He also showed that the contours are equally spaced and independent of distance from the surface, and concludes that the STM image is likewise independent of distance i.e. independent of current at constant voltage. However, as Soler *et al.* [58] point out, the corrugations increase with increasing tunnel current, at constant voltage. They suggested that elastic deformations of the surface, when low bias voltages and high tunnel currents are used, increase the observed corrugations. In a reply to this paper Pethica [63] pointed out that the force of the contact is large enough that a contact area much larger than a single atom must be expected, and that shearing of the graphite planes is likely to happen with the large pressure exerted on the top layers. Sliding the top graphite plane in and out of registry with the layers below it would result in an image with a periodic structure on an atomic scale, without resulting in true atomic resolution. Mamin *et al.* [77] attributed the giant corrugations to a large deformation of the graphite surface, in this case caused by the presence of a contaminant layer between the tunnelling tip and the

sample, which required the tip to be force into the sample for a tunnel current to be detected, and results in a contact area larger than atomic dimensions. This would also explain the reduced tunnel barrier heights that were often seen, since the tip has to move further than expected for a given increase in tunnel current. They also noted that in UHV the experimentally measured corrugations were 0.9 Å . This illustrates the need for the use of clean surfaces with clearly defined surface structures to make interpretation of images more straight forward. The next step on from imaging surfaces was to image adsorbates on surfaces. Eigler and Schweizer [17] spectacularly showed that at 4K they could not only image Xe atoms on Ni(110), but they could also move the atoms into the shapes of letters by lowering the tip over the atom and moving it to the desired position. Following on from this Crommie, Lutz and Eigler [19] showed that by moving Fe atoms into a circle on a Cu(111) surface the local density of states inside the circle is dominated by the eigen state density expected for an electron trapped in a circular 2D box. This means that rather than imaging the positions of the atoms in the surface inside the circle of Fe atoms, the STM image is dominated by the electronic structure. Other adsorbate systems have also been imaged at room temperature, such as oxygen on Cu(110) and Ni(110), and sulphur on Pt(111). These papers also highlight the need to know what the atom on the end of the tip is, and show how that effects the STM images taken. McIntyre *et al.* [64] imaged the $(\sqrt{3} \times \sqrt{3})$R30° sulphur structure on Pt(111), and discovered that the corrugation heights of the images they took changed after pulsing the tip at 0.7 V. Imaging the area where the tip pulse occurred showed that there were several missing Sulphur atoms. They concluded that transfer of sulphur atoms to the tip had occurred, and this resulted in the image corrugations seen increasing from 0.2 nA to 1.2 nA. Ruan *et al.* [65] imaged the oxygen induced (2×1) reconstruction on both Cu(110)and Ni(110). The (2×1) reconstruction consists of rows of alternating metal and oxygen atoms in the [001] direction, spaced at one row for every two bulk lattice rows in the $[1\bar{1}0]$ direction. The images of the rows show a periodicity compatible with imaging either the oxygen or the metal atoms. The Oxygen atom has been identified as occupying the long bridge position between the Cu atoms in the [001] direction, and so if the Oxygen atoms were imaged they would be in line with the Cu atoms in the $[1\bar{1}0]$

direction. By carefully cleaning the W tip this is what is seen in the images. After scanning for a while an uncontrolled tip change occurs, and the protrusions imaged on the surface are now out of registry with the bulk Cu atoms in the $[1\bar{1}0]$ direction. This has been interpreted as an O atom bonding to the end of the tip, which causes the metal atoms to be imaged. Molecular adsorbates have also been imaged and manipulated using STMs. Cuberes *et al.* [66] have imaged and manipulated C_{60} on Cu(111), and dimethylbianthrone on Cu(111) and Bartels *et al.* [68] have imaged and manipulated CO on Cu(111). Pushing the limits of STM imaging TiO_2(110) has been imaged by Rohrer, Heinrich and Bonnell [69] at elevated temperatures. The crystal was prepared by annealing at 900K to produce an oxygen deficient surface with sufficient conductivity for STM imaging. The contrast was assigned to the Ti atoms on the grounds that the sample was positively biased, and therefore tunnelling would occur into empty Ti states in the conduction a band. This is despite the fact that the oxygen atoms site 1 Å further out of the surface than the Ti atoms. This illustrates one of the continuing difficulties with STM. While it is possible to image surfaces at atomic resolution, it is not always clear whether the image actually represents the positions of the atoms in the surface, the electronic states near the Fermi level, or some combination of the two.

2.3.2 Atomic resolution imaging in contact mode AFM

Using soft levers with spring constants in the region of 0.02 N/m to 1 N/m many groups managed to image the atomic lattice on surfaces such as graphite, boron nitride, and molybdenum disulphide [76] and LiF in air. All the images taken had used a relatively large loading force, up to 10^{-7}N, between the tip and the sample. Since the images were taken in air there would have been a layer of water and contaminants on the surface too. It was suggested [77] that the high loading forces implied a significant contact area between the tip and the sample, and that the images did not show true atomic resolution but merely atomic periodicity. For the layered materials a mechanism involving the sliding of layers in and out of registry, suggested by Pethica [63], was used to explain the

fact that the images showed atomic periodicity with the correct lattice constant for the surface being imaged. This was confirmed by *ab initio* calculations by Abraham and Batra [71]. Some groups then used this as a way to measure the friction forces between the tip and surfaces such as graphite [14], Au(111) [44] and Cu(111) [106]. Loads up to 10^{-5}N could be supported on graphite without any apparent damage to the tip or the surface, but there was a gradual loss of atomic scale resolution as the load was increased from 10^{-7}N. To support this size of load there must be a significant contact area between the tip and the sample, which means that imaging of individual atoms should not be possible. For a Hertzian contact with a force of 1×10^{-7}N a tip radius of 100nm would give a contact area with a radius of 5nm. For imaging of LiF, a mechanism involving a coherent tip surface junction was suggested by Livshits and Shluger [74]. To remove the water and contaminants, and to achieve greater resolution, AFMs were put into UHV chambers. Giessibl and Binnig [3] showed that even in UHV at 4.2 K friction effects could be seen on contact AFM images of KBr taken with only 3nN load between the tip and the sample. Clearly the problems associated with adhesion, and the uncertainty about the size of the contact, meant that it was still not clear if the images were true atomic resolution, or merely showed atomic periodicity. Meyer and Amer imaged NaCl (100) in UHV [70]. A lever without a tip and a loading force of 10^{-8} N were used to produce images which showed atomic periodicity but no point defects. The relatively high loading force and the lack of point defects indicates that the images probably do not show true atomic resolution. In order to reduce the attractive forces between the tip and sample, Ohnesorge and Binnig [51] investigated calcite under water at room temperature. By choosing a suitable liquid the long range attractive forces can be greatly reduced. They observed that at a repulsive force loading of more than 0.1 nN the step edges were removed from the surface during scanning, and a defect free atomically resolved surface was left. Images with step edges showed that the atomic periodicity of the surface could be seen without damaging the surface. Images taken with the sample gradually approaching the lever initially show attractive forces acting on the lever at sites that match the position of the oxygen atoms in the surface. As the sample gets closer the contrast inverts and repulsive forces are seen over the atom sites. Abraham *et al.* [71] used an

empirical silicon interatomic potential to model Si(100)- (2×1). By looking at the relaxation of the surface under the influence of the tip using a many body energy minimization procedure they found that the force exerted by the tip must be less than 1nN to avoid sample damage. The tip is subject to attractive forces 2 Å or more above surface, if relaxation is included in calculations, and repulsive forces closer to the surface.

2.3.3 Atomic resolution imaging in non-contact mode AFM

To avoid the snap in of the cantilever to the sample in air, the use of nc-AFM was initially restricted to van der Waals, electrostatics and magnetic force measurements [43], where the tip was at least 3 nm away from the sample. However, this produces a lower resolution than in contact mode. In 1991 Albrecht *et al.* [12] introduced a new method to increase the sensitivity of the non-contact mode, called frequency modulation. It makes use of the increased sensitivity available by using levers with high quality factors Q in UHV, but unlike slope detection the measurement bandwidth is not limited by the, Q value. The first true atomic resolution nc-AFM image of Si(111)-(7×7) was recorded by Giessibl [13] in 1995 using the FM technique. Since then several other semiconductor surfaces have been imaged including, Si(100)-(2×1) by Kitamura and Iwatsuki, InP(110) and GaAs(110) by Sugawara *et al.* [78], and InAs(110) by Schwarz et al. [79] showing the true ability of AFM, some insulator surfaces have also been imaged at atomic resolution, such as: NaCl(100), NaF(100), LiF(100), and RbBr(100) by Bammerlin *et al.* [80], TiO_2(110)-(1×1) by Fukui *et al.* [81] and TiO_2(100) by Raza *et al.*, two metal surfaces have been imaged at atomic resolution: Ag(111) islands on Si(111)-(7×7) by Orisaka *et al.* [82] , and Cu(111) by Loppacher *et al.* [83]. Nowadays imaging surfaces with atomic resolution has become more routine, there has been a move to study adsorbates on atomically resolved surfaces. For example, the following have been imaged at molecular resolution: formate and acetate ions adsorbed on TiO_2(110)-(1×1) by Fukui *et al.* [81], C_{60} on Si(111)-7×7 by Kobayashi *et al.* [84] and the Au structure on Si(111)-(7×7) by Minobe *et al.* [85]

Interestingly, atomic resolution images of the graphite (0001) surface taken by Allers *et al.* [86] using FM nc-AFM at 22K look the same as those taken by STM or contact AFM, even though the large oscillation amplitudes used implies that a different imaging mechanism is in operation. Erlandsson *et al.* [46] have used a different method to achieve atomic resolution on Si(111)-(7×7). A lever with a force constant of 60 N/m is vibrated at 16 Å free oscillation amplitude, and the tip sample distance is regulated to give a constant reduced oscillation amplitude of 5 Å. This implies that the end of the tip is in repulsive contact with the sample at the turning point of each oscillation, and that there are significant tip sample interactions. From the numbers given above a repulsive force of 60nN must be acting on the lever. The change in amplitude of the lever was measured during approach of the sample to the tip and, while no change in deflection of the lever was seen until a jump to contact occurred, the oscillation amplitude gradually decreased from 16 Å to 1 Å at the point jump to contact occurred. This indicates that some long range repulsive force was acting on the lever. If van der Waals forces were involved in the interaction a long range attractive force would be seen, which would result in an increase in oscillation amplitude. Güethnier [87] has performed a series of experiments combining STM with FM nc-AFM imaging of Si(111)-(7×7). In the first experiment the deflection of a lever, with a force constant of 10 N/m, was measured during STM operation. The lever was bent towards the sample indicating that the interaction force was attractive, and the measured force was 0.8 nN larger over the corner holes than over the adatoms. However, unusually large corrugations of 5Å were seen in the STM data. A second experiment measured the frequency shift of the lever's thermal oscillations simultaneously with tunnelling. It shows a larger reduction in frequency over the adatoms (f= -145Hz) than over the corner holes (f= -12Hz), implying that the attractive interaction is larger over the adatoms. However, performing nc-AFM using the frequency shift as the feedback signal gives a smaller frequency shift (f=-862Hz) over the adatoms than over the corner holes (f= -872Hz). This implies that the interaction force is less attractive over the adatoms, which is consistent with the tip coming into repulsive contact with the sample at the point of its closest approach. This has been confirmed by numerical simulations performed by Sokolov *et al.* [88] STM images of the Si(111)-(7×7) surface show different

contrast over different adatoms in the unit cell at positive tip bias voltages, because it is imaging the filled states near the fermi level, and the different adatoms have different amounts of electron density associated with their dangling bonds. Different contrast has also been seen in FM nc-AFM images of the surface. Erlandsson *et al.* [46] saw increased contrast for the center adatoms. However, the pattern of contrast did not match the STM filled states contrast, or the relative heights of the adatoms. It was suggested that under the repulsive contact at closest approach of the tip there was a difference in the relaxation of the adatoms that caused the contrast. The amount of contrast the adatoms have follows the expected order of reactivity for the adatoms. Nakagiri *et al.* [89] have seen contrast in FM nc-AFM that matches the expected contrast for a filled states STM image. Varying the amplitude of the oscillations, while keeping the frequency shift constant, shows that this contrast is seen over a small range of vibration amplitudes. For larger oscillation amplitudes the contrast difference is lost and all the adatoms appear the same. Since the tip-sample distance is changed to maintain the fixed frequency shift, it is not clear for which oscillation amplitudes the tip approaches closest to the sample, or whether the tip is experiencing an attractive or repulsive force gradient. It is not possible to identify the faulted and unfaulted halves of the unit cell from this data. Sugawara *et al.* [90] also observed a similar contrast in the FM nc-AFM images to that expected for a filled states STM image. Again the contrast depended on the imaging parameters, the amplitude and frequency shift, which appear to be different for different apparatus, since the values used here were not at all close to the values used by Nakagiri *et al.* [89]. Sugawara *et al.* [90] have also reported a difference in the quality of the FM nc-AFM images depending on whether there is a discontinuity in the force-distance curves or not. This is explained as a shift from a physical bonding interaction to a chemical bonding interaction caused by a change in position of the tip apex atom. The use of the FM technique has raised the questions of how the measured frequency shifts relate to the force, or force gradient, acting on the lever and how close to the sample the tip is approaching. In order to clarify the situation force, or force versus distance curves have been measured. Oral *et al.* [41] showed the direct observation of short-range bonds, and the measured short-range force interaction agrees well in magnitude and length scale

with theoretical predictions for single bonds. Atomic resolution is shown to be associated with the presence of a prominent short-range contribution to the total force interaction. It is presented that the background longer-range interaction, whose relative magnitude depends on the tip structure, has a significant effect on the contrast observed at the atomic scale. The quantitative force gradient images are obtained using a sub-Ångstrom oscillation amplitude, off-resonance lever oscillation method during scanning tunneling microscopy imaging. Özer *et al.* [91] recently reported simultaneous scanning tunneling and atomic force imaging of Si(111)-(7×7) with atomic resolution using sub-angstrom oscillation amplitudes. They showed both constant height and constant current scans with tungsten tips/levers always exhibit larger attractive stiffness over corner holes than over the adatoms, in contrast to the theoretical expectations. They have also presented constant height scans which cannot be explained by interaction of tip motion with long range forces. Silicon levers, however, sometimes exhibited inversions of force contrast following local tip changes. They suggest that there may be charge variations between atomic sites on the surface, which produce electrostatic tip forces in addition to the covalent forces,which is usually regarded as dominant factor.

2.3.4 Force Measurement by STM

Tunnelling experiments between two gold electrodes by Teague [25] had shown that attractive forces needed to be taken into account to explain his experimental results. After the invention of the STM, importance of the forces during STM operation came from the observation of anomalous tunnel barrier heights by Chen and Hamers [92]. As the clean tungsten tip approaching a clean Si sample in UHV, they saw an increase in the tunnel barrier height from 3.5 eV, 4 Å from the surface to 4.8 eV, 1.5 Å from the surface. The barrier height then collapsed to close to zero when the tip was within 1Å of the surface. They concluded that the force between the tip and the sample induced deformation in the tip and sample in the vicinity of the tunnelling gap. This resulted in the actual z displacement being more than the measured tip movement. Several STM experiments were performed in UHV

to see the effect of forces on the topographic sample images. Dürig *et al.* [52] used thin metal cantilever beams, made from steel, copper, or tantalum, as the sample substrate, and measured the frequency spectrum of the tunnel current during tunnelling at different currents for a set voltage. There was a positive frequency shift, which increased with increasing current or decreasing voltage. This implies a positive force gradient over the whole tunnelling range, which, in turn, implies that a repulsive force was acting. As the authors point out this is rather strange because an attractive force gradient is expected to act starting 1.5Å away from the surface, and a repulsive force gradient is expected at closer distances. If the tip were really that close to the surface,the tunnel barrier should have collapsed, and a metallic contact would have formed. The most likely reason for seeing a repulsive force is that the tip had an oxide layer on it and was in contact with the sample. Moreover, when the end of the beam was imaged at successively smaller voltages, while the current is kept constant, finer details appeared at the grain boundaries observed in the images. This did not happen for images taken at the fixed end of the beam. The forces between the tip and the sample had affected the images. Further experiments by Dürig *et al.* [53], using a metal beam as the sample again, measured the interaction force gradient between an Ir tip and the Ir sample beam, while performing STM imaging. The maximum attractive force gradient measured was -8 N/m. This implies that an attractive force was acting between the tip and the sample. In this case the attractive forces were interpreted as metallic adhesion forces between the tip and the sample. The STM images showed a lateral resolution of a few angstroms, but atomic resolution was not achieved. Performing a similar experiment on an Al film, which had been exposed to 1L of oxygen, regions with attractive and repulsive interaction force gradients were found. The regions with repulsive interaction force gradients were identified as oxidized Al. Using self consistent calculations on Al(100), Ciraci [93] showed that the perpendicular force and barrier height are site dependent, and that the corrugation of the surface potential is enhanced by the tip-induced modifications of electronic structure. This may be the reason STM images of close packed metal surfaces show atomic resolution, even though the density of states at the fermi level is essentially flat. Clarke *et al.* [94] investigated the effect of tip-surface forces on tunnel barrier heights on Cu(100). By measuring the change

in corrugation height of images taken at different tunnel currents, but with the same bias voltage, the tunnel barrier height could be calculated. At low tunnel currents the barrier height was found to be constant, while at higher currents, from about 3nA, there was a roll off in the barrier height caused by the tip-sample interactions. Attractive tip-sample interactions cause the corrugation heights measured from the movement of the z-piezo to be less than the real corrugation. Molecular dynamic simulations showed that the force between the tip and the sample is about 1 nN at a separation of 3.5 Å.

2.3.5 Force Measurement by AFM

All attempts to measure the force interaction between a tip and a sample in air were subject to the same problem. A layer of adsorbed water and contaminants were present on the surface of the sample. This caused the lever to 'snap in' to contact with the sample's surface when the attractive force gradient became larger than the lever's force constant. The force-distance curves recorded in air also showed significant hysteresis between the approach and retraction curves caused by the strong adhesive forces on the tip. The large adhesive force also resulted in a significant contact area between the tip and the sample, and may cause deformation of the tip or sample as well. For example, Burnham and Colton [95] have measured $F - d$ curves on graphite and gold surfaces which show forces as large as 150 nN between the tip and the sample after 'snap in' has occurred. One way of reducing the long range van der Waals interactions is to immerse the lever in a liquid, as was done by Ohnesorge and Binnig [51]. The lever was submerged in water and force-distance curves were measured between the silicon tip and the calcite sample. The attractive force had a maximum value of -0.2 pN approximately 4 Å from the sample. The interaction range of 7 Å is the shortest that had been measured. Moving AFMs into UHV removed the contaminants from the sample's surface, but the problem of the lever snapping in to the sample's surface was still present, because soft levers were still being used. The frequency modulation technique developed Albrecht *et al.* [12] allowed much greater sensitivity in the noncontact mode. However, large vibration amplitudes,

of the order of 10nm, are used, and the measured quantity is the shift in frequency of the lever as the lever is brought closer to the surface. This makes it very difficult to deconvolve the different forces acting on the lever over the course of its motion. An alternative approach was taken by Jarvis *et al.* [96]. A magnetic force feedback technique was used to increase the stiffness of a lever as it approached the surface of a sample and prevent 'snap in'. A small piece of a Sm-Co magnet was mounted on the back of the lever, and a current carrying coil was used to apply a magnetic force on the lever directed away from the sample, which increased the lever's effective stiffness. Using this technique it was possible to map out the stiffness of the interaction during approach and retraction of the Si(111) sample from the silicon tip. The interaction range was about 3nm, and the maximum interaction stiffness was found to be -0.13 N/m. This is clearly too long a range to be due solely to covalent bonding interactions. A long range van der Waals background force was also observed in the force measurement. The maximum force on the lever, as calculated by integration of the interaction stiffness, was 0.3nN. Cross *et al.* [97] measured force-distance curves between a W(111) trimer tip and a Au(111) sample mounted on a lever with a spring constant of 120 N/m. The tip was imaged at atomic resolution, using Field Ion Microscope (FIM) before and after the experiments, apart from picking up a couple of adsorbed atoms, the tip was unchanged. This is despite the fact that it was pushed into the sample, as was indicated by the repulsive part of the force distance curve. The measured force distance curves were reproducible, and show an attractive interaction range of about 1 nm, with a maximum attractive force of 3nN on approach and 5nN on retraction and no sign of a jump to the contact. This interaction is too long range for the metallic adhesion forces which were being investigated. Jarvis *et al.* [96] have used an off-resonance ac mode for force spectroscopy. Using a stiff Pt/Ir coated Si lever (k=37 N/m) oscillated at 2.6 Å amplitude off resonance, the Au on mica sample was moved towards the lever, and the resulting change in amplitude was measured. This allows calculation of the force gradient acting on the lever. A maximum attractive force gradient of 9 N/m was measured on approach and retraction of the sample. Integrating this gives a maximum attractive force of 5 nN. The interaction range was 1nm, which is still too long range for the expected range for adhesion forces. Gotsmann *et al.* [98] have used a numerical algorithm

to calculate a force-distance curve from a series of Δf-distance curves. Using the FM technique, and starting with the lever out of the strong interaction range, the lever is incrementally moved towards the sample. The difference between the interaction at each position is calculated and used to build up a force-distance curve. The curve calculated in this way gives an interaction range of about 2.5 nm and a maximum attractive force of 5 nN. This value similar to that measured value by other groups, but it is still too long range to be a covalent bonding type interaction. Since the FM technique averages the interaction over the whole oscillation cycle, the force-distance curve only represents the change in the average interaction on the lever. Erlandsson *et al.* [40] recorded f-d curves which shows that, 'snap in' can still take place even for a lever with a spring constant of 60 N/m in UHV. The lever was oscillated with a free amplitude of 16 Å, which was seen to decrease as the lever approached the sample. When the lever's oscillation amplitude had dropped to 2 Å there was a sudden jump in the lever deflection of about 6 Å towards the sample. No lever deflection had been detected before this occurred. This was accompanied with a complete damping of the oscillations. Dürig [54] has recently shown that it is possible to calculate the interaction force from the frequency shift data. However, the frequency shift curve is proportional to a quantity that is intermediate between the force interaction and the interaction potential. Also, the region of the frequency shift curve where atomic resolution imaging can be achieved is the region of maximum adhesion and the onset of repulsive interactions. This implies that repulsive interactions are important for atomic resolution imaging using the FM technique.

2.3.6 Molecule and atom manipulation

STM and AFM are versatile and powerful methods not only for imaging but also for manipulate of atoms and molecules with atomic scale precision. In 1990, D.Eigler and E.Schweizer [17] achieved an impressive demonstration of atomic scale manipulation,they used an STM held at 4 K to write out "IBM" by arranging xenon atoms one at a time on a nickel surface, Fig. 2.8. Indeed, forces that acts between the STM tip and the sample can drag individual adatoms along the

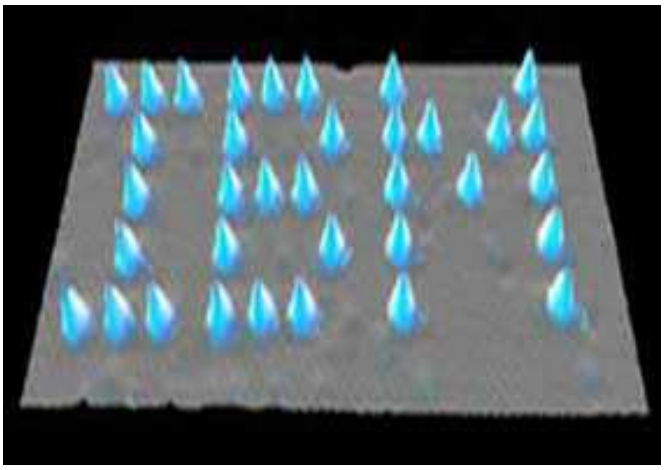

Figure 2.8: Manipulation of the Xe atoms on Ni(111) surface using LT-STM. (Adapted from [17]).

surface at small tip-surface distances, provided the adatoms are weakly bound. Once moved, the atoms can then be imaged by increasing the tip-sample distance. Moreover Dunn *et al.* [99] has realized manipulation of C_{60} molecules and cluster formation on Si(111)using STM at room temperature. The manipulation has achieved by using a sweeping procedure, which moves the tip closer to the surface and sweeps it across in a predetermined direction, while feedback control of tunnel current is maintained throughout and the tip-surface septation is adjusted by changing the sample bias and tunnel current. Sugimoto *et al.* [100] used nc-AFM technique to create an artificial pattern akin to Eigler's one, but at room temperature. They showed that Sn atoms deposited on Ge(111)-(2×8) reconstructed surface could be forced to switch positions with Ge atoms,Fig. 2.9. In atom manipulation using dynamic AFM each tip oscillation can extract enough repulsive force to break an atomic bond, for instance, or enough attraction force to influence surface effects, depending on how signal feedback levels are configured. In spite of all the attempts, a fundamental question left open, how much force and how much energy is required to initiate an atom or molecule to move from one atomic site to the next?

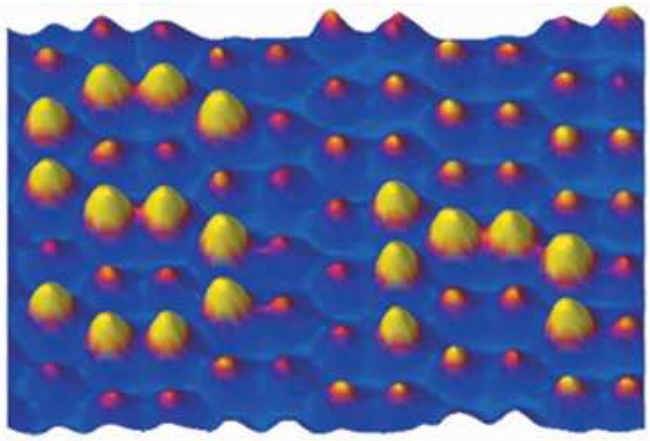

Figure 2.9: Atom interchanging using room temperature FM-AFM. (Adapted from [100]).

2.4 Lateral force microscopy at the atomic scale

Friction plays a central role in diverse systems and phenomena. The development of durable and/or low-friction surfaces and thin lubricating films has become an important factor in the miniaturization of moving components in many technological devices. These include micro-electro-mechanical systems (MEMS), computer hard disks systems and miniature motors with small loads. The old, simple empirical laws of friction do not always hold in such systems; this is due to their high surface-to volume ratio and the greater importance of surface chemistry, adhesion and surface structure or roughness. Conventional tribological and lubrication techniques used for large objects can be ineffective at the nanometre scale, which requires new methods for control. Another rapidly growing area of tribology is in bio systems, and particularly the lubrication mechanisms in joints. Through the process of natural selection, nature has produced water-based lubricant systems, which far by out perform the best oil-based lubricants developed by the human kind. These systems are one of todays great challenges. At the conceptual and theoretical levels, however, recent advances have revealed enormous complexity for the simplest tribological processes. Friction is intimately related

to both adhesion and wear, and all three require an understanding of highly non-equilibrium processes occurring at the molecular level to determine what happens at the macroscopic level. Surfaces can be smooth or rough, hard or soft, elastic, viscoelastic or plastic, brittle or ductile, dry (unlubricated) or lubricated, and of very different chemistries. The multitude of asperities on two shearing surfaces are constantly coming into and out of contact, where the local pressure between them can fluctuate between, 1 Pa and a few GPa within microseconds. These are extreme conditions that cannot always be treated by simple linear theories. To understand the behavior of two real surfaces in relative motion, while still in contact, we need to look into what is going on at the single asperity level. With the advent of the atomic force microscope (AFM) and its relative the lateral force microscopy(LFM) it became possible to study individual sliding junctions at the atomic level. In LFM, a sharp tip is brought into contact with a surface, which causes the normal bending of the cantilever supporting the tip. If the tip is then shifted with respect to the sample (or vice versa), the cantilever is also twisted. Both vertical and lateral movements are realized with piezoelectric elements below the sample. The two deformations can be detected using alternative detection methods. The normal and lateral forces acting on the cantilever can be deduced from the normal and lateral acquired signals, provided that the spring constants of the cantilever and the detection sensitivity are known. Friction on the atomic scale was measured for the first time in 1987 by Mate *et al.* [14] using a tungsten tip on graphite. They reported two important effects, first a saw-tooth pattern of lateral forces (stick-slip) and second, hysteresis between forward and backward scans (friction loop). A rather linear dependence of friction on normal force with friction coefficient $\mu = 0.01$ was also found. Later on, friction on ionic crystals was studied by E.Meyer and coworkers with an UHV FFM apparatus [101–105], which made possible the detection of atomic stick slip on NaF, NaCl, AgBr and KBr with standard silicon tips and the obtained friction map on KBr(100) is compared with a theoretical map, determined with the 2D Tomlinson model. With the same UHV-FFM Bennewitz *et al.* [106] measured atomic stick slip on copper. A reproducible stickslip behavior was detected on the Cu(111) surface, whereas irregularity and producibility of results were found on the Cu(100) surface. Molecular Dynamics simulations by Sorensen *et al.* [107]

proved that sliding without wear occurs preferably on the close packed Cu(111) surface rather than on Cu(100). In their simulations, Cu tips were used. Thus, in the experiments of Bennewitz *et al.* [73] the FFM tip was most probably covered by copper. This hypothesis is supported by the weak load dependence of friction and by current measurements Atomic stick.slip on the hard diamond (100) and (111) surfaces was first observed by Germann *et al.* [108] with an diamond tip in UHV. Subsequently, van der Oetelaar and Flipse measured friction on hydrogen-terminated diamond (111) with silicon tips [109]. The removal of hydrogen from the surface gave rise to an enormous increase of friction. Fujisawa *et al.* [110] measured friction on mica, MoS_2 and NaF with a 2D FFM apparatus, which revealed friction forces also perpendicularly to the scan direction [110, 111]. This effect is a consequence of the zig-zag walk of the tip, which can be predicted within the 2D Tomlinson model [112]. It is remarkable that the 2D stick-slip on NaF was limited to loads below 14 nN, whereas loads up to 10 μN could be applied on layered materials. Thus, the 2D stick-slip on NaF is related to a few-atom contact. The zig-zag walk on mica was confirmed by Kawakatsu and Saito [113] using an original 2D FFM with two laser beams and two quadrant photodetectors. The velocity dependence of friction on the atomic scale was recently studied by Gnecco *et al.* on NaCl [101]. It was proven that the atomic scale stickslip varies according to a logarithmic law at low velocities (v <1 μm/s), as predicted by the thermally activated Tomlison model [112]. A logarithmic dependence on velocity was also reported by Bennewitz *et al.* [73] on Cu(111). The velocity dependence of friction on the micrometre scale was studied by Bouhacina *et al.* [114] and by Zwörner *et al.* [115]. In the first experiment both triethoxysilane molecules and polymers grafted on silica showed a linear increase of the friction force with the logarithm of the sliding velocity up to $v = 300\mu$m/s [116]. They have proven that the mechanism of thermal activation is not relevant when the sliding velocity exceeds a critical value v_c, so that friction becomes independent of velocity. The critical velocity depends on several parameters, i.e. the tip-sample potential, applied load, temperature and a characteristic frequency f_0 . Thus, it cannot be excluded that v_c lay in the velocity range explored by Zwörner *et al.* The role of the sliding direction in friction processes was also clearly observed by Hirano *et al.* [116] in the contact of two mica sheets with different orientations. Overney

et al. [117] realized the first measurements of friction anisotropy by FFM on an organic bilayer film and proved that different molecular alignments lead to a significant change of friction. Further measurements of friction anisotropy on stearic acid single crystals have been reported by Takano and Fujihira [118]. In the context of nanosled experiments, Sheehan and Lieber observed that MoO_3 islands on MoS_2 slide only along low index MoS_2 directions [120]. In contrast, L*ü*thi *et al.* [105] found that friction is independent of direction for the case of C_{60} islands on NaCl. Such different behavior is probably due to the large lattice mismatch of C_{60} on NaCl, which should give a weak dependence of orientation. An example of friction anisotropy is related to carbon nanotubes (CNTs). Falvo *et al.* [122] manipulated CNTs on graphite using an AFM tip. A dramatic increase of lateral force was found in certain discrete directions, corresponding to transitions from incommensurate to commensurate states. At the same time the CNT motion changed from sliding/rotating to stickroll. Studies of sharp tips sliding in gentle contact over sample surfaces have already contributed to the understanding of the microscopic origins of friction forces. However, the lateral resolution of force microscopy in the contact mode is limited by a minimum contact area containing several atoms due to adhesion between tip and sample. This problem has been overcome in noncontact atomic force microscopy. Jarvis *et al.* [55]. developed a special cantilever layout for simultaneous control of tip-sample distance and lateral tip oscillations in order to sense lateral interactions between tip and sample when approaching the surface. Giessibl *et al.* [125] presented lateral force atomic resolution, used a later force sensor consisting of a tuning fork with a fixed prong and a tip attached to the free prong and intentionally tilted the tip with respect to the sample by 6°. The interaction between a single-tip atom that is oscillated parallel to an Si(111)-(7 × 7) surface is measured. A dissipation energy of up to 4 eV per oscillation cycle is found,as shown in Fig. 2.10. The dissipation is explained by a plucking action of one atom on to the other as described. Pfeiffer *et al.* [126]. reported Lateral forces between the tip of a force microscope and atomic-scale features on the surface of a sample can be accurately measured in a noncontact mode. Feedback-controlled excitation of the torsional eigenmode of a rectangular cantilever beam forces the tip to oscillate parallel to the Cu(111) surface. Forces of the order of 0.05 nN have been detected when the tip approaches

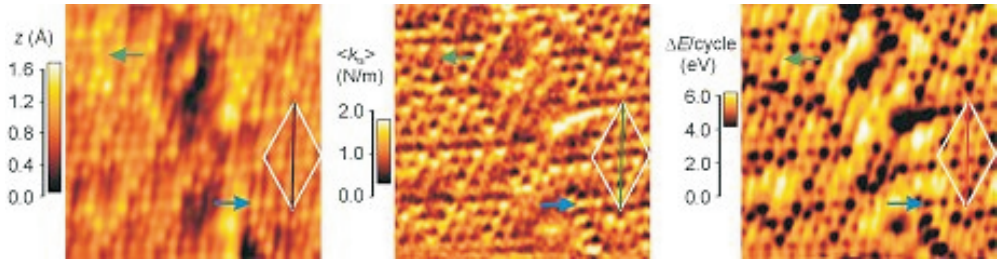

Figure 2.10: Topography, average lateral stiffness, and damping signal recorded simultaneously while imaging Si(111)-(7 × 7). (Adapted from [125]).

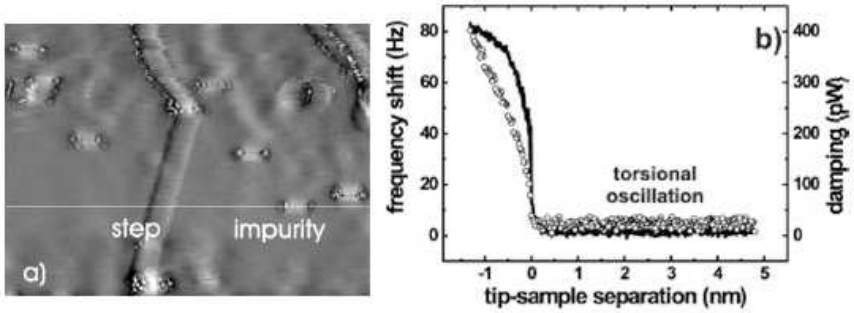

Figure 2.11: a) Frequency shift map of the lateral oscillation recorded while scanning at constant tunneling current on a Cu(100)surface. A monatomic step running from top to bottom and several sulphur impurities appear. b)Frequency of lateral oscillation parallel to the surface (solid line) and damping (open circles) vs. sample displacement curves..(Adapted from [126]).

a step or a sulphur impurity, as shown in Fig. 2.11.

Kawai *et al.* [127] reported lateral force atomic resolution using frequency modulation dynamic lateral force microscopy. Torsional resonance mode of a commercially available rectangular cantilever was used to detect interaction lateral force gradients caused between the tip and the sample surface. As shown in Figure 2.12, individual adatoms in a unit cell of the Si(111)-(7×7) reconstructed surface were imaged with the constant frequency shift mode. Two sets of the neighboring corner adatoms and one set of the center adatoms on the dithering direction of the tip were connected on the image. This method has a great

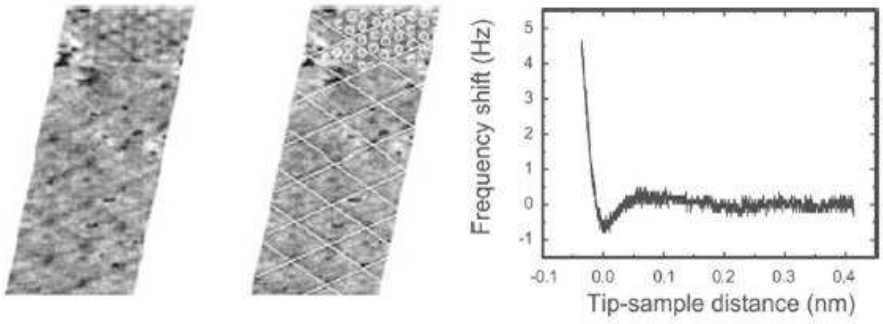

Figure 2.12: a)An atomically resolved constant torsional resonance frequency shift image of the Si(111)-(7×7) reconstructed surface. On the top quarter part, individual adatoms in a unit cell could be resolved.b) The torsinoal frequency shift vs. tip-sample distance curve.(Adapted from [127]).

potential to observe friction between single atoms. A heterodyne Doppler interferometer was used to measure the velocity of the cantilever with the resonance frequency up to around 2 MHz. In their technique a superheterodyne circuit was used to excite the cantilever in its resonance.

Chapter 3

Instrumentation and Noise Analysis

This chapter describes the experimental equipment, construction details and procedures used to do the measurements in the next chapter. In addition, noise analysis and the developments made to reduce the noise in order to achieve the highest sensitivity will be explained. All of the experimental work details in this thesis was carried out on a newly designed, combined scanning tunnelling and non contact lateral atomic force microscope(STM/Lateral nc-AFM) in ultra-high vacuum (UHV), which was built in the Department of physics at the University of Bilkent. We used two UHV systems. One home built system and the other one has been donated by University of Oxford.

The apparatus consists of two main parts, a UHV system and the STM/Lateral-nc-AFM. There are two main reasons for using UHV conditions to carry out STM or AFM experiments. First of all, an atomically clean surface is necessary for STM or AFM is imaging. Moreover, at the UHV pressures the mean free path of ions and electrons is significantly greater than the distances between the sample and the ion gun or the low energy electron diffraction (LEED) optics. Therefore collisions between electrons or ions and gas molecules in the chamber can be neglected, and the specimen is kept clean for up to a week.

3.1 The ultra-high vacuum (UHV) system

The UHV system which we mainly performed our experiments in, consists of a single chamber separated from a fast entry lock (FEL) by a gate valve. The chamber itself is mounted on a frame that has rubber pads under its feet to help reduce the vibrations transmitted from the surroundings to the chamber. The FEL can be pumped separately from the main chamber by closing the gate valve. The FEL is pumped by a 70 l/s turbo pump, which is backed by a rotary pump with a foreline trap. There is a one way valve between the turbo and rotary pumps that prevents gas diffusing back into the FEL when the pumps are turned off. The main chamber is pumped by a 300 l/s Starcell ion pump and a titanium sublimation pump. The chamber is fitted with an ion gauge, which can measure the pressure under vacuum conditions down to pressures as low as 3×10^{-11} mbar, and a LEED system. The typical operating pressure for the chamber is 8×10^{-11} mbar after the 'bake out'. Whenever the system has been open to air, it is necessary to 'bake out' the chamber to obtain UHV conditions. During a 'bake out' the whole system is enclosed in heat shields and the chamber is pumped out while it is heated up to 155 °C for around 48 hours. The 'bake out' is ended once the pressure has dropped to about 3×10^{-7} mbar. The 'bake out' causes gas molecules, especially water, that are adsorbed on the chamber's walls to be desorbed and pumped out of the system. While the chamber is still hot after the 'bake out' all the equipment in the chamber which has filaments should be degassed. This prevents the gas molecules that are desorbed from the filaments from sticking to the chamber walls, and means that the filaments do not out-gas when they are operated later. The UHV system is shown in Figure 3.1.

3.2 Cantilever/Sample Transfer and electron beam heater

Sample and cantilevers are transferred in to the main UHV chamber through the Fast Entry Lock(FEL) by using a magnetic transfer arm. After the FEL

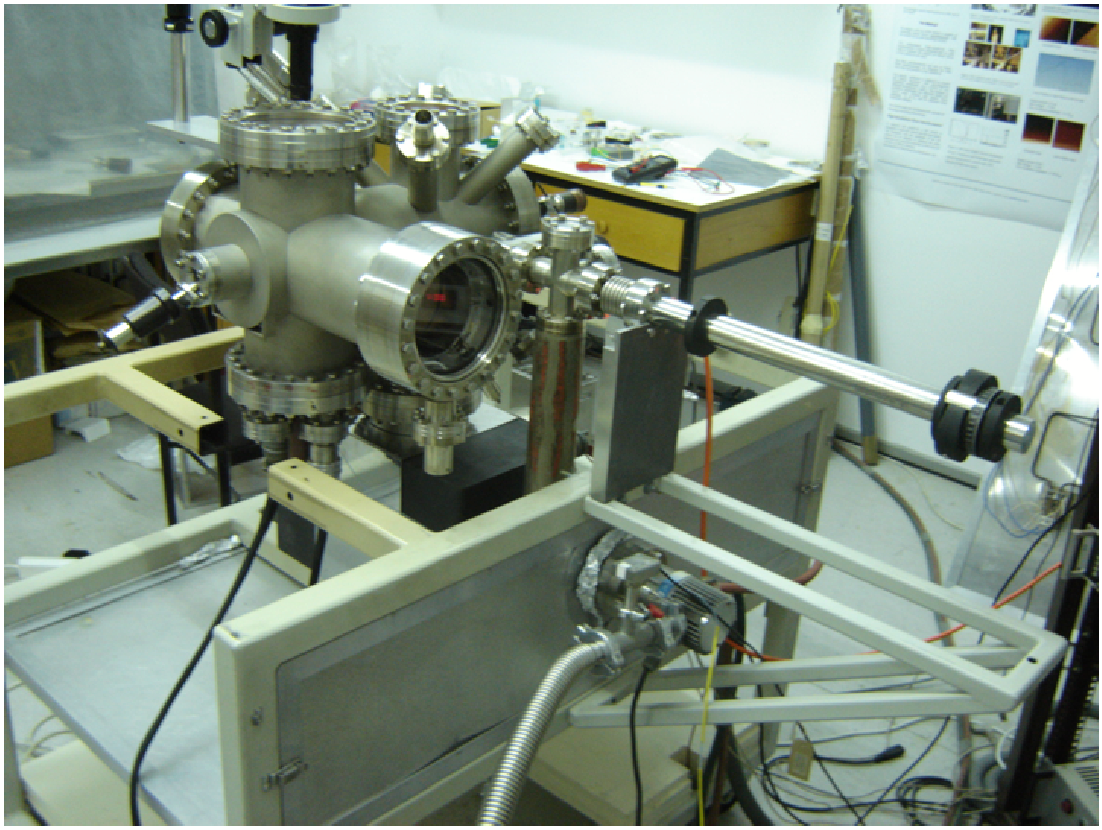

Figure 3.1: The picture of UHV chamber

port is closed, the turbomolecular pump is run for about 1 hour, then the gate valve is opened and the sample or cantilever is transferred to the UHV chamber using the sample manipulator which is mounted onto push pull rotary-motion feedthrough. Then the sample and cantilever is transferred from the manipulator to the microscope stage or carousel using a pincer-grip wobble stick. The FEL allows samples and tips to be transferred into, or out of, the chamber without breaking the vacuum. The tips and samples are mounted on holders with a common geometry that fits into the transfer system. A pin on the magnetic transfer arm fits into a hole in the sample holder, and a leaf spring holds the sample holder in place. Initially the FEL was heated, using heater tapes wrapped around the magnetic transfer arm and the entry lock, to try to reduce the amount of water that was admitted to the chamber when the gate valve was opened. To allow for the heating and cooling of the FEL the time that the FEL was pumped down was increased to three hours. However, there are a number of reasons why this procedure was abandoned. Firstly, the levers were individually tested in UHV to determine if their reflection gave sufficient sensitivity to be used in the interferometer, and often several levers were rejected before three suitable ones were found. This meant that a lot of time was spent heating and cooling the FEL. Secondly, heating the FEL also heated the gate valve and caused the seal to leak gas into the chamber, which was what we were trying to avoid in the first place. It was also very difficult to heat all of the FEL to over 100 ^{o}C, and so be sure that all the water had been pumped out of the FEL. The deciding point was the fact that it was found to be easier to obtain atomic resolution STM images if the levers had been 'baked out' in the chamber. So it was decided that the we would keep the chamber under the best vacuum possible without spending too much time pumping down the FEL, and then, when three suitable levers were found, the whole system would be 'baked out' for 12 hours. The e-beam heater is built into the sample manipulator for sample cleaning. Top view of the e-beam heater is shown in Fig. 3.2. The filament is kept at -1200V and the sample is grounded. The filament current is regulated to control the emission current I_{em} , hence the heating power. The sample can be heated up to 1400 °C with this heater. Figure 3.2.(b) shows degassing and flashing procedure of Si(111) sample. The e-beam heater was designed and built in house from

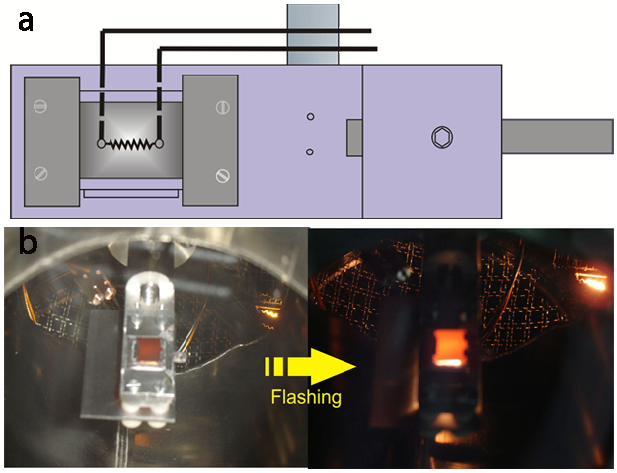

Figure 3.2: Schematic view of e-beam heater

tantalum pieces, using alumina insulating pieces to insulate the filament from the base. The current flowing through the filament is adjusted by the heater electronics to heat it so that thermionic emission of electrons occurs. The high voltage between the sample and the filament accelerates the electrons towards the sample. The sample holders are held in the manipulator arm just above the heater. There is a hole in the sample holder so that the electrons can hit the backside of the sample and heat it. A tantalum shield surrounds the filament so that stray electrons cannot escape into the chamber. The manipulator arm, which can rotate about its direction of travel, allows transfer of the sample to the far end of the chamber, where it can be removed from the manipulator with a wobble stick. This is used to either place it on a carousel, where it can be stored until it is needed, or to place it directly onto the sample slider. The carousel can store up to four sample or tip holders at one time.

3.3 Construction of combined lateral non-contact AFM and STM

The microscope is mounted on a 8" special CF flange. This has two 20 pin instrumentation feedthroughs to bring electrical connections into UHV. The fiber feedthrough is mounted on a 1.33" CF mini flange, which brings the fiber optic cable into UHV. There is a UHV linear motion feedthrough which is used to lock the base plate during sample and cantilever transfer to the microscope. In order to reduce the external vibrations, a single stage spring suspension system with eddy current damping is used. There are four springs mounted on adjustable collars to balance the microscope and four Sm-Co magnets are surrounded by copper plates attached to the microscope base for eddy-current damping. The microscope also contains two piezo coarse positioner; the sample slider , the fiber slider, and cantilever mount. The photograph of the STM/nc-AFM is shown in Fig.3.3. The sample slider which performs the coarse approach of the sample towards the cantilever. The three dimensional scanning is performed by a single tube piezo with split electrods mounted on slider and the macor sample holder gluded on the end of piezo tube. The sample slider performs the coarse approach of the sample towards the cantilever, whereas the fine approach and scanning is achieved with the tube piezo.

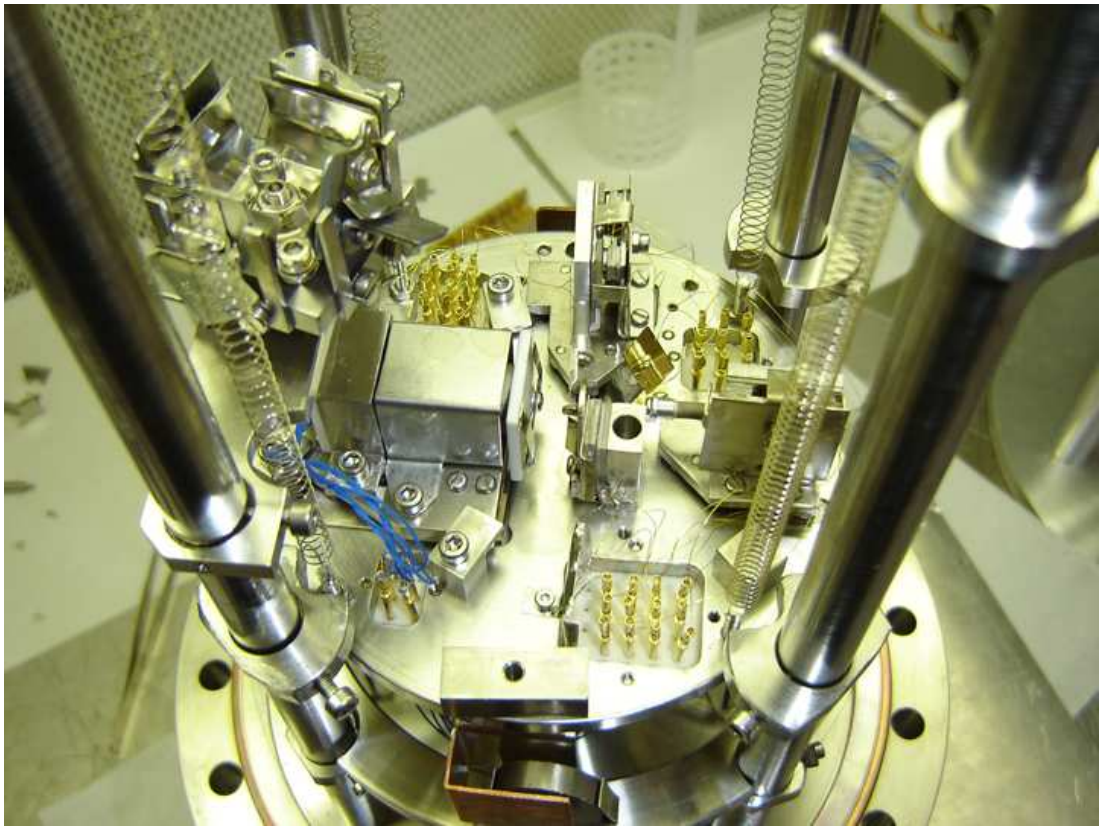

Figure 3.3: The picture of our home-made combined lateral non-contact AFM and STM.

3.3.1 The Sample Slider

The sample slider performs the coarse approach of the sample towards the cantilever. The schematic view of a sample slider is shown in Fig. 3.4, the 3 dimensional scanning is performed by a tube piezo mounted on slider and the macor sample holder glued is at the end of piezo tube. The sample slider performs the coarse approach of the sample towards the cantilever, whereas the fine approach and scanning is achieved with the tube piezo. Under the slider, there are three set of cross polarized shear piezos: two front corners and one at the back as shown in Figure 3.5.

On top of each shear piezo set, there is a small one side polished Alumina ceramic piece is glued. Sm-Co magnets mounted on the base plate under slider which pull the nickel plate at the bottom of the slider increase the stiffness of the system. To move the slider, a voltage signal of the form $V \propto t^2$ is applied across the three shear piezos. When the voltage reaches a predetermined maximum value, it is brought to zero in a few microseconds, this causes one electrode of the shear piezo to moves with respect to the other electrode laterally and the inertia of the slider keeps it in its new position, as shown in Fig. 3.6. Rapidly repeating the voltage pulses allows the slider to be moved in the desired direction at a rate of a few mm per minute. The slider is also able to move sideways by using the other set of which have polarization direction rotated by 90° with respect to other set. The slider can also be rotated clockwise and counterclockwise by applying voltage to the relevant piezos electrodes. The coarse approach-sliders motion- is controlled by setting the frequency and voltage pulse duration through the computer program and then activating the different directions using joystick which is connected to the AFM Electronics.

3.3.2 Scanning Mechanism

A single piezoelectric tube serves as a sample scanner. Piezoelectric materials change their shape in an electric field, due to their anisotropic crystal structure and permanent electric dipoles in the crystal. Using the transverse piezoelectric

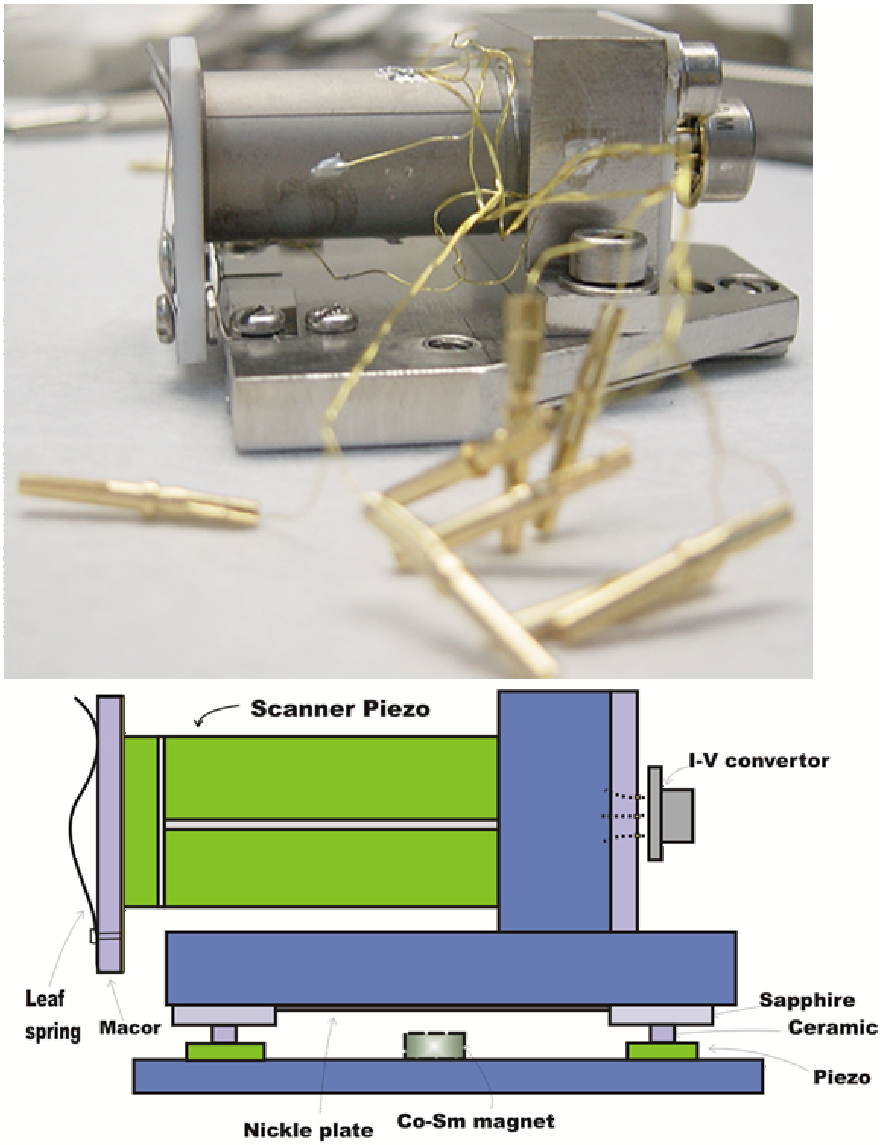

Figure 3.4: (a) The picture and (b) Schematic view of the sample slider

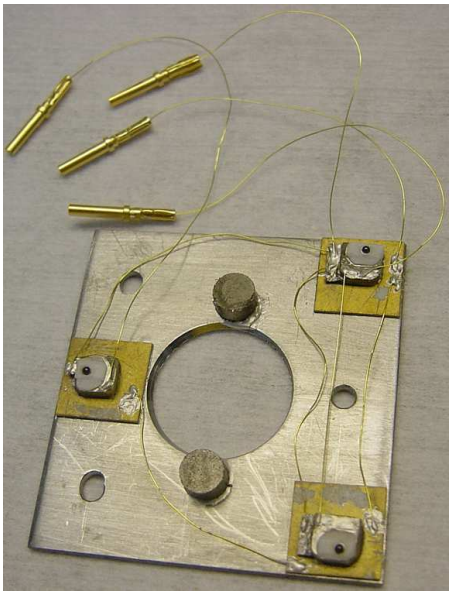

Figure 3.5: The picture of slider piezos and mounting pieces used for sample coarse approach.

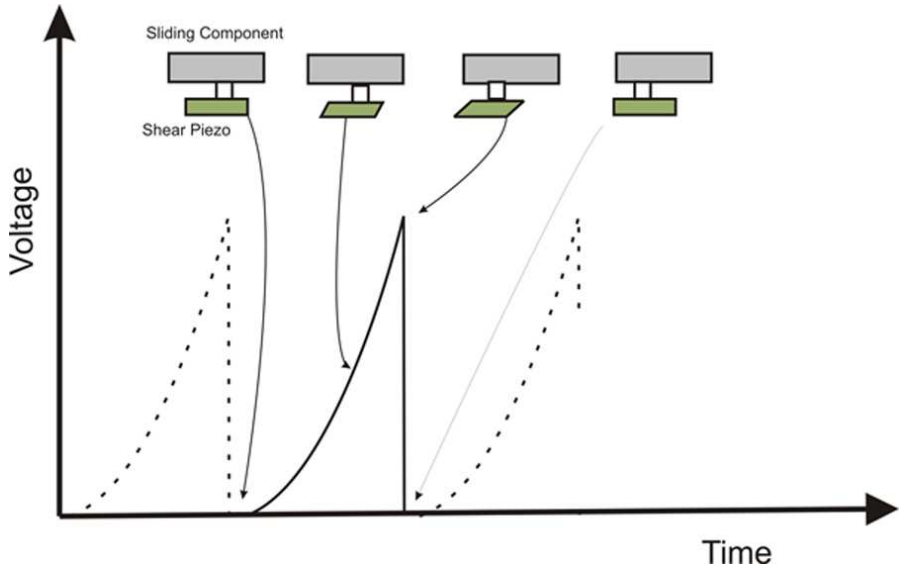

Figure 3.6: The operation of slider for sample coarse approach.

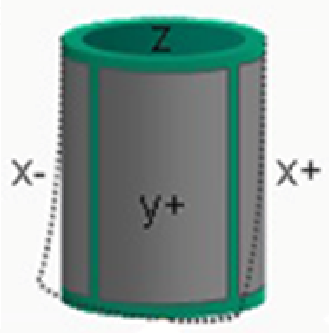

Figure 3.7: Sketch of tube scanner piezo.

effect, the length of a bar of piezo material can be changed by applying a voltage to electrodes attached to its side walls. The standard material for piezoelectric actuators is PZT (lead zirconium titanate). The relative length variation $\Delta l/l$ of a bar is given by

$$\frac{\Delta l}{l} = d_{31}E \tag{3.1}$$

Where E is the electric field across the bar and d_{31} the transverse piezoelectric coefficient. In order to elongate a piezoelectric tube a high-voltage amplifier is necessary to drive the piezoelectric tube electrods. The materials for piezoelectric actuators needs to be polarized with very high voltage to produce the desired effect. This polarization can be lost either gradually after long use, or suddenly when the material is heated above its Curie temperature. The elongation of tube piezoelectric material is used for the vertical movement, while the bending the tube accomplishes the horizontal scanning movement, as shown in Fig. 3.7. For this propose, the outer electrode of the tube is split into four symmetric electrodes along the tube axis. By applying equal but opposite voltages to opposing electrodes the tube will bend due to contraction and expansion of opposite electrodes. The inner wall of the tube is contacted by a single electrode and is grounded . The vertical displacement Δl of the tube scanner can be given by:

$$\Delta l = \frac{d_{31} l U_z}{t} \tag{3.2}$$

here l is the length of the tube, U_z the voltage applied to the inner electrode, and t the wall thickness of the tube. The lateral displacement Δx of the tube

end which is introduced by applying the voltage $-U_x$ and U_x to opposite side electrodes, is given by:

$$\Delta x = \frac{2\sqrt{2}d_{31}l^2U_x}{\pi Dt} \tag{3.3}$$

where D is the average diameter of the tube. The inner electrode of the piezo tube is grounded and the z-voltage is added to the outer electrodes at the four high voltage amplifiers driving the outer electrodes.

The sample is electrically connected by thin polyimide insulated silver wire through the center of piezo tube to the i-v converter. Fine approach of the sample to the tip is achieved by increasing the voltage applied to all four quadrants simultaneously until a tunnelling current is achieved. Gradually changing the applied voltages to the left and right quadrants allows the sample to be scanned across the tip. During the scan line, the feedback loop checks the measured current value and compare it with set current value, if there is a difference between the two then the voltage is applied to the quadrants is changed to move the sample so that the measured value matches the set value. At the end of each scan line the sample is returned to the start point, and the voltage applied to the top and bottom piezo quadrants is incrementally changed, so that the sample can be raster scanned. In STM feedback, the z displacement of piezo is controlled by the feedback circuit to keep the tunnelling current at a specified value and in AFM imaging the force gradient is kept at specified value by the feedback loop circuit.

3.3.3 I-V Converter

The small tunnel current is measured by using a low input current OP-AMP as shown in Figure 3.8. Positive input of OP-AMP(OPA111AM) is grounded and the sample is connected to the negative input. A large feedback resistor, R_f=100 MΩ, is necessary to amplify very low tunnel currents. The output of the converter is then

$$V_{out} = -R_f I_t \tag{3.4}$$

Hence the gain of the amplifier is -100 mV/nA . The amplifier is placed in UHV chamber at the back of sample sample piezo and shielded in a Faraday cage to

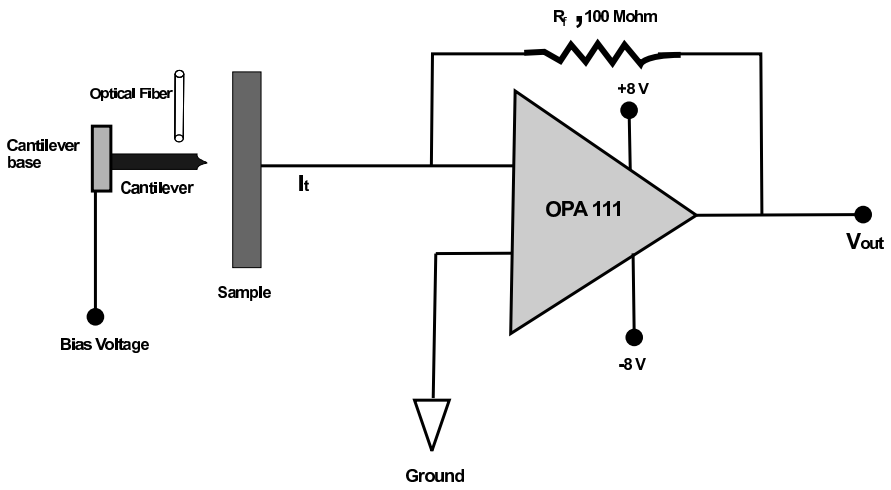

Figure 3.8: The schematic view of I-V converter.

reduce the interference noise from the other signals. The amplifier power supply is set to $\pm$ 8 V to reduce the input bias current and the power dissipation. The backside of Macor sample holder is grounded and a shield is placed over the scanner tube to reduce the coupling between the piezo signals to the tunnel current.

3.3.4 The Fiber Sliders

A fiber slider is used to position the fiber at any point at the side of the special cantilever. The fiber slider consists of two separate sliders which can move and rotate in a plane. Figure 3.9 shows a schematic view of the fiber slider. Similar to the sample slider, the fiber slider has small one side polished ceramic peices glued on top of the shear piezos mounted under the body. The xyθ-slider which is responsible for the motion in horizontal plane, is very similar to the sample slider except for a few minor differences like the positions of the piezos. The xyθ-slider is also able to rotate clockwise and counter clockwise in order to adjust the angle between the fiber and the lever precisely for maximum reflection. The zxϕ-slider which is able to move up and down, rotate clockwise/counterclockwise is mounted on one side of the xyθ-slider. Unlike sample slider and xyθ-slider,

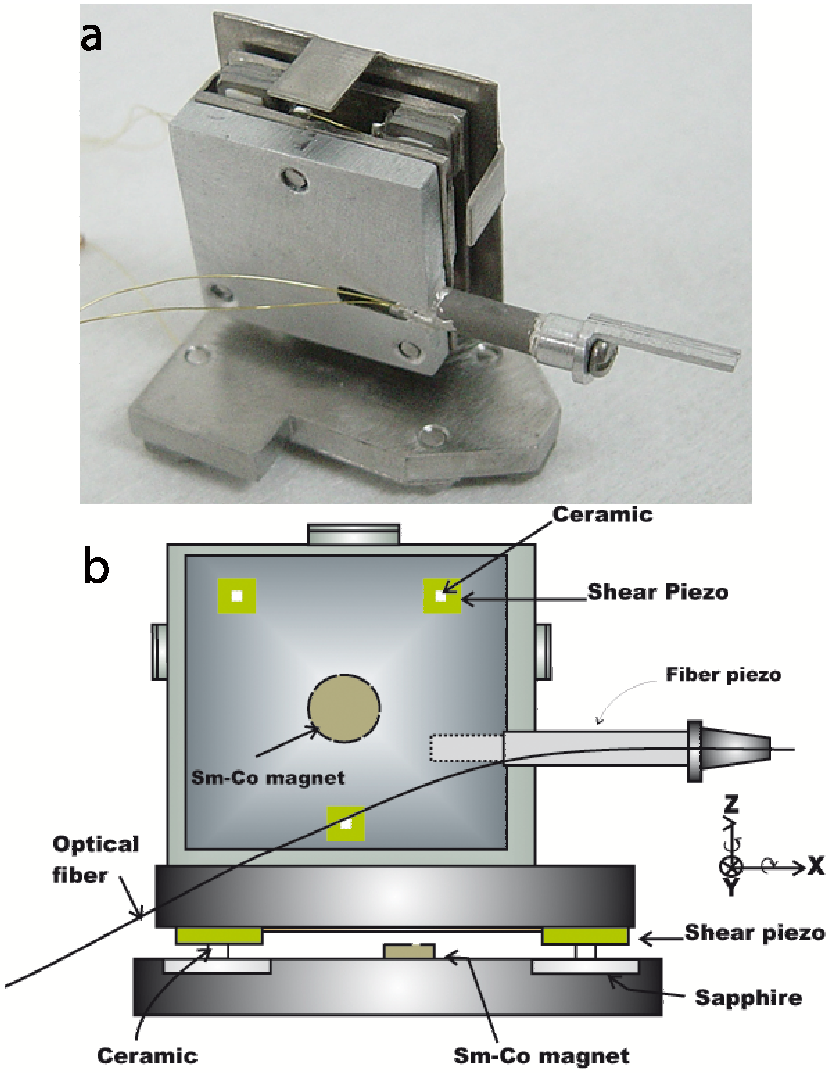

Figure 3.9: (a)The picture and (b) Schematic view of fiber slider

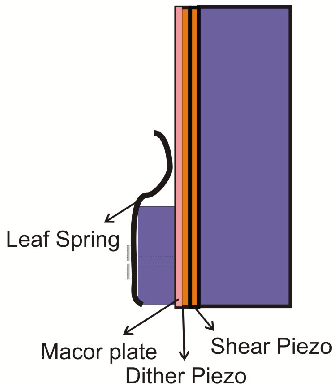

Figure 3.10: The schematic view of cantilever mount

we put three piezos at each position in the zxϕ-slider, since it is relatively more difficult to move a mass upwards against gravity. Two of the piezos at each position is responsible for up/down motion. It can also move in the x- direction, which is quite useful when xyθ-slider is close to its limits in the movement in that direction. The most important feature of the fiber slider is its ability to rotate in two planes, to adjust the angles ϕ and θ the fiber makes with the lever. The fiber itself is mounted on a tube piezo, which is used for fine positioning of the fiber and to keep the instrument at quadrature point. Keeping in mind that the reflecting side of the levers may not be uniform in reflectivity or the levers may be misaligned, a fiber positioner is essential if one desires the ultimate performance from the interferometer.

3.3.5 The Cantilever Mount

A schematic view of the cantilever mount is shown in Fig.3.10. The cantilever holder is kept in place by a leaf spring at the cantilever mount which is in turn fixed to the base plate. Electrical connections are made to the dither and shear piezos to vibrate cantilever in lateral and normal directions with respect to the sample using an A.C. voltage and to the cantilever holder through the contact with the leaf spring in order to apply a D.C. bias voltage. The cantilever is electrically isolated from the piezos by a macor plate.

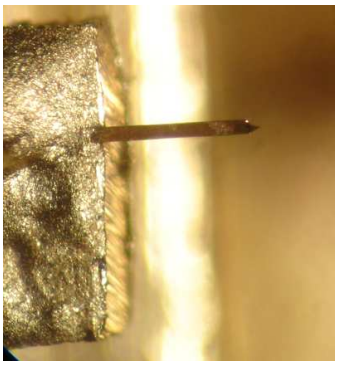

Figure 3.11: A tungsten cantilever on its mount

3.3.6 Cantilever preparation

Home-made tungsten cantilevers have been used in all experiments. because we desire to have metallic cantilever with a spaecial shape, as shown in Figure 3.11. However, in most of other normal and lateral force microscope experiments, scientists prefer to use Silicon microcantilevers. Cantilever quality is one of the most important technical part of the microscope. Preparing the cantilever requires extreme attention and all the steps should be done consciously. We use a specially Tungsten drawn ribbon with the thickness of 0.02 mm and width of 0.1 mm. First, the Tungsten ribbon is cut into around 1.5 cm pieces. The ribbon pieces are electropolished in photographic film developer [132] to enhance the reflectivity. The ribbon wire and platinum circular shape wire put into electrolyte and the wire is kept on positive potential about 20 V, for less than a second. The last step is electrochemical etching of the sharp tip. The tungsten wire is put into a solution of 2 M NaOH or (KOH) and is kept on a positive potential whereas the platinum wire serves as counter electrode. The electrochemical etching setup is shown in Figure 3.12. An electronic circuit developed by NanoMagnetics Instrument Ltd. [128] serves as a power supply and controller for etching process. Once the controller is turned on, the etching starts, the etching process takes place predominately on the surface of the solution. When the neck is thin enough the wire fractures due to its weight, the etching continues till the wire is completely broken. The controller cuts the current as soon as the lower part of the wire

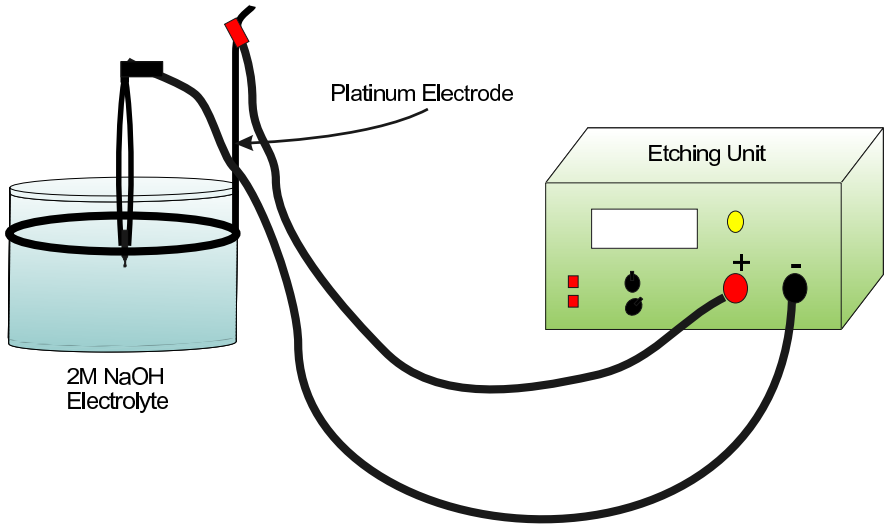

Figure 3.12: The schematic view of tip etching unit

falls off, creating a sharp tip. Tip should be cleaned with deionized water and pure ethanol (or methanol) in order to remove contaminates which come from the etchant. Once the tip is formed and cleaned, the levers are ready to be mounted on their holders. The cantilevers are glued on cantilever holder using a UHV compatible conductive epoxy. After curing the epoxy, the levers are cleaned with Acetone and methanol in ultrasonic bath. In order to enhance the reflectivity of the levers further, the side of prepared cantilever are gold coated. After the coating process, the levers are ready to use in the microscope. Figure 3.13 shows a SEM image of a prepared cantilever.

In order to get quantitative information on force gradient out of recorded data and performed images the stiffness of the cantilever should be known. We have been using geometrical dimension to calculate the cantilever stiffness. We measure the dimension of the cantilever as precise as possible and calculate the stiffness using the expression valid for a rectangular beam:

$$k = \frac{E}{4} w \frac{t^3}{l^3} \tag{3.5}$$

where E is Young's Modulus, w, t, l are width, thickness and length of the lever, respectively. E is 3.1×10^{11} Pa for tungsten. For the typical cantilever with

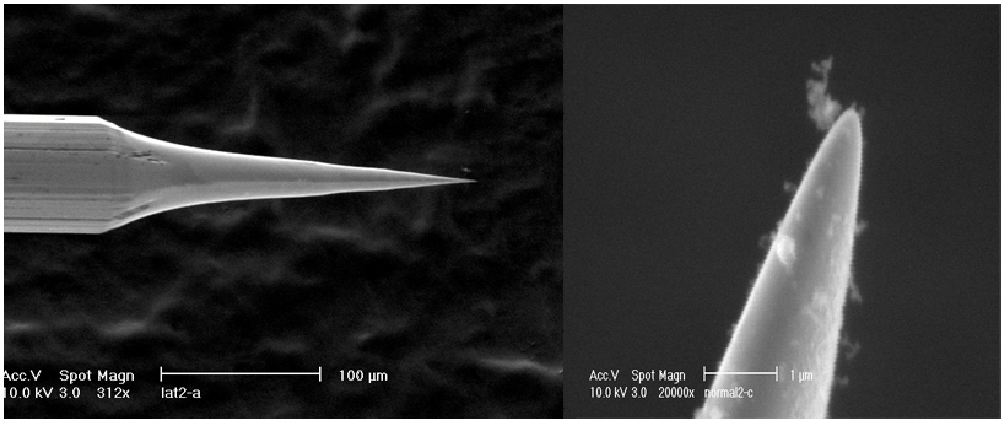

Figure 3.13: SEM picture of typical tip apex

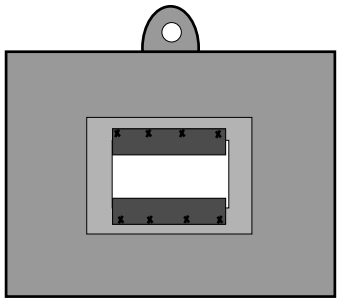

Figure 3.14: The schematic view of sample holder

thickness of 0.02 mm and width of 0.1 mm and length of 0.6 mm, the stiffness of around 100 N/m is calculated.

3.3.7 Sample and Cantilever Holder

Sample holder is a 1 mm thick Molybdenum piece machined in rectangular shape of dimensions 20 × 15 mm as shown in Fig. 3.14. A rectangular hole is punched on which the sample is mounted for direct e-beam heating. Two tantalum leaf spring are spot-welded to the plate to fix the sample. A small hole at the upper part is used to hold the sample holder with magnetic transfer arm and wobble stick enable us to move the sample in UHV chamber. Cantilever holder is a

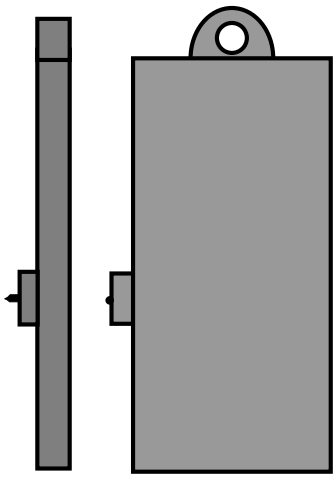

Figure 3.15: The schematic view of cantilever base

specially machined stainless steel piece, which is machined to form a stage for cantilever, the cantilever is glued using conductive epoxy [133] on the stage, so that the apex of the cantilever is pointed to the sample. The schematic view of the cantilever holder is shown in Figure 3.15

3.3.8 Interferometry based force sensing technique

Deflections of the lateral force microscope cantilever is detected by using an all-fiber interferometer. As it is mentioned earlier, the force resolution of the microscope is directly related to the sensitivity of the deflection sensor. Among various types of cantilever deflection measurement, we have chosen to use all-fiber interferometry due to its high sensitivity and relatively easy implementation to UHV . The design of the interferometer which is shown in Fig. 3.16 is very similar to that of Rugar *et al.* [130]. However, the performance is higher than the earlier versions, as a result of some improvements both in the fiber and fiber positioner unit. A single-wavelength, narrow linewidth laser coupled to a single mode fiber with isolators in a semiconductor package is used as a light source.

The laser light is coupled into a single mode 50% directional coupler. One

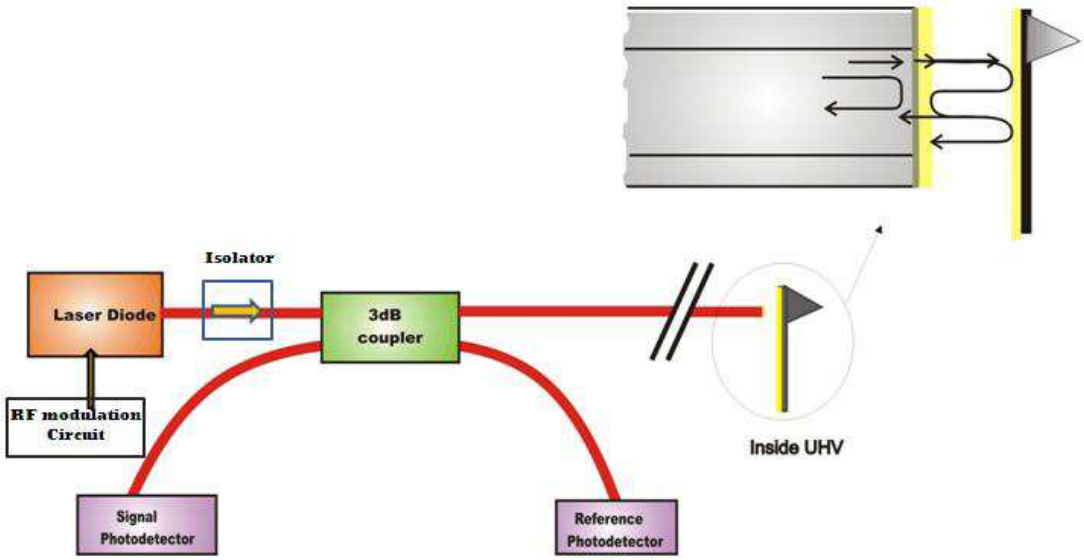

Figure 3.16: The schematic view of the Fabry-Perot interferometer

output of the 3dB coupler is terminated with a reference photodiode used for monitoring the laser power changes and this signal is used for compensating the effect of laser power fluctuations. The light from the other output is carried to the side of our specially designed AFM cantilever. The end of the fiber is cleaved with a commercial fiber cleaver to give a reflection of about 4% from the end. Since the reflected beam from the end of the fiber is used as the reference beam to interfere with the signal, the reflectivity of the fiber end had to be enhanced further. In order to increase the reflectivity, we coated the end of the fiber by evaporation silicon and gold on top of the fiber end. The transmitted beam directed on the cantilever side, reflects back and part of is coupled back to fiber as the signal beam. The coating material thickness had to be chosen carefully, because increasing the reflectivity of the fiber end should not be at the expense of transmission. As shown Figure 3.17 in the simulation using R-soft full wave software, coating of 94 nm Si following by 22 nm of Au gives the optimal reflectivity, and hence the highest interferometer sensitivity.

This combination gives $\sim 55\%$ reflectivity from fiber end. The reference and the signal beams travel through the coupler and interfere at the signal photodiode.

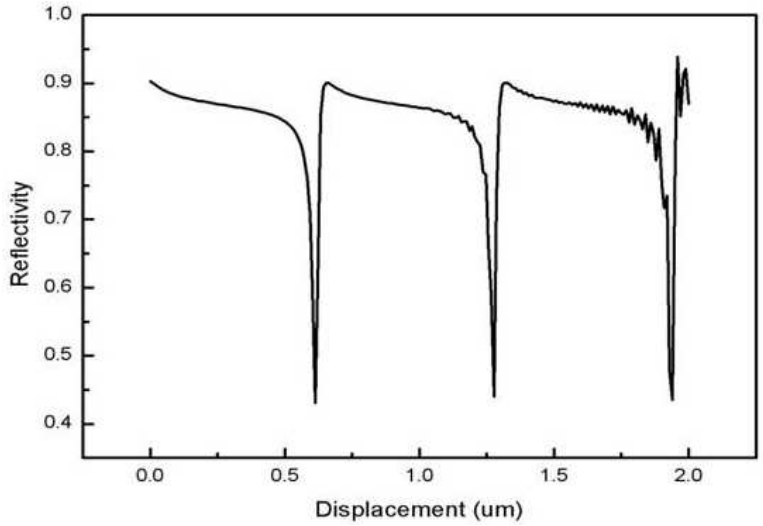

Figure 3.17: Modelling of Fabry-Perot cavity using R-soft full wave software

The photodetector current can be written as

$$i = i_0[1 - V\cos(4\pi d/\lambda)] \tag{3.6}$$

where i_0, V, and d are average current, visibility, and fiber to cantilever separation, respectively. Average current in the photodiode and visibility can be written as

$$i_0 = P_{av}S = (P_r + P_s)S = [R + (1 - A)(1 - R^2]P_0S/4 \tag{3.7}$$

$$V = 2\sqrt{P_rP_s}/(P_r + P_s) \tag{3.8}$$

where P_r, P_s, P_0 and S are reference beam and signal power at the photodiode, laser output power and responsivity of the photodiode, respectively. The most sensitive operating point is at the quadrature where $d = \frac{\lambda}{8}, \frac{3\lambda}{8}, \frac{5\lambda}{8}, ...$ The interferometer is limited by shot noise in the photodiode current, $i_{shot} = \sqrt{2ei_0f}$, where f is the measurement bandwidth. The minimum detectable displacement is then

$$d_{shot-noise} = \frac{\lambda}{2\pi V}\sqrt{\frac{ef}{2SP_{av}}} \tag{3.9}$$

The above derivation is valid for an interference resulting from a single reflection which shows up as a pure sine-wave. If there are multiple reflections provided by

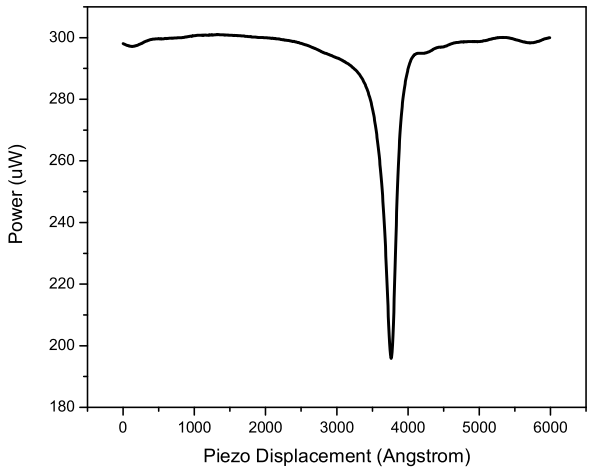

Figure 3.18: Typical interference pattern of the Fabry-Perot interferometer

a cavity, then the photodiode current in Eq.3.10 will be a complicated function of d rather than a cosine [131]:

$$i = i_0[1 - V\mathcal{F}(4\pi d/\lambda)]. \tag{3.10}$$

This modifies the expression for $d_{shot-noise}$ by contributing a factor of m. Hence the expression for our case will be

$$d_{shot-noise} = \frac{\lambda}{2\pi V m}\sqrt{\frac{ef}{2SP_{av}}} \tag{3.11}$$

where m is the ratio of the slope of the interference pattern to that of ordinary interference signal. With the typical figures for the parameters, λ = 1320 nm, V= 0.81, m= 12.5, S= 1 A/W, $P_{av} = 100\mu$ W, e= 1.6×10^{-19}, the shot-noise limit of our interferometer is calculated to be $\sim 6.4 \times 10^{-6}$ Å$/\sqrt{Hz}$. After technical development to reduce the noise, which will be described later. We measured sensitivity of the interferometer is 1×10^{-4} Å$/\sqrt{Hz}$. We may improve the sensitivity further by using higher laser with higher power and better back reflection isolator. A typical interference pattern taken to test the performance of the interferometer is shown in Fig. 3.18. We usually record a few patterns for every cantilever so that we can check the critical parameters such as the slope of the pattern, average power and visibility reliably.

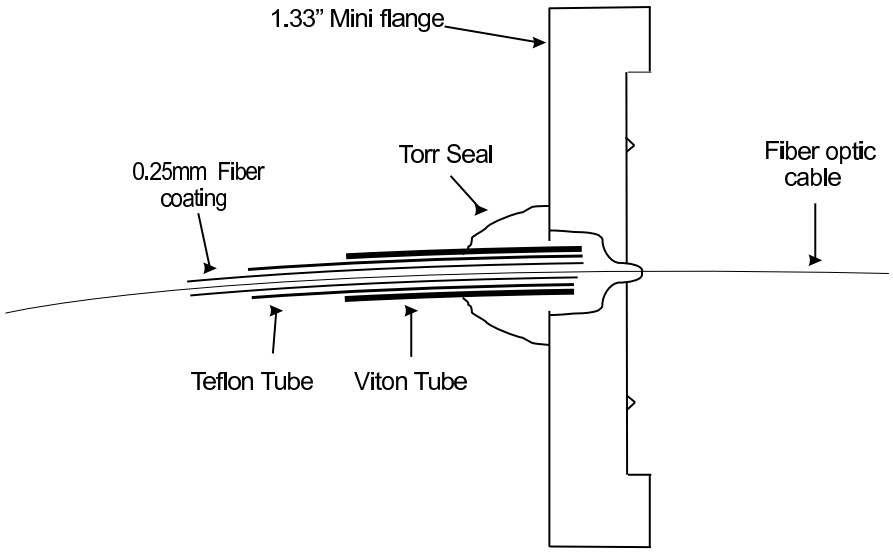

Figure 3.19: The schematic view of the fiber flange

3.3.9 Fiber Preparation for introducing into the UHV chamber

A single mode fibre optic cable which is used to carry the laser light to the back of the lever is mounted on a 1.33" inch CF flange as shown in Figure 3.19. The crucial steps in the construction of the fiber interferometer is the preparation of the fiber itself. We used singled mode fibers with FC/APC connectors at one end. The part of the fiber which goes into the UHV chamber is stripped using a fiber stripper to get rid of the teflon cover and plastic coating. The plastic protection of the adjacent section of about a meter which resides in the bakeout oven is stripped and then put in a PTFE tubing so as to withstand temperatures of up to 150 °C during bakeout. The fiber is glued on a mini UHV flange after feeding the fiber through the 0.5 mm diameter hole at the centre of the flange. Only the fully stripped section of the fiber is left on vacuum side of the flange. We glue and seal the fiber on the flange using UHV Torr seal. The fiber has three protective layers, a viton outer layer, a 900 micron layer and a 250 micron cladding layer. The silica fiber itself is 125 microns in diameter and the fibre core is 10 microns in diameter. To be UHV compatible, only bare fiber can be

exposed to the vacuum so the protective coatings have to be stripped from the fibre. Outside the chamber the fibre coatings need to be able to withstand the 'bake out' temperature of 155°C. The outer layer has to be removed for about 1 m from the flange, and is replaced by a teflon tube which can withstand 160°C. The region where the fibre meets the flange is strengthened against breaks by supporting the fibre with a piece of viton tubing. The fibre is fed through the hole in the flange and glued in place with the tubing using Torr Seal, which gives a vacuum compatible seal to the hole, and allows bake out to 100°C. Since the 'bake out' temperature is 155 °C the fiber flange is cooled by running water through a copper tube mounted fixed to the flange. The next step is the preparation of the cantilever end of the fiber. The fiber end is cleaved with a commercial cleaver as to end up with a reflection of about 3-4% after a few trials. Then fiber is coated using thermal evaporator. We use Si-Au two layers coating. Firstly the Si is evaporated while the reflectivity up to an optimum thickness around 90 nm and then the thin layer of gold on top of Si layer will be coated. Typical thickness of gold layer is around 20 nm. The gold coating caps the silicon layer and provides a mirror so that multiple reflections can occur between the back of the lever and the fibre. The internal reflection is monitored during the evaporation process by having the fibre connected to the electronics, and monitoring the voltages from the signal and reference photodiodes using the photodiode card in the control electronics. When deciding how much internal reflection would be needed, we first assumed that half the light that left the fibre end would be coupled back into the fibre, so an internal reflection of around 55% was chosen. In addition to increasing the amplitude of reference signal, the gold layer, more importantly, forms a kind of Fabry-Perot cavity with the back of the cantilever and amplifies the signal beam considerably as a result of multiple reflections.

3.3.10 AFM Electronics and Control System

The AFM is controlled by a personal computer through an AFM Electronic Control unit developed by NanoMagnetics Instrument Ltd. [128]. The control electronics consists of eight PCB cards. There is a power supply card which supplies

+5 V, ∓8 V, ∓15 V, ∓220 V, +450 V to the other cards, a HV amplifier card to supply voltages to the sample scanner piezo quadrants, a slider card to supply the voltage pulses to the sliders shear piezos, a interferometer card that contains the laser diode, the coupler and the two photodetectors, an analogue to digital converter card, a digital to analogue converter card which supplies various voltages under computer control, and the analog feedback control which regulates the tip sample separation. All the functions of electronics are controlled through the software in C^{++} developed by NanoMagnetics Instruments Ltd. , and has been specially developed to control the microscope. The program performs automatic sample approach, imaging , as well as various image processing algorithms, in order to analyse the data. Coarse approach of the sample to the tip is controlled the setting the frequency and duration of the voltage pulses to the shear piezos and using a joystick connected to the electronics to select the direction of motion. The fine approach of the sample to the tip is automatically controlled by computer. Before automatic approach is started, the feedback loop gain is usually set to its maximum value, the number of voltage pulses per cycle is set so that the slider moves forward a shorter distance than the maximum piezo extension. This prevents crashing the tip into the sample during approach. The approach involves the following steps: the tube piezo is extended until it reaches its full extension or a tunnelling current is found, if no tunnelling current is found the tube piezo is fully retracted, a number of steps are made by slider and then the piezo is extended again, this procedure is repeated until a tunnelling current is found. If the AFM mode is being used, the feedback signal comes from lock-in amplifier, which measure the lever vibration amplitude, and the approach stops when a set force gradient is found. The program can record interference patterns and display them on screen, and the patterns can be saved. The details of the maximum and minimum power, the visibility, and the power at the signal and reference photodiodes are displayed on screen. The slope of the interference pattern is also displayed. The program can also be set to keep the interferometer at the quadrature point. To do this the computer records an interference pattern and calculates the quadrature point. The fiber piezo is used to keep the fiber at the position which keeps the laser power at the same value as at the measured quadrature point. For imaging, number of parameter need to be set. The tip

bias voltage, set tunnelling current and feedback loop gain can all be set via the software, the position of scan area can be controlled by using offset voltages. The pixel size of the images can be set manually in a 128×128, 256×256 or 512×512 matrix form and a automatic routine is used to record images. The software allows many channels to be recorded and the gain for each channel can be set separately. If the scan parameters are to be kept constant for number of scans, there is also an option, that checks the tip-sample position whether it is within tunnelling range or not. If the sample is too close or too far from the tip, then an appropriate numbers of step is made by the slider to bring the sample within the optimal range, where a small z-voltage is applied to the tube piezo. Keeping the voltage applied to the tube piezo close to 0 V reduces the amount of piezo creep. Cross section of the images also can also be plotted, which gives better idea about surface corrugation. The I-V and force-distance curves can also be acquired.

3.4 Noise Analysis

Scanning Tunneling Microscopes and Atomic Force Microscopes are used to measure very small tunnel current, force or force gradient between a very sharp tip and a sample. The signal to be measured is weak, therefore, utmost attention should be given to the system noise. In the following sections the noise consideration and attempts towards reducing the noise levels to achieve the highest possible sensitivity will be described.

3.4.1 General Discussion of Noise

A noisy physical variable, $Y(t)$, can be written as a sum of two terms:

$$Y(t) = Y_0 + \delta Y(t) \tag{3.12}$$

where $Y_0 = Y(t)$ is the average value defined as

$$\langle Y(t) \rangle = \lim_{t' \to \infty} \frac{1}{t'} \int_{t_0}^{t_0 + t'} Y(t) dt \tag{3.13}$$

and $\delta Y(t)$ is the noise term. The spacial density of noise, $W_Y(\omega)$, where ω is the operation frequency, is defined by

$$W_Y(\omega) = \lim_{t' \to \infty} \frac{1}{t'} | \int_0^{t'} \delta Y(t) \exp(-i\omega t) dt|^2 \tag{3.14}$$

It can be shown that the mean square of the noise is given by

$$\langle \delta Y^2(t) \rangle = \lim_{t' \to \infty} \frac{1}{t'} \int_{t_0}^{t_0 + t'} Y(t) dt \tag{3.15}$$

The noise, which passes through a filter that has a bandwidth of B and transmission of unity around the center frequency ω, is a widely used definition of noise is given in terms of the relative intensity noise (RIN), defined by an advantage of using the RIN is that the contributions from different noise sources are additive.

3.4.2 Noise associated with STM

The tunnelling current is measured with a current to voltage converter as explained in previous section, which is usually with a single operational amplifier with low noise, low input bias current and feedback resistor with a typical impedance of R=100 MΩ. The tunneling current I_t is used to measure the distance between tip and sample. The noise in the tunneling current in the case of STM needs to be small enough to ensure that the corresponding vertical noise δz is considerably smaller than the atomic corrugation of the sample. In the following, the noise level for he imaging signals and vertical positions are described by the root-mean-square (rms) deviation of the mean value and indicated by prefix δ, i.e.,

$$\delta \xi = \sqrt{\langle (\xi - \langle \xi \rangle)^2 \rangle} \tag{3.16}$$

In order to achieve atomic resolution, a first necessary condition is that the mechanical vibrations between tip and sample are smaller than the atomic corrugations. This condition is met by a microscope design emphasizing outmost stability and establishing proper vibration isolation. The inherent vertical noise in STM in connected to the noise in current measurement. Because the measurement of

I_t is subject to noise, the vertical distance measurement is also subject to a noise level δz:

$$\delta z = \frac{\delta I_t}{|\partial I_t/\partial z|} \tag{3.17}$$

It is shown below that the noise δI_t in the tunnel current is the Johnson noise of the feedback resistor, R in the current amplifier, the Johnson noise in the tunneling region, and the input noise of the operational amplifier. The Johnson noise density of a resistor R at temperature T is given by:

$$n_R = \sqrt{4k_BTR} \tag{3.18}$$

where k_B is Boltzmann constant. In typical STMs, the tunneling current is of the order of $I_t \approx 100pA$ and measured with an bandwidth of $B \approx 1kHz$. with a gain of V/I=R = 100 MΩ and T=300 K, the rms voltage noise is $n_i = \sqrt{B} = \sqrt{4k_BTRB} = 40\mu V$ at room temperature, corresponding to a current noise of $\delta I_t = 0.4pA$ and the vertical noise shown as:

$$\delta z \approx \frac{\sqrt{4k_BTB}/R}{2\kappa_t|I_t|} \tag{3.19}$$

which amounts to a z-noise of 0.2 pm in the present example. Thus in STM, the noise in tunelling current is not a problem, because it is much smaller than the required resolution.

3.4.3 Mechanical noise consideration

Mechanical vibrations are source of noise to achieve high-resolution measurements. Since sub-Ångstrom noise amplitudes are measured in STM/nc-LFM a very accurate vibration isolation is necessary to for proper operation of the microscope. The vibration amplitude of the ordinary laboratory floors are of the order of a micron. Among various methods used by scientists for this purpose, spring suspension system with eddy current damping has been used for the vibration isolation. Base of the microscope is suspended with four stainless steel springs from four posts screwed on the flange. The springs are mounted on adjustable collars to balance the microscope. There are four Sm-Co magnets clamped to a

stainless ring which rests on collars tightened to the posts. Viton O-rings are cut and placed under the magnet holding ring to reduce the vibration which can be coupled to the base. These magnets together with the copper plates mounted on the microscope base are used for eddy current damping.

3.4.4 Thermal Cantilever Noise

The cantilever of a atomic force microscopy acts as an isolated one-dimensional harmonic oscillator having energy

$$E = \frac{1}{2}m(\frac{\partial z}{\partial t})^2 + \frac{1}{2}m\omega_0^2 z^2 \tag{3.20}$$

where z is the detection of the free end of the cantilever,m is the effective mass of the cantilever and $\omega_0 = (\frac{k_0}{m})^{\frac{1}{2}}$is the resonant frequency (k_0 is the spring constant) The total thermal energy of such an one-dimensional harmonic oscillator is k_BT The spectral density of the thermal z-position noise of this free-running cantilever is

$$W_{Vz}(\omega) = |G(\omega)|^2 \Psi_{th}(\omega) \tag{3.21}$$

where

$$|G(\omega)|^2 = \frac{1/m^2}{(\omega_0^2 - \omega^2)^2 + (\omega_0\omega/Q)^2} \tag{3.22}$$

is the response function of the cantilever(damped harmonic oscillator) and

$$\Psi_{th} = 2m\omega_0 k_B T/Q \tag{3.23}$$

is the thermal white noise.Here Q is the quality-factor of the damped harmonic oscillator. Because the strength of the thermal white noise(Ψ_{th})decreases with increasing Q, high-Q cantilevers have less thermal noise off resonance. The cantilever thermal noise acts as the optical path length noise of one arm of an interferometer. Assume the optical powers from the two arms are equal and the two optical waves have a phase shift of $\frac{\pi}{2}$, we can show the maximum current noise (spectral density) generated on a photo-detector is given by

$$W_i(\omega) = (\frac{4\pi}{\lambda}\eta P_0)^2 W_z(\omega) \tag{3.24}$$

3.4.5 Noise associated with cantilever deflection sensing

An Atomic Force Microscope consists of a lever integrated with a sharp tip, deflection sensing unit, and piezoelectric element to vibrate the cantilever. Each parts contributes noise to the system. We mentioned that for an ideal interferometer the minimum detectable deflection is limited by shot-noise in the photodetector. However, practically there are other sources of noise which exceeds shot-noise and hence degrades the sensitivity of the interferometer and therefore cantilever deflection sensing. In this section, we focus on the primary sources of laser diode noise including shot noise, intensity, and phase noise which is converted into amplitude noise in an interferometer configuration. Then a measurement from the noise of our interferometer, which clarify the fact that the measured sensitivity of our interferometer is considerably below the ideal sensitivity limited by shot noise. All fiber interferometer is a kind of Differential Homodyne detection system in which the beam is transferred throughly with a fiber. The homodyne detection system suffers from effects of drift in the optical path length d_0, which in our case is the gap between the fiber end and the lever. Since the relative thermal drift $\Delta d/d \propto \Delta T$, where ΔT is the temperature variation, Δd can be minimized by a routine which keeps the fiber at quadrature point. Another kind of noise is the Johnson noise generated by the photodetector which shows up a fluctuations in the current as

$$\langle \Delta i_1^2 \rangle_J = 4k_B T B/R \tag{3.25}$$

where k_B is the Boltzmann constant, T is the temperature, and B is the measurement Bandwidth. The Johnson noise is small in comparison to other noise contributions, hence can be neglected. The noise in the semiconductor diode laser, is one of the main contributions to the overall interferometer. The dominant noise in our optical configuration of our interferometer is due to intensity variation, mode switching, and the phase noise which can only be present when two optical waves with different optical path lengths recombine. In our case, the back reflected laser wave from the fiber end and the optical wave reflected form the cantilever side recombination have created the phase noise which caused the power fluctuations of the laser diode. This problem was suppressed by adding an

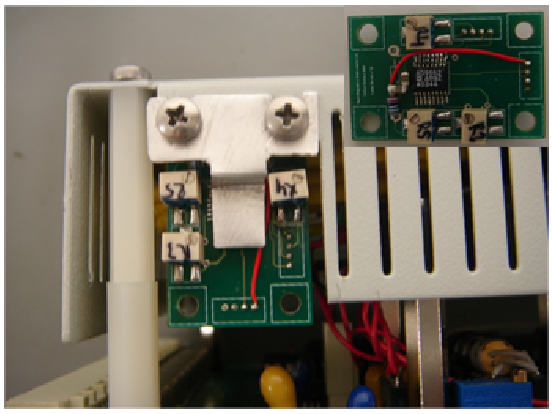

Figure 3.20: The picture of RF modulation circuit

isolator at the laser output and injecting radio frequency (RF) modulation, as shown in Figure 3.20 to the output of the laser driver.

This minimizes the influence of back reflections into the laser diode by decreasing the coherence length. The amplitude and the frequency of the RF current can be adjusted using two potentiometers to optimize noise level. The good choice of the laser diode and additional components such as optical isolators after the laser also resulted in signal to noise enhancement. The current noise of the laser generated by each photodetector is defined as

$$\langle \Delta i_1^2 \rangle_L = S^2 P_{pd1}^2 RIN \tag{3.26}$$

$$\langle \Delta i_2^2 \rangle_L = S^2 P_{pd2}^2 RIN \tag{3.27}$$

Where S is the responsively of photodiode, $P_{pd1,pd2}$ is the power incident on photodiode, and RIN is the relative intensity noise, which is defined as

$$RIN_{int} = 10log[\frac{\langle \Delta P^2 \rangle}{\langle P \rangle^2}](dB) \tag{3.28}$$

The dominant source of noise in the laser diodes is the spontaneous emission. The laser diode, which behaves like a thermal source, we have to take into account the mode-partition noise, mod switching noise, and $1/f$ noise. Practically, we can

use the specifications accompanying a laser diode that give the RIN measured in a given bandwidth around a center frequency. We measured the relative intensity noise, RIN, of the laser diode to be RIN_{int}=-120 dB.

The noise corresponding to the laser intensity noise can be expressed as

$$\langle \Delta V^2 \rangle_{int}^{1/2} = SP_0R\sqrt{RIN_{int}} \tag{3.29}$$

Where P_0 is the average power on the photodiode, and R is the load resistor.

The intensity noise of a multimode laser is much smaller than that of a single mode laser because of negative cross-correlation effects that exist between the different modes. Phase noise is another important contribution to the laser diode noise. Fluctuations in the phase of a optical wave passing through a interferometer can be translated into intensity noise on a photodetector.

As mentioned before, the shot-noise limit of our interferometer is very low, and depends on the quality of the lever. Consequently, the sensitivity changes with different levers. We carried out measurements with a certain lever to figure out noise characteristics of the interferometer and characterize the lever. In order to make quantitative analysis of the force/force gradient data obtained, one has to know parameters such as the spring constant and resonance frequency of the cantilever. We investigated the power dependence of noise in V_{PD}. We measured signal to noise ratio of V_{PD} signal out of lock-in amplifier at different laser power levels ranging from 0.8 mW to 5 mW. We found the optimum signal to noise level can be achieved at laser power of around 1.9 mW. We recorded Fast Fourier Transform (FFT) spectra of the V_{PD} output and by injecting Radio frequency modulation and optimized the signal to noise level, as shown in Figure 3.21

In order to check the effect of mechanical vibration of the microscope on the overall noise of the interferometer, we disabled the vibration isolation mechanism by locking the microscope. There was no considerable difference in the noise spectrum compared to the measurements done while the vibration isolation mechanism is on.

We performed another experiment to measure the center wavelength and the

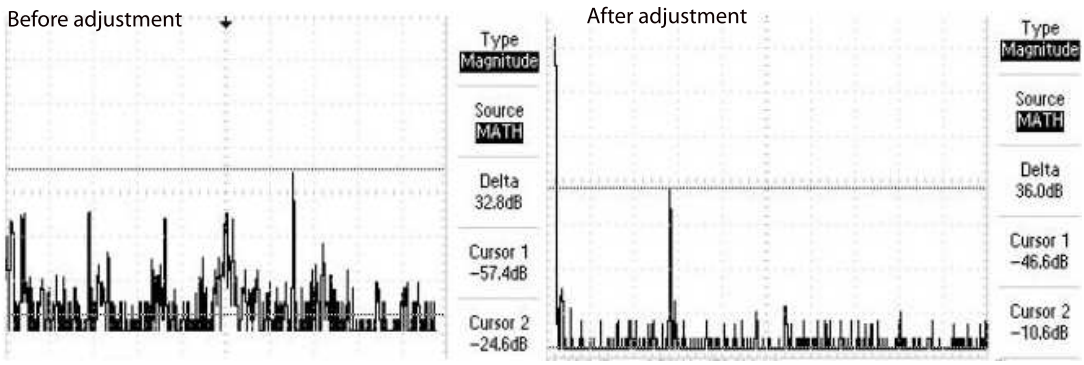

Figure 3.21: FFT spectra of V_{PD} before and after RF modulation current injunction to the laser diode

line-width of the laser diode using ADVANTEST Q8384 Optical Spectrum Analyzer. We measured the power versus wavelength of the laser diode when the RF is turned on and off as shown in Fig.3.22. Measurement is acquired with a laser power of 1.9 mW, which is the optimal power value used in almost all experiments. Wavelength spectrum shows that when the RF is on, laser become more of a multimode laser than the single mode one, because of negative cross-correlation effects that exist between the different modes, The rms spectral with, $\Delta\lambda$, of the laser was found to be about 0.03 nm.

The current noise in the signal photodiode for the case of multiple beam interference, mainly consist of the noise in laser power$[1 - V\mathcal{F}(\frac{4\pi d}{\lambda})]\Delta i_0$, changing in the optical path length $i_0 V m \frac{4\pi}{\lambda}\Delta d$ and the wavelength fluctuation $i_0 V m (4\pi d)\frac{\Delta\lambda}{\lambda^2}$.

The derivative of the$\mathcal{F}(\frac{4\pi d}{\lambda})$ is considered to be the slope of the interferometer pattern, and the value of Δd needs to be measured from the experiment. Since the major contribution to the change in optical path length is the deflection of cantilever. The main attempt in noise analysis is to find out the relative contribution of different noise sources to the noise in measured quantity, Δd. Moreover, it should be considered that the fluctuations in the laser power is also effective source of noise. In order to calculate the change in optical path length due to power noise of the laser, we can relate the noise in the cantilever deflection

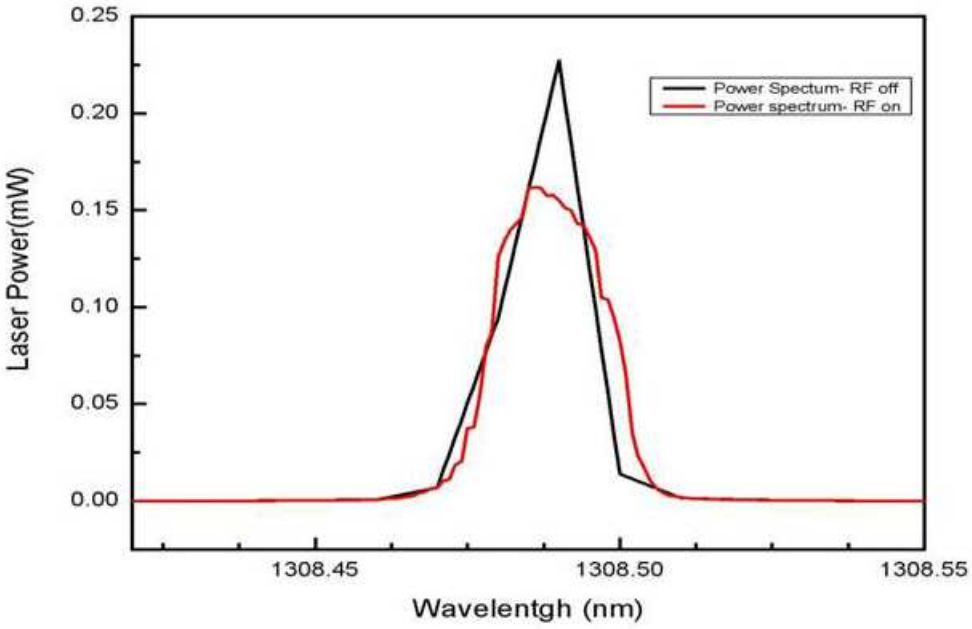

Figure 3.22: Power spectrum of the laser diode

measurement as :

$$\Delta d \approx \frac{1 - V\mathcal{F}(\frac{4\pi d}{\lambda})}{Vm4\pi/\lambda}(\frac{\Delta i_0}{i_0}) = \frac{(i/i_0)}{Vm4\pi/\lambda}(\frac{\Delta i_0}{i_0}) \tag{3.30}$$

For typical quantities of interferometer parameters, λ=1309 nm, V= 0.22, m=10 and $\frac{\Delta i_0}{i_0}$= 1.5×10^{-6} the noise in the deflection of cantilever is calculated to be $\approx 1 \times 10^{-4}$ $\mathring{A}/\sqrt{Hz}$. The measurement has done with a cantilever at frequency of 7.27 kHz which is far below the resonance frequency of 16.848 kHz. This noise level is low enough to allow measurements at the atomic resolution.

3.5 Noise-limited Sensitivity of Microscope

We have translated independent sources of noise into current noise and voltage noise on a photo-detector.The total mean square of current noise is the sum of all possible sources and can be denoted as:

$$\langle \delta i^2 \rangle_{thotal} = \langle \delta i^2 \rangle_{shot} + \langle \delta i^2 \rangle_{int} + \langle \delta i^2 \rangle_{phase} + \langle \delta i^2 \rangle_{Johnson} + \langle \delta i^2 \rangle_{th} + ... \tag{3.31}$$

The total mean square of voltage noise across a load resistor is given by

$$\langle \delta V^2 \rangle_{total} = \langle \delta i^2 \rangle_{total} \times R^2 \tag{3.32}$$

3.5.1 Minimum Detectable Force

In contact mode operation of a Scanning Force Microscope.,The static detection of a cantilever caused by the repulsive force between the force-sensing tip attached to the free end of a cantilever and sample surface is measured. The force F and the detection of the cantilever Δz obey the Hooke's law

$$F = k_0 \Delta z \tag{3.33}$$

Here k_o is the spring constant of the cantilever which has a typical value range of 0.01-200 N/m. Under favorable conditions (the two optical waves have equal optical power and phase shift of $\frac{\pi}{2}$ at zero deflection of the cantilever, the deflection of the cantilever produces a current change on a photo-detector given by

$$\Delta i = \langle \delta i^2 \rangle = \frac{4\pi}{\lambda} \eta P_0 \Delta z \tag{3.34}$$

whereλ is laser wave length ,η is quantum efficiency and P_0 is initial laser power. The minimum detectable force F_{min} is defined by the equation

$$\Delta i = \langle \delta i^2 \rangle_{total}^{\frac{1}{2}} \tag{3.35}$$

from which we get

$$F_{min} = k_0 \frac{\lambda}{4\pi\eta P_0} \langle \delta V^2 \rangle_{total}^{\frac{1}{2}} / R \tag{3.36}$$

where R is the load resistor on the photo-detector. So the minimum detectable force F_{min} is proportional to the spring constant of the cantilever and total noise level but inversely proportional to laser power.

Chapter 4

Results and Discussion

In this chapter, we shall describe the torsional mode dynamic AFM imaging of Cu-tetra-3,5 di-tertiarybutylphenyl porphyrin (Cu-TBPP) molecules on Cu (100) surface and results from small oscillation amplitude lateral ncAFM I built.

4.1 Simple calculation of Lateral contact stiffness

In Section 2.4 we explained a number of lateral force measurement experiments. Now, we examine how the the lateral contact stiffness is measured, in detail. This approach will enable us to compare between the accuracy of the lateral force measurement in contact mode and dynamic mode. Figure 4.2 shows the cantilever in torsional vibration in contact with surface. The lateral motion of the base of cantilever,$A_{0,lat}$, is caused by the torsion and lateral bending of the cantilever, A_t and A_b respectively, as well as deformation of tip-surface contact, A_c. The base of the cantilever is oscillated sideways with an amplitude $A_{0,lat}$, which, if the tip does not slide over the surface, is accommodated by elastic deformation of the tip-surface contact, A_c, torsion of the cantilever, A_t, and lateral bending of the cantilever, A_b. A_t is found from the measured amplitude at frequency f_L

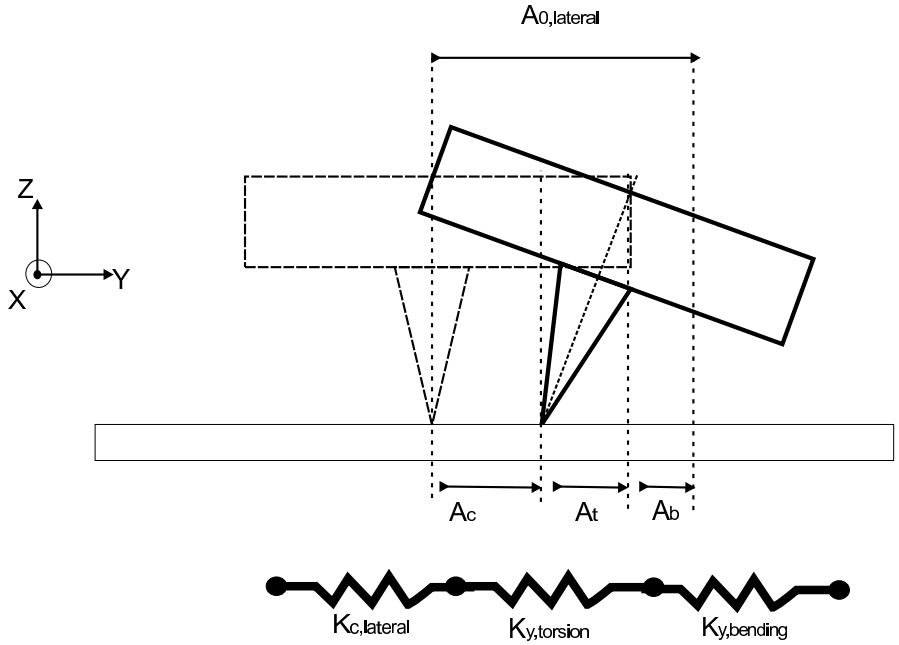

Figure 4.1: The Schematic view of a custom-made cantilever in contact mode

from the geometry of the cantilever and the position of the point of measurement. The lateral stiffness of the tip-surface contact is denoted k_L, which is assumed to be constant. The torsional and bending stiffnesses of the cantilever are denoted $k_{y,torsion}$ and $k_{y,bending}$ respectively, and can be calculated from the geometry. We ignore the effects of damping, so the system can be modelled as three springs in series at equilibrium. The force in each 'spring' must be equal, so we have

$$A_t k_{y,torsion} = A_c k_{c,lateral} \tag{4.1}$$

and

$$A_t k_{y,torsion} = A_{cb} k_{c,bending} \tag{4.2}$$

therefore the applied oscillation amplitude $A_{0,lat}$is given:

$$A_{0,lat} = A_b + A_t + A_c \tag{4.3}$$

combining Equations 4.1, 4.2, 4.3 we obtain the following equation of k_L:

$$k_L = \frac{A_t k_{y,torsion} k_{y,bending}}{A_{0,lat} k_{y,bending} - A_t(k_{y,bending} + k_{y,torsion})} \tag{4.4}$$

This gives us the lateral contact stiffness in terms of measurable parameters. As above equation implies, bending stiffness also should be taken in to account to able to have more realistic measurement of lateral force stiffness. this is difficult to quantify and it is dependent on normal load on cantilever.

4.2 nc- Lateral Force Microscope Operation

In the following section, we describe how lateral forces acting between tip and sample and even molecules on the surface can be measured. The challenges faced by dynamic mode lateral force microscopy are similar to those faced by dynamic mode normal force microscopy. In dynamic operation modes, the cantilever deliberately vibrated parallel to the surface and therefore frequency modulation Atomic force microscopy(FM-AFM) and off resonance amplitude modulation Atomic Force Microscopy appear to be the natural choices for pursuing nanometer scale and even atomic resolution in lateral force microscopy. In this thesis the measurements are performed by two methods; (a) frequency shift method in dynamic mode (b) small oscillation amplitude ncAFM method.

4.2.1 Frequency Modulation Lateral Force Microscopy: Torsional Mode

In frequency modulation torsional mode lateral force microscopy, a cantilever with torsional eigenfrequency f_{tors} and spring constant k_{tors} oscillates with a constant amplitude A, as shown in Fig.4.3. The deflection signal is phase shifted, routed through an automatic gain control (AGC) circuit and fed back to the piezo actuator. The frequency f is a f_{tors}, its quality factor Q, and the phase shift φ between the mechanical excitation generated at the actuator and torsional deflection of the cantilever. If $\varphi = \frac{\pi}{2}$, the loop oscillates at $f = f_{tors}$. Lateral forces between tip and sample cause a change in $f = f_{tors} + \Delta f$. If the second derivative $k_{ts} = \frac{\partial^2 u_{ts}}{\partial z^2}$ of the tip-sample potential is constant for the whole range covered by the oscillating cantilever, the shift in the torsional frequency that

occurs is given by:

$$\Delta f = \frac{f_{tors}}{2k_{tors}} k_{ts} \tag{4.5}$$

The path of the cantilever can be expressed by $y'(t) = Acos[\alpha(t)]$ where the phase velocity is given by $\dot{\alpha} = 2\pi[f_{tors.} + \Delta f(t)]$. For a sinusoidal modulation of $\dot{\alpha} = 2\pi[f_{tors.} + \Delta f_{tors.} + \Delta cos(2\pi f_{mod} t')]$ the torsional deflection $y'(t)$ is given by

$$y'(t) = Acos[2\pi(f_0 + \Delta f_0)t] + \frac{\Delta}{f_{mod}} sin(2\pi f_{mod} t) \tag{4.6}$$

which leads to a frequency spectrum centered at $f_0 + \Delta f_0$ and an infinite number of subbands spaced by integer multiples of the modulation frequency f_{mod}. Fortunately, the n subband drops rapidly. It is given by $J_n(m_f) \times A$ where J_n is a Bessel function of the first kind and order n, and $m_f = \Delta / f_{mod}$ is the modulation index. For practical purposes, the required bandwidth is given by Carson's rule.

$$B = 2(\Delta + f_{modmax}) \tag{4.7}$$

where Δ is the deviation of the frequency setpoint and f_{modmax} is its maximal modulation frequency. Carson's rule has an important consequence for FM-AFM: only the noise of the cantilever deflection signal which lies within a frequency interval [$f_{tors.}$-B,$f_{tors.}$+B] contributes to the noise at the output of the FM demodulator. The oscillator circuit is critical component in FM-AFM. The function of this device is best understood by analyzing the cantilever motion. The cantilever can be treated as a damped harmonic oscillator that is driven externally. For sinusoidal excitations $A_{drive} e^{i2\pi f_{drive} t}$ and $Q \gg 1$, the response of the cantilever deflection is

$$\frac{A}{A_{drive}} = \frac{1}{1 - \frac{f_{drive}^2}{f_{tors}^2} + \frac{i f_{drive}}{f_{tors} Q}} \tag{4.8}$$

The absolute value of the amplitude is given by

$$|A| = \frac{|A_{drive}|}{\sqrt{1 - \frac{f_{drive}^2}{f_{tors}^2} + \frac{f_{drive}^2}{f_{tors}^2 Q^2}}} \tag{4.9}$$

and the phase angle between the driving and resulting signals is

$$\varphi = arctan[\frac{f_{drive}}{Q f_{tors}(1 - f_{drive}^2 / f_{tors}^2)}] \tag{4.10}$$

in the case of closed feedback loop, the driving frequency can no longer be chosen freely but is determined by f_{tors}, Q, the phase shift φ and the tip-sample lateral forces. The purpose of the oscillator circuit is to provide controlled feedback with a phase angle of $\varphi = \frac{\pi}{2}$ such that the cantilever oscillates at a constant amplitude.

Conservative tip-sample lateral forces cause a frequency shift. A non-conservative component in the tip-sample force, that is hysteresis in the force versus distance curve,

$$\Delta E_{ts} = \oint F_{ts}(z + z')dz' \tag{4.11}$$

causes extra dissipation in in the motion of cantilever. When the tip of the cantilever is far from the sample, the damping of the cantilever is due to internal dissipation and the energy loss per oscillation cycle is given by

$$\Delta E_{CL} = 2\pi \frac{E}{Q} \tag{4.12}$$

Where $E = kA^2/2$ is the energy of the cantilever and Q is its quality factor. When the phase angle between the excursion of the actuator and the excursion of the cantilever is exactly $\varphi = \pi/2$, the cantilever oscillates at frequency f_0 and the driving signal is $A_{drive} = Ae^{i\pi/2}/Q$. Hence, the driving amplitude can be written as:

$$|A_{drive}| = |A| \frac{\Delta E_{CL}}{2\pi E} \tag{4.13}$$

When the tip oscillates close to the sample, additional damping occurs and the driving signal A_{drive} is increased by the oscillator control electronics to A'_{drive} to maintain a constant amplitude A, where

$$|A'_{drive}| = |A| \frac{\Delta E_{CL} + \Delta E_{ts}}{2\pi E} = |A|(\frac{1}{Q} + \frac{\Delta E_{ts}}{2\pi E}) \tag{4.14}$$

Measuring the damping signal yields the dissipation in the approach and retract phases of the oscillating tip, where

$$|A'_{drive}| = |A| \frac{\Delta E_{CL} + \Delta E_{ts}}{2\pi E} = |A|(\frac{1}{Q} + \frac{\Delta E_{ts}}{2\pi E}) \tag{4.15}$$

It is noted that dispersions (frequency-dependent phase variations) in the oscillator circuit and in the actuator assembly can lead to artifacts in the interpretation of damping data, because $|A_{drive}| = |A|/Q$ only hold for $\varphi = \pi/2$. Mechanical

resonances in the actuator assembly are likely to occur at the high resonance frequencies of conventional cantilever. These resonances can cause sharp vibrations of the phase with frequency and thus create artifacts in the measurement of ΔE_{ts}. Self-oscillation technique for cantilever [134] helps to avoid these resonances. Cleveland *et al.* [135] have introduced a method that yields the correct dissipation energy even for cases where that phase angle between actuator and cantilever is not $\varphi = \pi/2$.

4.2.2 Simple theory of small amplitude, off resonance AC mode Lateral Force Microscopy

In the simple approximation which is illustrated in Figure 3.4. The cantilever is modelled as a mass attached to a spring with a stiffness k_0 , and the displacement x increases with increasing distance from the sample surface. The cantilever is assumed to obey the Hooke's law:

$$F = -k_0 x \tag{4.16}$$

The stiffness k_0 is positive for a lateral spring, in which the restoring force opposes the displacement x. The tip-surface interaction stiffness is modelled as another spring of stiffness k_L , and is equal to $-\frac{dF}{dx}$, where F is the tip-surface force and x is the tip-sample separation. k_L is assumed to be constant over the range of the oscillation amplitude. It is a restriction that makes it necessary to use a small amplitude. By contrast, if a large amplitude is used, cannot be assumed to be constant, and much more complicated models must be used to extract the tip-surface interaction. Damping is ignored, and the oscillation frequency is assumed to be sufficiently low that the cantilever resonance has no effect. in the experiment, as shown in Figure 4.4, A displacement with constant amplitude at a frequency well below the resonance is applied to the base of the cantilever using a piezo (the 'shear piezo'). The tip oscillation amplitude is measured, for the shear oscillation, for the simplified model, the displacement for cantilever in interaction is $A_0 - A_{lat}$ and the displacement of spring like bonding between the tip apex and the sample is A_{lat} , we can then write

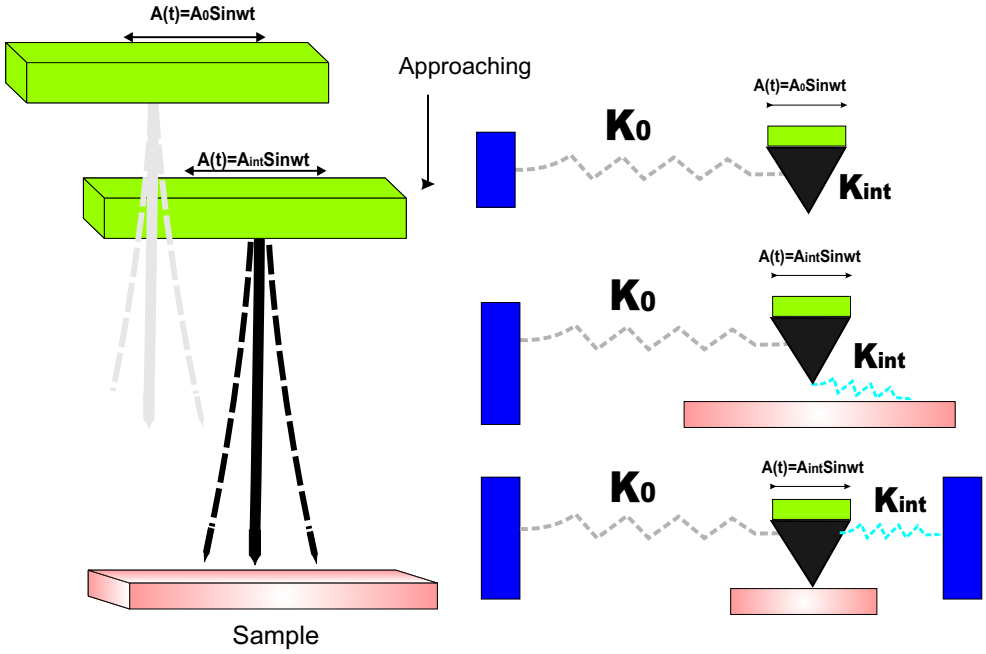

Figure 4.2: Schematic view of lateral tip sample interaction

$$k_0(A_0 - A_{lat})sin(\omega t) = k_L A sin(\omega t) \tag{4.17}$$

Where A_0 is the free oscillation amplitude (i.e. the amplitude at large tip-surface separation, where k_L is zero). It then becomes clear that k_L is given by:

$$k_L = k_0(\frac{A_0}{A_{int}} - 1) \tag{4.18}$$

We therefore see that small amplitude AC mode AFM does not actually measure the force itself, but rather the interaction stiffness.

When the contact stiffness is zero, the measured amplitude is simply equal to the applied amplitude. A negative interaction stiffness k_L gives a increase in interaction oscillation amplitude A_{int}, and a positive k_L gives an decrease in A_{int}.

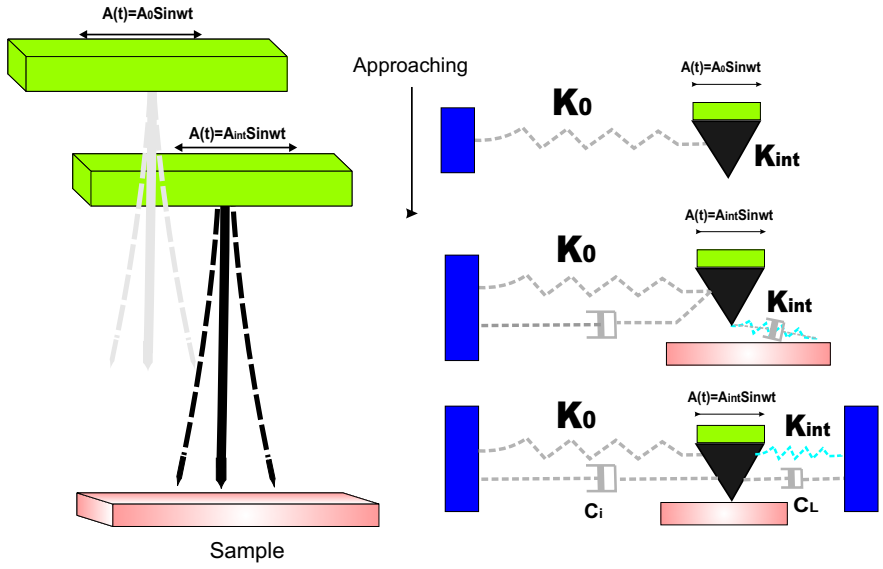

Figure 4.3: the schematic view of tip-sample interaction and considering dampimg effect

4.2.3 Classical dynamic theory of small amplitude, off resonance AC mode Lateral Force Microscopy

In previous section we gained a basic understanding of how small amplitude AFM works, we now turn to a more realistic model. As before, we model the cantilever as a mass on a spring. We assume that the cantilever can be modelled as a harmonic oscillator with a single degree of freedom. This assumption is valid provided that the interaction stiffness is not so high and the dynamic behaviour of the cantilever is not changed. We keep the low frequency constraint and allow for the effects of damping, as shown in Figure 4.5. We consider only the oscillation of a special cantilever parallel to the sample by means of a piezoelectric actuator. As the system is not in equilibrium, we write down the equation of motion:

$$m\frac{dz}{dt} + (C_i + C_L)\frac{dz}{dt} + (k_0 + k_L) = k_0 A_0 sin(\omega t) \tag{4.19}$$

C_i is the intrinsic damping coefficient of the cantilever, including effects due to the internal damping of the cantilever structure. C_L is the damping coefficient

due to the tip-surface interaction, and m is the effective mass of the cantilever . The steady-state solution to Equation 4.19 has the form

$$x = A_{int} sin(\omega t + \phi) \tag{4.20}$$

where A_{int} is the tip oscillation amplitude and ϕ is the phase. Substituting Equation 4.20 into Equation 4.19, we find that A_{int} and ϕ are given by:

$$A_{int} = \frac{k_0 A_0}{[(k_0 + k_L)^2(1 - \frac{\omega^2}{\omega_0^2})^2 + ((C_i + C_L)\omega)^2]^{1/2}} \tag{4.21}$$

$$tan\phi = \frac{(C_i + C_L)\omega}{(k_0 + k_L)(1 - \frac{\omega^2}{\omega_0^2})} \tag{4.22}$$

Equations 4. 21 and 4.22 can then be rearranged to give the following relations for k_L and C_L:

$$k_L = k_0(\frac{A_0 cos\phi}{A_{int}(1 - \frac{\omega^2}{\omega_0^2})} - 1) \tag{4.23}$$

$$C_L = \frac{kA_0(1 - \frac{\omega^2}{\omega_0^2})^2 tan^2\phi}{A_{int}\omega[1 + (1 - \frac{\omega^2}{\omega_0^2})tan^2\phi]^{1/2}} - C_i \tag{4.24}$$

First, we note that Equations 4.23 and 4.24 give the tip-surface contact stiffness and damping coefficient entirely in terms of measurable parameters, ω,A_0,A_{int},ϕ are obviously known, and ω_0 can be found from the geometry of the cantilever or by direct measurement , and C_i can be found from Equation 4.21 by measuring the phase angle at large tip-surface separation, where C_L is zero.

Equation 4.23 reverts to the simple solution (Equation 4.18) under conditions of low frequency (ω) and low damping (C_L) Moreover, we can determine whether these conditions are satisfied in any particular experiment because ω,ω_0, ϕ are measurable parameters. In practice, it is clear that we can safely use the simple approximation (Equation 4.18) when $\omega < 0.1\omega_0$ and $\phi < 5^o$.

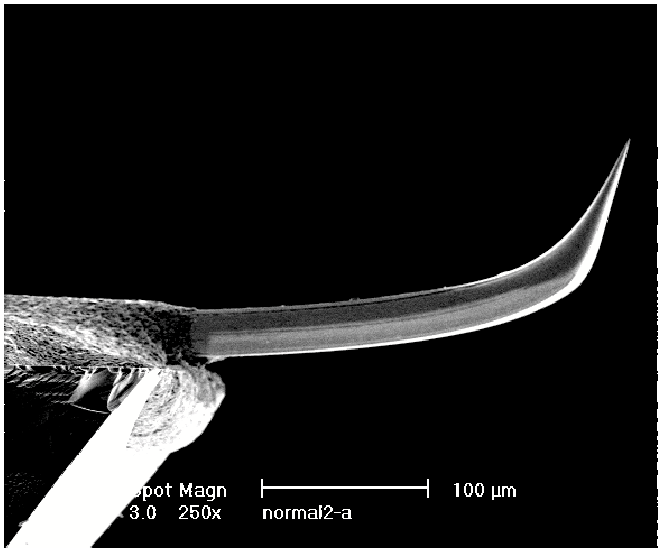

Figure 4.4: SEM picture of a tungsten cantilever to measure lateral force in dynamic mode

4.2.4 Lateral force imaging of Cu-TBPP molecules on Cu(100)

We used combined tunneling and force microscope operating at room temperature in ultra high vacuum UHV at University of Basel . Metalic home made cantilever out of tungsten wire was made and attached carefully attached on a silicone cantilever base block as shown in Fig. 4.6. The deformation of the cantilever is detected via the deflection of a light beam reflected from the back side of the cantilever.

A four quadrant photodiode is employed to detect both bending and torsional deflections. The cantilever are supposed to be very stiff in order to prevent the tip from jumping into contact with the surface due to the strong force gradients likely to develop at tunneling distances. The normal and torsional cantilever stiffness are measured to be between 100- 150 N/m and 3200-3400 N/m respectively. The eigenfrequency f_0 of the fundamental normal and torsional resonance frequency of the cantilevers are typically between 25 kHz to 30 kHz and between 800 kHz and 3 MHz, respectively. The quality factors in UHV were between 10000 and

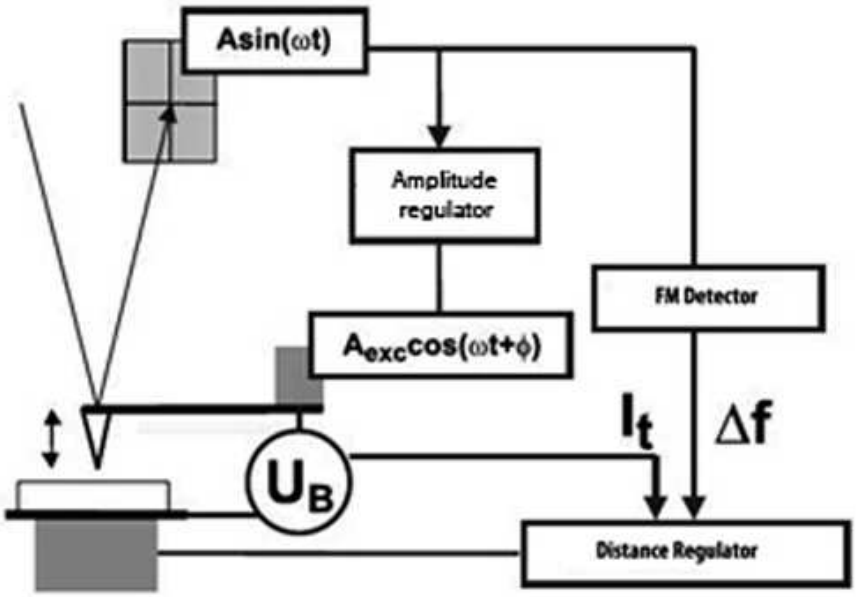

Figure 4.5: Schematic view of AFM set up for torsional mode imaging

30000. The position of the reflected light beam is sensed by a negatively biased low-capacitance photodiode. The currents from the four quadrants are converted to voltages by fast operation amplifiers which are positioned a few millimeters from the photodiode in the UHV.

To circumvent heating problems in vacuum, the amplifiers are operated at low voltage. The photodiode and the current-to-voltage converter are mounted on a UHV compatible sapphire circuit board. Directly outside the vacuum chamber the voltage signal is again amplified to compensate the capacitive load of the output cable.

Actual eigenfrequencies of the cantilever oscillations up to 3MHz are detected by a digital phase-locked loop with a resolution of 10 mHz. A sinusoidal signal with the same frequency is used to excite the torsional oscillation by means of a piezoactuator. The actuator mainly shakes the cantilever holder in the normal direction, however the high quality factor and the tuning to the actual eigenfrequency the torsional oscillation can also be excited effectively . The amplitude of excitation is controlled to maintain a constant level. The (100) surface of a

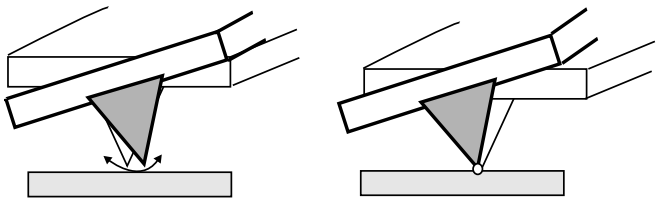

Figure 4.6: Schematic view of torsional mode of cantilever oscillation a) Free oscillation parallel to the surface b) Torsional oscillation with tip-sample contact

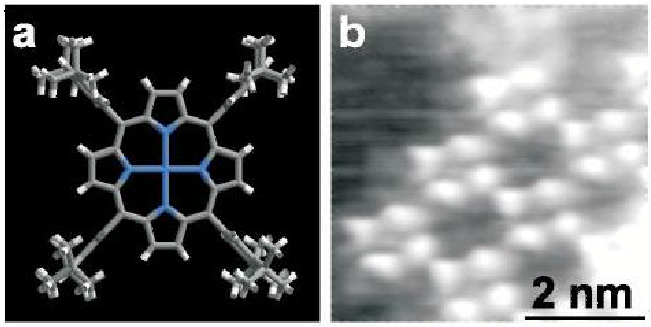

Figure 4.7: a)Chemical structure of di-teriary-butyl-phenyl prophyrin molecule (Cu-TBPP) and b) STM topography image of Cu-TBPP molecule Adopted from [136]

Cu single crystal has been cleaned by repeated cycle of argon ion sputtering and annealing. Pressure did not exceed 5×10^{-7} mbar during annealing at 450 °C for 30 minutes in each cycle. After this preparation, the surface exhibits atomically flat terraces of typically 100 nm wide, separated by monoatomic steps. Then, approximately 0.2 monolayer of Cu-tetra-3,5 di-tertiarybutylphenyl porphyrin (Cu-TBPP) molecules were sublimated onto an atomically clean Cu(100) surface. Figure 4.8. shows the chemical structure of (Cu-TBPP) molecule and its STM topography image. The evaporation rate and thickness was monitored by using a quartz crystal thickness monitoring system.

We imaged the Cu-tetra-3,5 di-tertiarybutylphenyl porphyrin (Cu-TBPP) molecules on Cu(100) in normal and torsional modes, to measure the lateral

and normal forces gradient in dynamic mode using tungsten cantilever, and attempted to manipulate (Cu-TBPP) molecules on Cu(111). Tunneling current I_t feedback was used for the distance regulation. As the cantilever is vibrating I_t is recorded during only a small fraction of the oscillation cycle when the tip is in tunneling proximity to the surface. Consequently the mean tunneling current I_{t-mean} was used as a feedback signal. Figure 4.9 shows the topography, Δf and damping signals. The cantilever is dithered in normal oscillation mode at the resonance frequency of f_0=27.834 kHz, and amplitude oscillation of about $A_0 = 5nm$, and the the bias voltage of V_{bias}= 1.06 V is applied and tunnel current is set to be $I_t = 0.5nA$. In topography and damping images monoatomic step is resolved and the (Cu-TBPP) molecule wires features at the lower terrace are imaged, however, Δf channel does not show any contrast. In Figure 4.10 a large scan area over molecule deposited sample of Cu(100) is imaged. In this measurement the cantilever is dithered in normal mode with respect to the sample, the sample surface feature steps and terraces is resolved in topography, Δf and damping channels. Low coverage of Cu-TBPP molecule deposition could be also imaged, while the tip-sample distance is regulated by keeping the mean tunnel current constant. Bias voltage set to V_{bias}= 1 V. The scan speed is set to 40 nm/s and the scan area is 250×250 nm. In Figure 4.10 the image area is specifically zoomed over the(Cu-TBPP) molecules deposited over a wide terrace without any changes in scan parameter. The topography and Δf channels show good contrast of molecules images. The image size is set to be 50×50 nm. We increased the dither frequency of the cantilever to excite the torsional mode of the cantilever. The bias voltage is set to V_{bias}= 0.6 V and vibration amplitude is measured to be between 2 to 4 nm, the topography, Δf and damping channels are imaged as shown in Figure 4.11. In all channels the step features and wide terrace regions are imaged. In Δf and damping signals the molecules at the lower terrace and the step edges are also resolved, however the molecules images in topography channel are not clear. A comparison between images obtained by normal mode oscillating cantilever and torsional one, shows that the step edge features and molecule sites at Δf and damping channel images are distorted. Which might be caused due to the large amplitude oscillation in torsional mode vibration. We increased the amplitude of the torsional oscillation to a value between 6 to 10 nm

and keeping all the other scan parameters such as V_{bias}, scan speed and set tunnel current constant. As shown in Figure 4.12 we observed no changes in topography image but images of Δf and damping signals show wider steps and scattered pattern at the molecules sites, which might be due to mechanical excitation of the molecules by induced energy of the oscillating cantilever while intermittent contact of the tip apex to the sample surface. Figure 4.14 shows the effects of large amplitude oscillation of the cantilever at the step edge. In topography channel no change in step edge imaging is observed. Because the control electronics uses the mean value of the current. However, the wider feature of steps edges at Δf and damping signals are resolved. These measurement implies that large amplitudes required by FM-AFM are prohibited for lateral force microscopy, because the molecular and atomic resolution is not achievable with cantilevers oscillating over a few nanometers parallel to a surface.

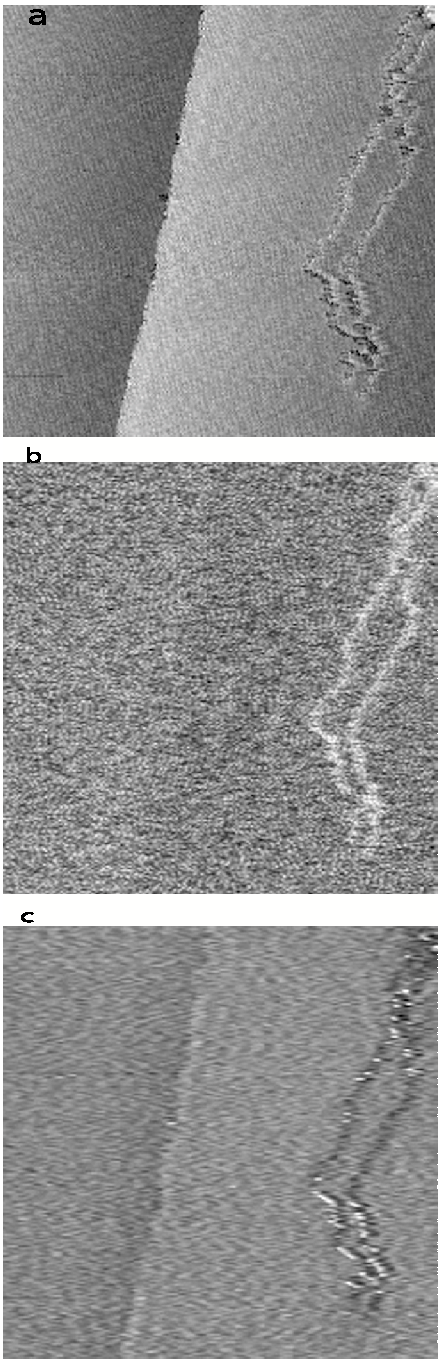

Figure 4.8: Cu-TBPP molecule on Cu(100) surface image obtained in normal mode oscillation a) Topography b) Δf signal c) damping, image size: 90×90 nm, normal oscillation resonance frequency=f_0=27.834 kHz, and amplitude oscillation of about $A_0 = 5nm$, and the the bias voltage of V_{bias}= 1.06 V is applied and tunnel current set to be $I_t = 0.5nA$.

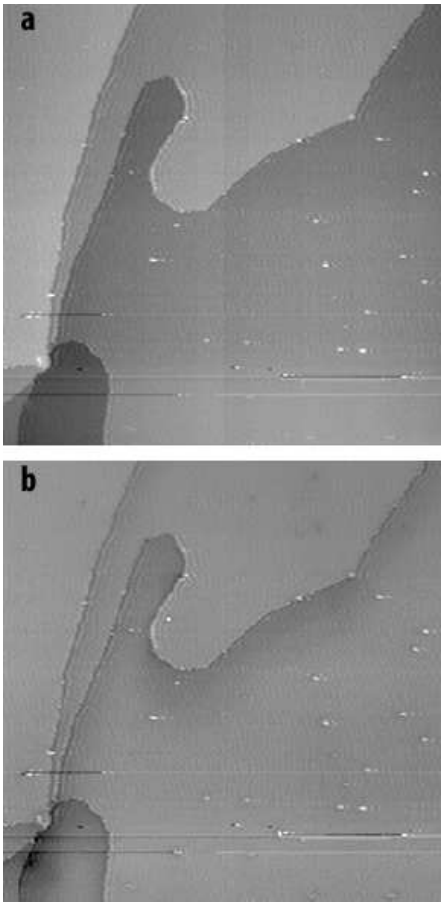

Figure 4.9: Cu-TBPP molecule on Cu(100)surface image obtained in normal oscillation mode a)Topography b)Δf signal, image size: 250×250 nm, Resonance frequency: 27.834 KHz, V_{bias} = 1.0 V, I_t = 0.5 nA, Free oscillation Amplitude:∼ 5 nm

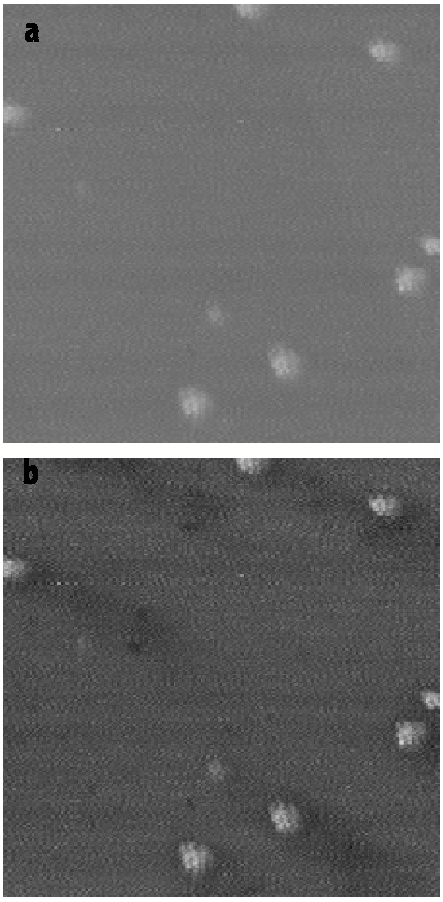

Figure 4.10: Cu-TBPP molecule on Cu(100)surface image obtained in normal oscillation mode a)Topography b)Δf signal, image size: 50×50 nm, Resonance frequency: 27.834 KHz, V_{bias} = 1.0 V, I_t = 0.5 nA, Free oscillation Amplitude:∼ 5 nm

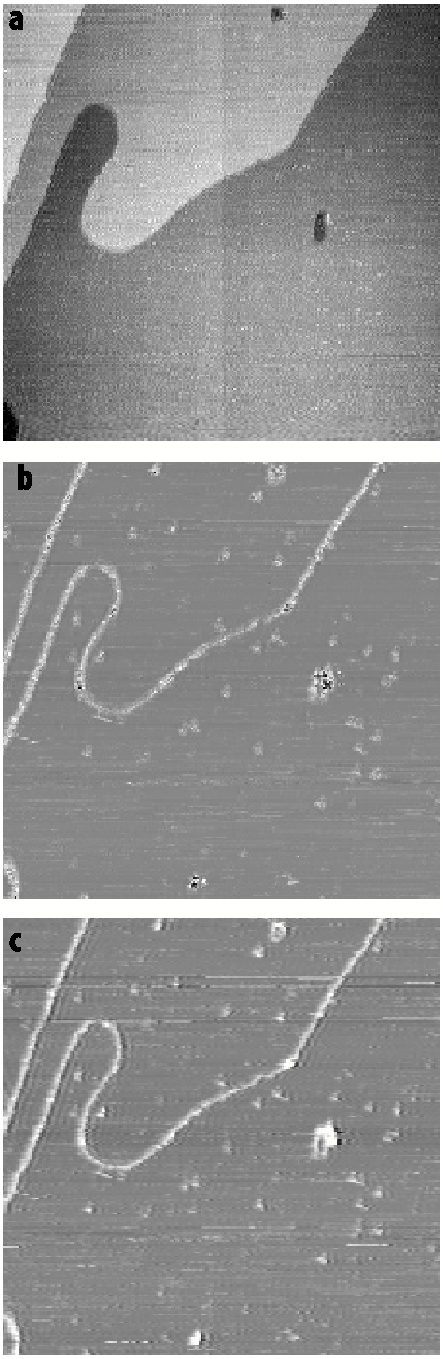

Figure 4.11: Cu-TBPP molecule on Cu(100)surface image obtained in torsional oscillation mode a)Topography b)Δf signal c) damping, image size: 250×250 nm, Resonance frequency: between 1.7 MHz-2.5 MHz $V_{bias} = 0.6$ V, $I_t = 0.5$ nA Free oscillation Amplitude: between 2-4 nm.

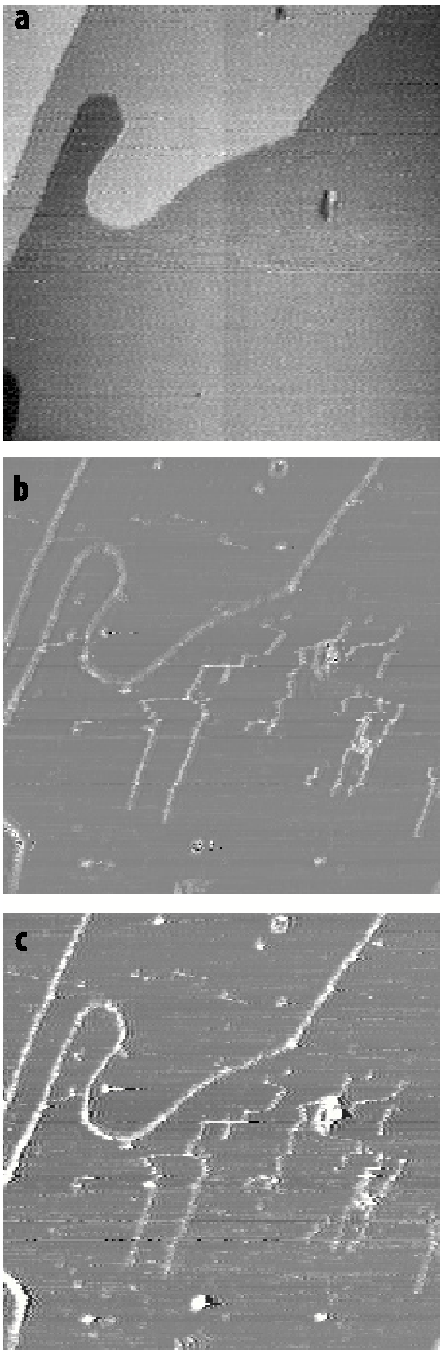

Figure 4.12: Cu-TBPP molecule on Cu(100)surface image obtained in torsional oscillation mode a)Topography b)Δf signal c) damping, image size: 250×250 nm, Resonance frequency: between 1.7 MHz-2.5 MHz, $V_{bias} = 0.6$ V, $I_t = 0.5$ nA Free oscillation Amplitude: between 8-10 nm.

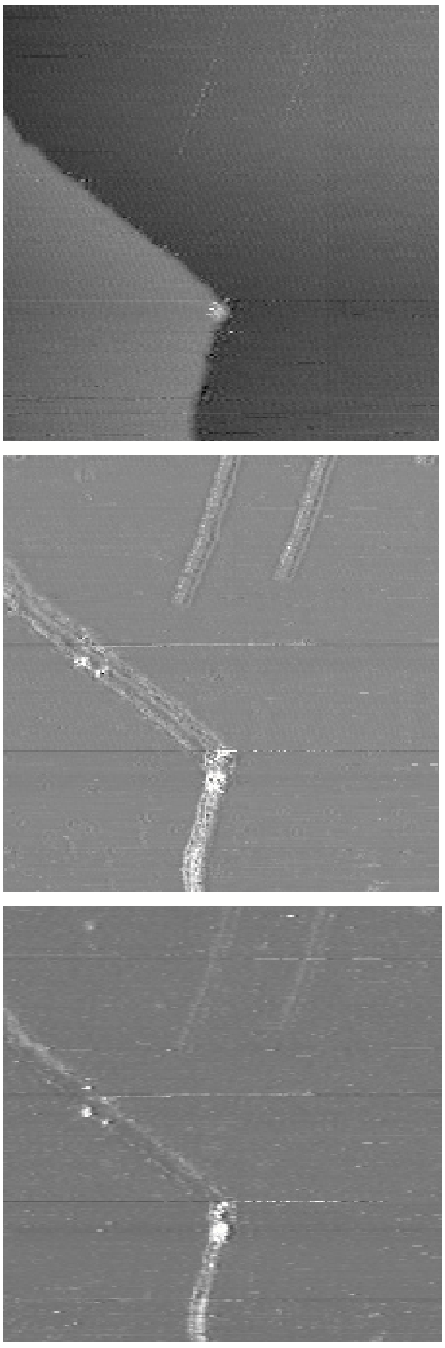

Figure 4.13: Cu-TBPP molecule on Cu(100)surface image obtained in torsional oscillation mode a)Topography b)Δf signal c) damping, image size: 250×250 nm,Resonance frequency: between 1.7 MHz-2.5 MHz, V_{bias} = 0.6 V, I_t = 0.5 nA Free oscillation Amplitude: between 8-10nm

4.2.5 Small amplitude, off resonance lateral force nc-AFM imaging

In this section, we are going to describe the experiments performed using our home made lateral force ncAFM that we built at Bilkent University.

The Microscope is first run as STM in air and vacuum, to check the accuracy of basic components of the microscope, specially, tube scanner piezo of the microscope , on the well known HOPG sample surface and atomic resolution was achieved as shown in figure 4.1. The hexagonal unit cell is imaged. Note that The hexagonal unit cell of graphite has two atoms in its basis, but STM shows only one of the two, forming a trigonal lattice.

Si(111) samples were cut from 525 μm thick, P-doped, n-type wafers with 1-10 Ωcm resistivity oriented to within 0.5 $^\circ$ of (111) plane. Both *exsitu* and *insitu* processes are applied to clean the samples. The sample was cleaned with propanol in ultrasonic bath and rinsed with overflowing deionized water. Samples are dried with blowing dry nitrogen gas before transferring into the load-lock chamber. The sample is then transferred to the UHV system and degassed by e-beam heating at $\sim$ 600 °C for about 10 hours. The pressure is kept in the 10^{-10} mbar range during degassing. Then the sample is flashed to $\sim$ 900 °C for 2 minutes followed by a sudden increase to about 1050 °C. After waiting again for 2 minutes at this value the temperature is set to $\sim$ 900 °C for a minute. Finally the sample is slowly cooled down in a few minutes.

The cleaned sample is left on the sample manipulator for about 15 minutes, and then transferred to the sample carousel in order to cool down. The sample temperature drops to the microscope temperature in about 1.5 hours. Then the sample is transferred to the slider and it is ready for STM/AFM analysis.

Si(111) samples stays almost clean for about 3-4 days at a chamber pressure of about 1×10^{-10} mbar. Once the sample is loaded to the microscope, the fiber has to be aligned with respect to the back of the cantilever to achieve the maximum interferometer sensitivity. A CCD camera with a zoom lens is used to monitor

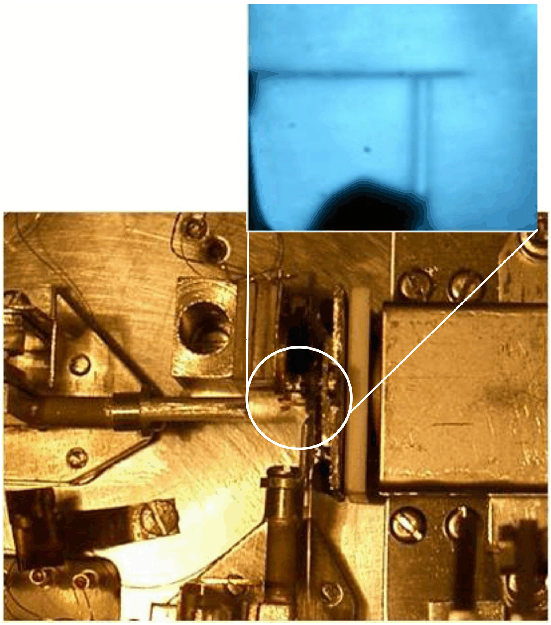

Figure 4.14: The view of fiber alignment at the side of cantilever

the fiber during coarse positioning of the fiber at the side of the lever with fiber slider, as shown in Figure 4.15.

During fiber slider operation a triangular voltage is applied continuously to the fiber tube piezo, so that it moves back and forth giving rise to an interference signal which can be monitored with an oscilloscope and recorded by the software. We maximize the sensitivity by searching for the best point on the lever and best angle of the fiber with respect to the lever. As explained earlier, the software allows to measure interference patterns and calculates the visibility, slope and the overall sensitivity of the interferometer after every step. Once the user is satisfied with the obtained sensitivity the software can be set to keep the fiber at the quadrature point of the interference where the sensitivity is maximum. Except for decreases due to the reduction of the laser power by time, the sensitivity usually stays constant throughout an experiment. The CCD camera is used to monitor the cantilever and sample during coarse approach of the sample towards the tip controlled via the joystick. After tunneling current is obtained, initial checks on whether the tip is good or not are made by monitoring the tunneling current or

taking short scans and i-v curves. Tip treatment procedures described earlier are applied, if necessary. It is quite possible that a blunt tip gets sharp during a scan or vice versa. Hence we do not insist on guaranteeing the quality of the tip at the very early stages of operation. On the other hand, the interferometer needs some time to be stabilized. For example the laser power drops quite rapidly in the first few hours because of the heating of the diode laser. The choice of the appropriate frequency is a crucial step while setting up the interferometer. The accumulation of all these problems usually prevents us to get good results in the first day after cleaning the sample. Very low pressures in the vacuum system is therefore essential to have long operating time. Since a clean sample begins to be contaminated by the residual gases in the UHV chamber after a few days depending on the system pressure, it must be recleaned for longer experiments. Although we know from experience that the number of defects increases as the number of cleaning cycles increases, sometimes the samples were recleaned for further investigation to save time.

During the scans we usually record signals through three channels simultaneously. The first channel is the tunnel current, which is used as the feedback parameter. The second channel is the oscillation amplitude of the lever measured through the lock-in amplifier, which is related to the force gradient. Third channel is the voltage applied to regulate the sample scanner, V_z, which is actually the STM topography of the surface. We sometimes record the phase of the lever oscillation.

In the first series of experiments, we tried to see how oscillating STM tip parallel to the sample would effect on image quality. The image was obtained about 3 days after the sample was cleaned. Fig 4.16 show STM topography of the Si(111) surface and its cross section. The adatoms could be resolved. The free oscillation vibration set to 0.8 $Å_p$, The image size is 70×30 Å and the scan speed set to 100 Å/s. Tip bias voltage and set tunnel current were -1.8 V and 0.4 nA, respectively.

In second series of experiments, as shown in Fig. 4-17, we performed our measurement on HOPG sample using tungsten cantilever. The images were obtained

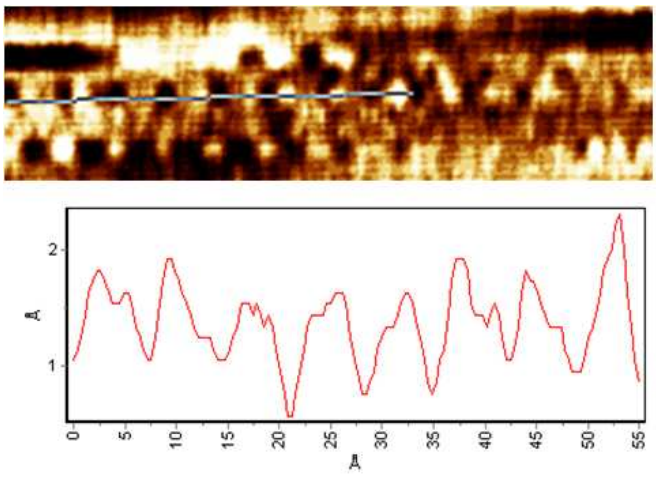

Figure 4.15: Atomic resolution of STM topography with dithering cantilever. The free oscillation vibration set to 0.8 $Å_p$, The image size: 70×30 Å and the scan speed set to 100 Å/s. Tip bias voltage and set tunnel current were -1.8 V and 0.4 nA, respectively.

with cantilever with the stiffness of $\sim$ 215 N/m with an oscillating amplitude of 0.4 $Å_p$, while the tunnel current maintained the feedback. The oscillating frequency set to 8.092 kHz while the resonance frequency of the cantilever was 47.065 kHz. The image size is 1200×1000 $Å^2$ and the scan speed set to 50 Å/s. Tip bias voltage and set tunnel current were -0.2 V and 0.4 nA, respectively.

In the other set of experiments, we imaged a clean Si(111) using lateral cantilever. The stiffness of cantilever is calculated using Equation 2.17 and it is found to be 75±10 N/m. The lever was oscillated parallel to the surface with an oscillation frequency of 7.56 kHz. The cantilever resonance frequency was 18.049 kHz. The cantilever is oscillated far below its resonance frequency with an oscillation amplitude of 0.4 $Å_p$. The tunnel current is used for feedback to control tip-sample distance. The scan speed set to 40 Å/s and the tip bias voltage and set tunnel current were -1 V and 0.4 nA, respectively. The single atom and double steps on Si(111) are resolved in both topography shown in Fig. 4.20, as well as lateral stiffness force gradient channel, We found that at the single step we observed 0.1 N/m contrast compared to 0.5 N/m at the double step. These values are smaller than the normal force contrast by an order of magnitude. Our experiments reveals

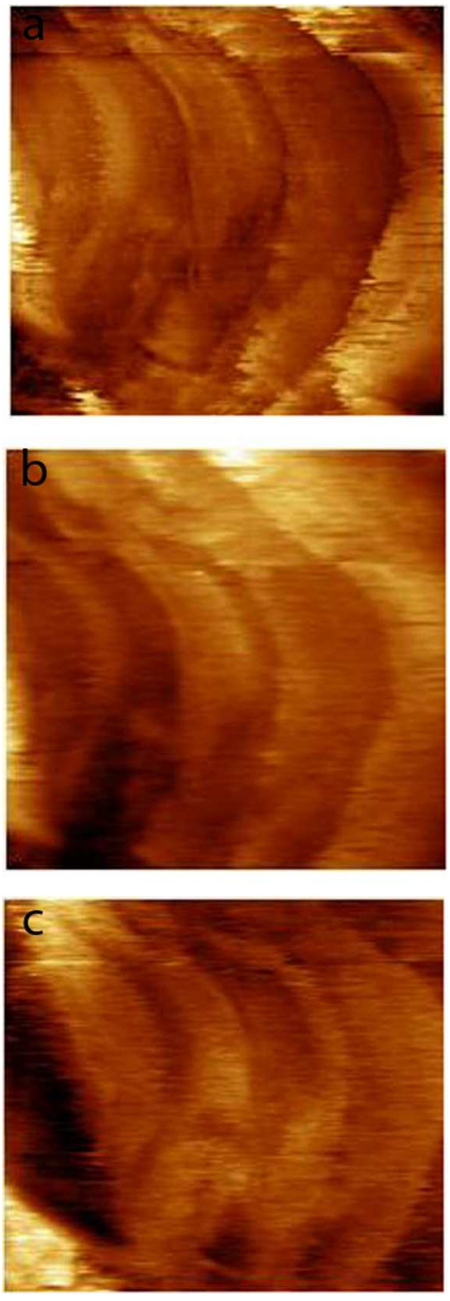

Figure 4.16: Imaging of HOPG steps a) Topography, b) Lateral stiffness, c) Phase. Oscillating amplitude of 0.4 $Å_p$, The image size is 1200×1000 $Å^2$ and the scan speed set to 50 Å/s. Tip bias voltage and set tunnel current were -0.2 V and 0.4 nA, respectively.

the first direct measurement of lateral force gradient in dynamic mode.

We have also performed lateral force-distance spectroscopy. As the feedback loop is frozen, the sample is first retracted back by a specified distance and re-approached toward the tip, while recording the force gradient as well as the tunnel current. A threshold current level is used to stop and retract the sample. The lever stiffness calculated to have stiffness of 50± 10 N/m and oscillation amplitude was 0.4 Å_p.

In the first measurement as shown in Figure 4.21, the force gradient starts much earlier than tunnel current occurs and the tunneling barrier hight is calculated to be ϕ_A= 0.4 eV. This extremely small value indicates that the tip or sample has some contamination and to increase current, tip has to be indented in to the surface quit hard. In another experiment, which is given in Figure 4.22, the tunnel current starts before lateral force as expected. spectroscopy exhibits a sudden change in force gradient , while the tunneling current increasing smoothly in the course of approaching sample to the oscillating cantilever. The maximum attractive force is measured to be 46 N/m. The barrier hight calculated to be ϕ_A=4.1 eV, which implies that tip and sample are clean. It should be noted that for both experiments we used the same cantilever but different sites of the sample and bias voltage for both measurement was set on -1 V. It seems that there are very significant lateral forces acting on tip during typical experiments. The lateral force gradient at 1 nA tunnel current is somewhere between 15-40 N/m as can be seen in Fig. 4.22.

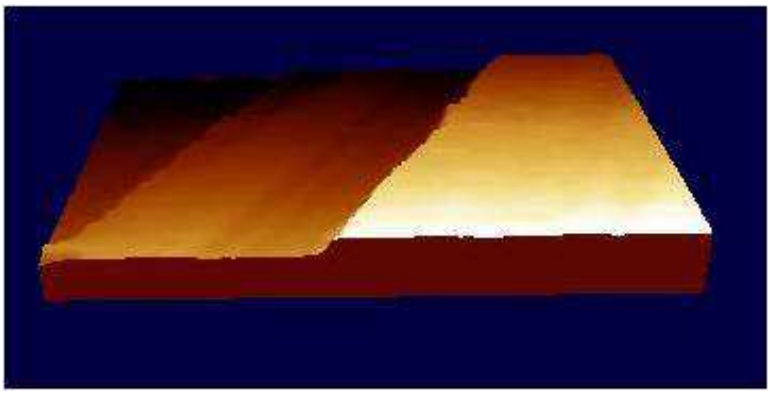

Figure 4.17: 3 Dimension image of STM topography of Si(111), showing single and double steps. Image size: 690×380 Å^2.

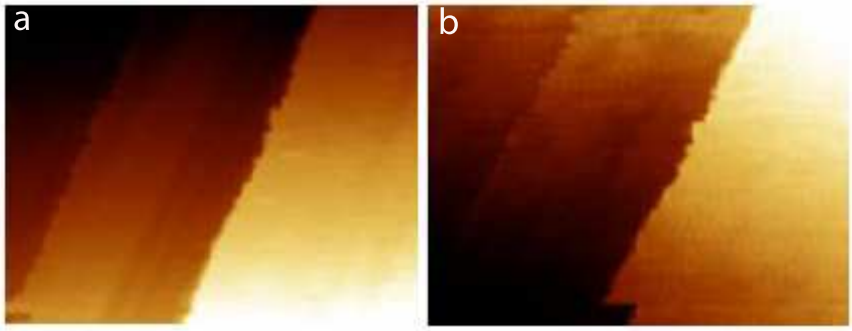

Figure 4.18: Simultaneous imaging of Si(111) a) Topography image b) Lateral force gradient image. Image size: 690×380 Å^2,. The lever was oscillated parallel to the surface with an oscillation frequency of 7.56 kHz, with an oscillation amplitude of 0.4 Å$_p$. Tip bias voltage and set tunnel current were -1 V and 0.4 nA, respectively.

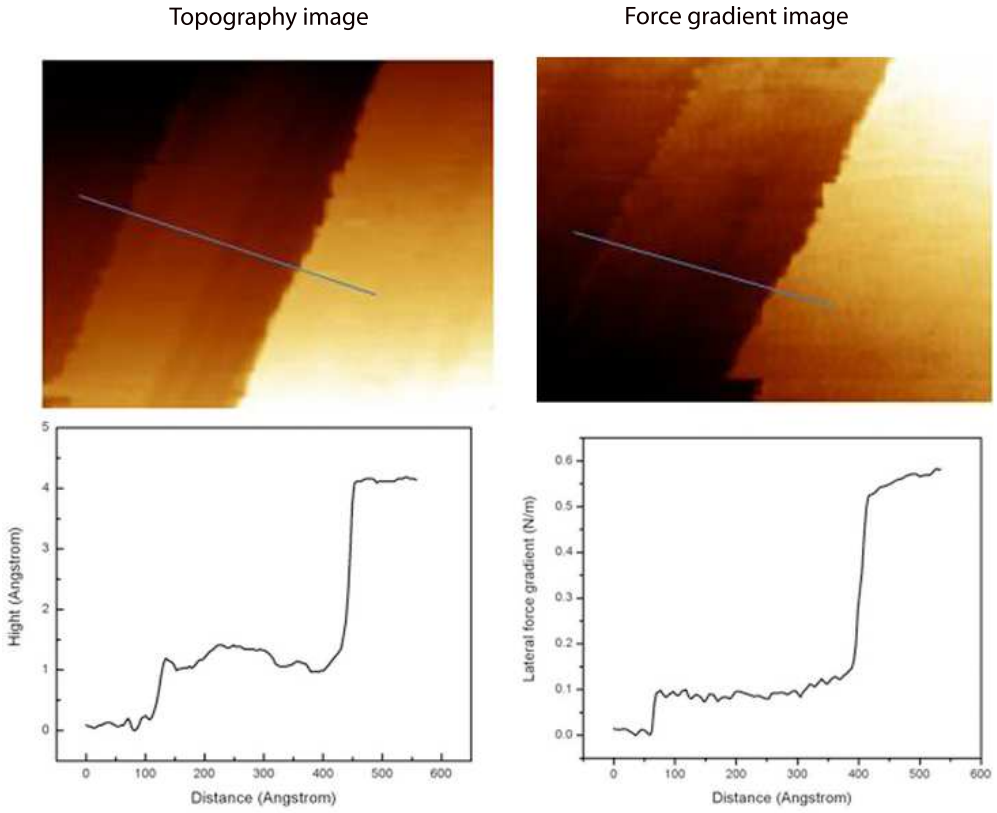

Figure 4.19: a)Lateral Force gradient image, b)Lateral force gradient vs. distance.

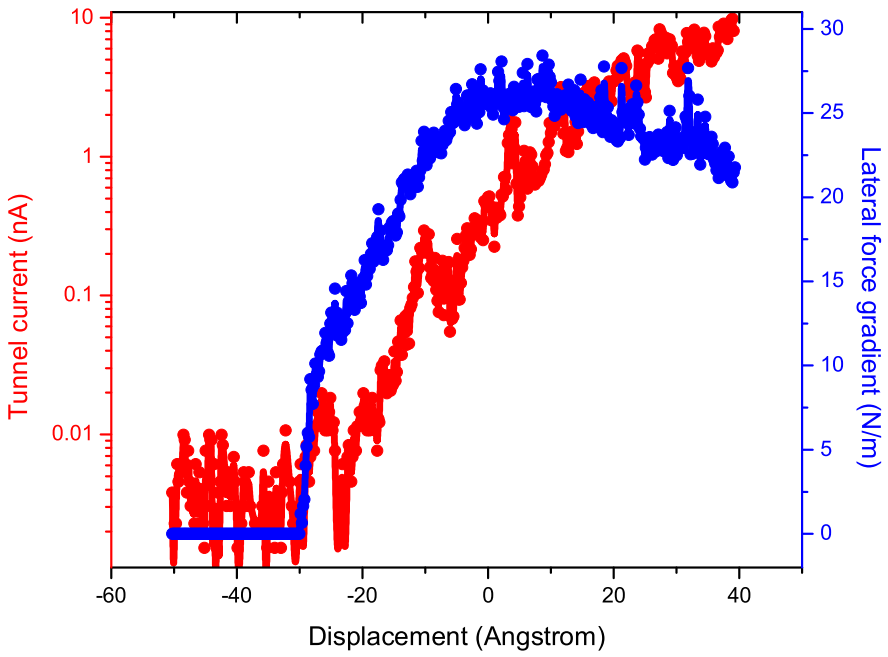

Figure 4.20: Lateral force gradient-distance spectroscopy.The sample bias voltage was set on -1 V. The cantilever free oscillation amplitude 0.4 Å_p .

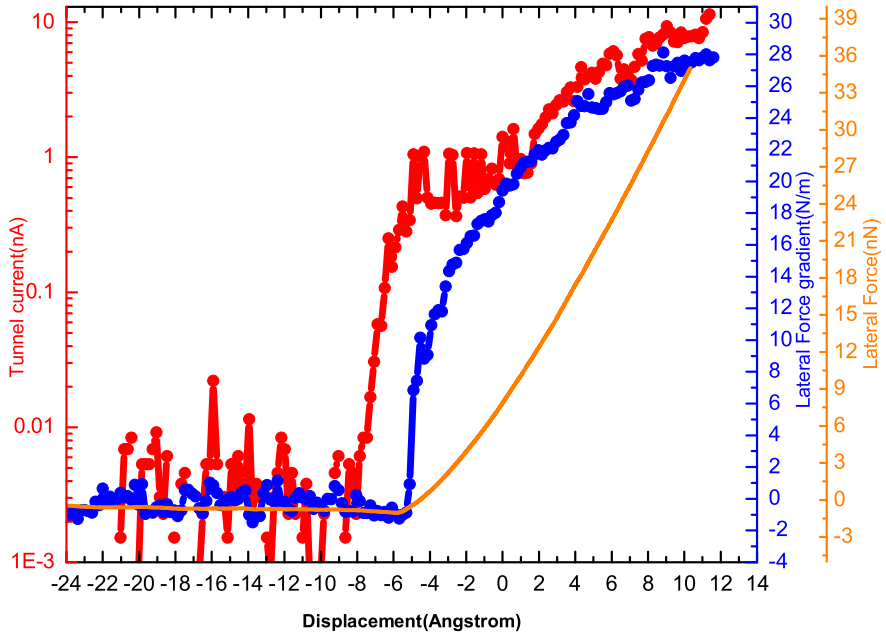

Figure 4.21: Lateral force gradient, force -distance spectroscopy. The sample bias voltage was set on -1 V. The cantilever free oscillation amplitude 0.4 $Å_p$.

Chapter 5

Conclusions

In this Ph.D. work, we constructed a novel fiber optic interferometer based lateral nc-AFM/ STM and used to investigate Si(111)-(7×7) surface. The interferometer has been built in such a way that its sensitivity surpasses that of the earlier versions. The improvement in the resolution of the interferometer allowed us to use very small oscillation amplitudes to oscillate the cantilever parallel to the surface, which overcomes the problems associated with the large amplitude technique that has been widely used. Since we use small amplitude, by measuring directly the changes in the oscillation amplitude rather than the frequency shift, we can extract lateral forces with unprecedented sensitivity.

We can directly extract the force gradient with out any complication. It is simple to quantify the AFM data. We have observed single and double atomic steps in topography and lateral the lateral stiffness. These information allowed us to measure the lateral force direct and quantitatively. The lateral stiffness contrast has been observed to be 0.1 N/m at single step in contrast to 0.5 N/m at double step on Si(111) surface.

We have also carried out lateral force-distance spectroscopy experiments, in which we simultaneously measured the force gradient, and tunneling current as the sample is approached towards the tip and retracted back. We obtained $f - d$

curves exhibiting sharp change of the force gradient while the sample is approaching to the surface. It seems this behavior is related to the nature of laterally vibrated cantilever and sample interaction rater that just the quality of the tip although the tip quality should be considered as an important parameter, we observed only positive force gradients similar to related work reported by Ernst Meyer and H. Kawakatsu groups. The lack of attractive region in the lateral force gradient could be due to cancellation of long range attractive forces, acting on the tip because of the symmetry. We observed for the first time, surprisingly large, 15-40 N/m, lateral stiffness in typical STM operating currents at 1 nA.

The microscope can be improved further to measure the lateral and normal force gradient simultaneously. This will allow us to quantify the friction forces directly from imaging the surface, at different normal loads. Our method could be also employed in liquid environment.

Moreover challenges toward measurements of forces involved in atomic and molecular scale manipulation are still open. These forces and energy scales can be measured by this novel microscope. possible methods to investigate lateral forces in dynamic mode are examined by running a dynamic force microscopy in torsional mode. in one series of experiments we employed frequency modulation lateral force microscopy in torsional mode which is also known as dynamic force microscopy. This series of experiments are performed at University of Basel, Switzerland. We imaged the (Cu-TBPP) molecule on Cu(100) surface in normal and torsional mode using a home made tungsten cantilever. our experiments show the capability of manipulating molecules on surface using a vibrating cantilever. In our technique , the tunnel current is used to regulate tip sample distance, cantilever is oscillated in its torsional mode parallel to the surface at its torsional resonance frequency. The cantilever oscillation up to 3 MHz are detected by a digital phase-locked loop with a resolution of 10mHz. This method is capable to image a sample in lateral force mode and even manipulate the molecules on a specific surface. However the forces involved in these processes are not quantitatively obtainable. To achieve these goals, we followed extensive experiments which started by constructing our home made microscope.

Lateral forces in dynamic mode are examined by running a dynamic force microscopy in torsional mode at University of Basel. We imaged the Cu-TBPP molecules on Cu(100) surface in normal and torsional mode using a home made tungsten cantilever. Our experiments show the capability of manipulating molecules on surface using a vibrating cantilever. In these experiments, the tunnel current is used to regulate tip sample distance, cantilever is oscillated in its torsional mode parallel to the surface at its torsional resonance frequency. The cantilever oscillations up to 3 MHz are detected by a digital phase-locked loop with a resolution of 10mHz. This method is capable to image a sample in lateral force mode and even manipulate the molecules on a specific surface. However the forces involved in these processes were not quantitatively obtainable, in contrast to sub-Ångstrom oscillation amplitude AFM that we have developed.

Bibliography

[1] G. Binnig, H. Rohrer, Ch. Gerber, and E. Weibel,"Tunneling Through a Controllable Vacuum Gap", Appl. Phys. Lett., **40**, 178, (1982).

[2] G. Binnig, H. Rohrer,"Scanning Tunneling Microscopy", Helvetica Physica Acta, **55**,726 (1982).

[3] G. Binnig, C. F. Quate, Ch. Gerber, "Atomic Force Microscope", Phys. Rev. Lett., **56**, 930, (1986).

[4] G. Binnig, Ch. Gerber, E.Stoll, T. R. Albrecht, C. F. Quate, " Atomic resolution with atomic force microscope", Europhysics. Lett., **3**, 1281-1286, (1987).

[5] J. Krim, D. H. Solina, and R. Chiarello, "Nanotribology of Kr monolayer: A quarz-crystal microbalance study of atomic scale friction", Phys. Rev. Lett.,**66**, 181 (1991).

[6] E. S. Snow, P. M. Campbell, " AFM fabrication of sub-10 nanometer metal oxide devices with in situ control of electrical properties", Science, **270**, 1639, (1995).

[7] J. Tersoff, D. R.Hamann, " Theory and application for Scanning tunneling microscope", Phys. Rev. Lett., **50**, 1998, (1983).

[8] J. Tersoff and D. R. Hamann,"Theory of Scannig Tunneling Microscope," Phys. Rev. B, **31**:805, (1985).

[9] C. J. Chen, "Attractive interatomic force as a tunnelling phenomenon", J. Phys.: Condens. Matter, **3**, 1227, (1991).

[10] F. F. Abraham, I. P. Batra. ,"Theoritical interpretation of atomic force microscope images of graphite", Surf. Sci., **209**, L125, (1989).

[11] R. G. Miller, P. J. Bryant, " Atomic force microscopy of layared compoyndes", J. Vac. Sci. Technol. A, **7**, 4, 2879, (1989).

[12] T. R. Albrecht, P. Grtter, D. Horne, D. Rugar., "Frequency modulation detection using high-Q cantilever for enhanced force microscope sensitivity", J. Appl. Phys., **69**, 668, (1991).

[13] F. J. Giessibl,"Atomic resolution of the Silicon (111)-(7×7) surface by atomic force microscopy," Science **267**, 69 (1995).

[14] C. M. Mate,G. M. Mcclleland, R. erlandsson, S. Chiang . ," Atomic scale friction of a tungsten tip on a graphite surface", Phys. Rev. Lett., **59**, 1942 (1987).

[15] R. Perez, M. C. Payne, I. Stich, K. Terakura, "Contrast mechanism in non-contact AFM on reactive surfaces", Appl. Surf. Sci., **123**, 249, (1998).

[16] R. Perez, I. Stich, M. C. Payne, K. Terakura," Surface-tip interaction in noncontact atomic force microscopy on reactive surface," Phys. Rev. B,**58**, 16, 10835, (1998).

[17] D. M. Eigler, E. K. Schweizer, "Positioning single atoms with scanning tunneling microscope", Nature,**344**, 524 (1990).

[18] T. W. Fishlock, A. Oral, R. G. Egdell, J. B. Pethica,"Manipulation of atoms across a surface at room temprature," Nature, **404**, 743 (2000).

[19] M. F. Crommie, C. P. Lutz, D. M. Eigler, "Confinement of electrons to quantum correls on a metal surface", Science, **262**, 218, (1993).

[20] J. R. Oppenhimer, "Three Notes on the Quantum Theory of Aperiodic Effects", Phys. Rev. B., **31**, 66, (1928).

[21] L. Esaki,"New Phenomenon in Narrow Germanium p-n Junctions", Phys. Rev., **109**, 603, (1958).

[22] I. Giaver,"Energy Gap in Superconductors Measured by Electron Tunneling", Phys. Rev. Lett., **5**, 157, (1960).

[23] B. D. Josephson, "Possible New Effects in Supreconductive Tunneling", Phys. Lett., **1**, 251, (1962).

[24] R. Young, J. Ward and F. Scire, "The Topographiner: An Instrument For Measuring Surface Microtopography", Rev. of Sci. Instrum.,**43**, 999,(1972).

[25] E. C. Teague, "Room Temperature Gold-Vacuum-Gold Tunneling Experiments", Bulletin of American Physical Society, **23**, 290, (1978).

[26] U. Poppe, "Tunneling Experiments on a Single Crystal of ERh_4B_4", Physica B & C,**108**, 805, (1981).

[27] J. Bardeen, "Tunneling From Many Particle Point of View", Phys. Rev. Lett., **6**, 57, (1961).

[28] A. Erkan Tekman, M. S. Thesis, Bilkent University, (1987).

[29] J. Winterlin, J. Wiechers, H. Brune, T. Gritsch, H. Hoeffer, R. J. Behm. Phys. Rev. Lett.," Atomic-resolution imaging of closed-packed metal surface by scanning tunneling microscopy", **62**, 59, (1989).

[30] S. Ciraci, A. Baratoff and I. P. Batra, "Tip-Sample Interaction Effects in Scanning Tunneling and Atomic Force Microscopy", Phys. Rev. B, **40**, 2763, (1989).

[31] K. Cho and J. D. Joannopoulos, "Tip-Surface Interactions in Scanning Tunneling Microscopy", Phys. Rev. Lett., **71**, 1387, (1993).

[32] N. D. Lang, "Spectroscopy of single atoms in the scanning tunneling microscope", Phys. Rev. B, **34**, 5947, (1986).

[33] C. B. Duke, p. 1 in *Tunneling in Solids*, Suppl. 10 of *Solid State Physics*, Academic Press, New York, 1969, and references there in.

[34] A. Selloni, P. Carnevali, E. Tosatti, and C. D. Chen, "Voltage-Dependent Scanning Tunneling Microscopy of a Crystal Surface: Graphite", Phys. Rev. B, **31**, 2602, (1985).

[35] J. A. Stroscio, R. M. Feenstra and A. P. Fein,"Electronic structure of the Si(111)2×1 surface by scanning tunneling microscopy", Phys. Rev. Lett., **57**, 2579, (1986).

[36] R. J. Hamers, R. M. Tromp and J. E. Demuth, "Surface Electronic Structure of Si(111)(7×7) Resolved in Real Space", Phys. Rev. Lett., **56**, 1972, (1986).

[37] D. W. Pohl, W. Denk and M. Lanz, "Optical Spectroscopy: Image Recording with Resolution $\lambda/20$", Applied Physics Letters, **44**, 651, (1984).

[38] D. Courjon, K. Sarayeddine and M. Spajer, "Scanning Tunneling Optical Microscopy", Optics Communications, **71**, 23, (1989).

[39] W. J. Kaiser and L. D. Bell, "Direct Investigation of Subsurface Interface Electronic Structure by Ballistic Electron Emission Microscopy", Physical Review Letters, **60**:1406, (1988).

[40] R. Erlandsson, G. M. McClelland, C. M. Mate, "Atomic force microscopy using optical interferometry", S. Chiang, J. Vac. Sci. Technol. A **6**: 266, (1988).

[41] A.Oral, R. A.Grimble, H. Ö. Özer, P. M. haffmann and J. B. Pethica, "Quantitative atom-resolved force gradient imaging using noncontact atomic force microscopy", Appl. Phys. Lett.,**79**, 1915, (2001).

[42] G. Meyer and N. M. Amer, "Novel optical approach to atomic force microscopy", Appl. Phys. Lett. **53**, 1045, (1988).

[43] Y. Martin, C. C. Williams and H. K. Wickramasinghe, "Atomic force microscope, force mapping and profiling on a 100 Å scale", J. Appl. Phys. **61**, 4723, (1987).

[44] G. Neubauer, S. R. Cohen, G. M. McClelland, D. Horne and C. Mate, "Atomic force microscopy with a bidirectional capacitance sensor", Rev. Sci. Instrum. **60**, 2296, (1990).

[45] M. Bammerlin, R. Lüthi, E. Meyer, A. Baratoff, J. Lü, M. Guggisberg, C. Loppacher, Ch. Gerber, H.-J. Güntherodt, Appl. Phys. A, **66**, s293, (1998).

[46] R. Erlanddson, L. Olsson and P. Mårtensson, Inequivalent atoms and imaging mechanisms in ac-mode atomic force microscopy of Si(111) 7×7, Phys. Rev. B **54**, R8309, (1996).

[47] B. D. Terris, J. E. Stern, D. Rugar and H. J. Mamin, "Contact electrification using force microscopy", Phys. Rev. Lett. **63**, 2669, (1989).

[48] J. N. Israelchvili and G. E. Adams," Direct measurement of long range forces between two mica surfaces in aqueous KNo_3 solutions", Nature **262**, 774, (1976).

[49] S. P. Jarvis, A. Oral, T. P. Weihs, J. b. Pethica," A novel force microscope and point contact probe", Rev. Sci. Instrum., **64**, 3515, (1993).

[50] N. A. Burnham and R. J. Colton, "Measuring the nanomechanical properties and surfaces forces of materials using an atomic force microscope", J. Vac. Sci. Technol. A **7**(4), 2906, (1989).

[51] F. Ohnesorge and G. Binnig," True atomic resolution by atomic force microscopy through repulsive and attractive forces", Science **260**, 1451, (1993).

[52] U. Dürig, J. K. Gimzewski, D. W. Pohl, "Experimental observation of forces acting during scanning tunneling microscopy", Phys. Rev. Lett. **57**, 2403, (1986).

[53] U. Dürig, O. Züger and D. W. Pohl, J. Microsc. **152**, 259, (1988).

[54] U. Dürig, O. Züger and D. W. Pohl, "Observation of metallic adhesion using the scanning tunneling microscope", Phys. Rev. Lett. **65**, 349, (1990).

[55] S. P. Jarvis, M. A. Lantz, U. Dürig, H. Tokumoto, "Off resonance ac mode force spectroscopy and imaging with an atomic force microscope", Appl. Surf. Sci. **140**, 309-313, (1999).

[56] G. Meyer and N. M. Amer, "Optical bean deflection atomic force microscopy: The NaCl(001) surface", Appl. Phys. Lett. **56**, 2100, (1990).

[57] R. Pérez, I. Štich, M. C. Payne, K. Terakura, "Surface-tip interactions in noncontact atomic-force microscopy on reactive surfaces: Si(111)", Phys. Rev. B., **58**, 10835, (1998).

[58] J. M. Soler, A. M. Baró, N. García and H. Rohrer, "Interatomic forces in scanning tunneling microscopy: Gaint corrugation of the graphite surface", Phys. Rev. Lett. **57**, 444, (1986).

[59] J. N. Israelcahvili, "Intermolecular and surface science", 2nd edition. (Academic Press, London 1991).

[60] L. Olsson, N.Lin, V. Yakimov, R. Erlandsson, " A method for in situ charactrization of tip shape in ac-mode atomic force microscopy using electrostatic interaction", J. Appl. Phys. **84**, 4060, (1998).

[61] D. Sarid, Scanning Force Microscopy, Oxford University Press, (1991).

[62] C. Schönenberger, S. F. Alvarado, "A differential interferometer for force microscopy", Rev. Sci. Instrum., **60**, 10, 3131, (1989).

[63] J. B. Pethica. Phys. Rev. Lett., "Comment on "Interatomic forces in scanning tunneling microscopy: Gaint corrugation of the graphite surface" **57**, 3235, (1986).

[64] B. J. McIntyre, P. Sautet, J. C. Dunphy, M. Salmeron, G. A. Somorjai., " Scanning tunneling microscopy tip-dependent image contrast of S/Pt(111) by controlled atom transfer", J. Vac. Sci. Technol. B, **12**, 3, 1751, (1994).

[65] L. Ruan, F. Besenbacher, I. Stensgaard, E. Laegsgaard, "Atomic resolved discrimination of chemically different elements on metal surfaces", Phys. Rev. Lett., **70**, 4079, (1993).

[66] M. T. Cuberes, R. R. Schlittler,J. K. Gimzewski, "Room-temperature repositioning of individual C_{60} molecule at Cu steps: Operation of a molecular counting device", Appl. Phys. Lett.,**69**, 3016, (1996).

[67] M. T.Cuberes, R. R. Schlittler, J. K. Gimzewski, "Room temperature supermolecular repositioning at molecular interfaces using tunneling microscope", Surf. Sci., **371**, L231, (1997).

[68] L. Bartels, G. Meyer, K.-H. Rieder, D. Velic, E. Knoesel, A. Hotzel, M. Wolf, G. Ertl, " Dynamics of electron-induced manipulation of individual Co molecules on Cu(111)", Phys. Rev. Lett., **80**, 2004,(1998).

[69] G. S. Rohrer, V. E. Heinrich, D. A. Bonnell., "A scannig tunneling microscopy and spectroscopy study of the TiO_{2-x}(110) surface", Surf. Sci., **278**, 146, (1992).

[70] E. Meyer, H. Heinzelmann, D. Brodbeck, G. Overney, R. Overney, L. Howald, H. Hug, T. Jung, H. R. Hidber, H.-J. Guntherodt. J. Vac. Sci. Technol. B, **9**, 2, 1329, (1991).

[71] F. F. Abraham, P. Batra, "Theoritical interpretation of atomic force microscope images of graphite", Surf. Sci., **209**, L125, (1989).

[72] S. R. Cohen, G. Neubauer, G. M. McClelland,"Nanomechanics of Au-Ir contact using a bidirectional atomic force microscope", J. Vac. Sci. Technol., A, **8**, 4, 3449, (1990).

[73] R. E. Bennewitz, T. Gyalog, M. Guggisberg, M. Bammerlin, E. Meyer, H.-J. Guntherodt, "Atomic-scale stick-slip processes on Cu(111)", Phys. Rev. B, **60**, R11301, (1999).

[74] A. I. Livshits, A. L. Shluger, "self-lubrication in scanning force microscope image formation on ionic surfaces", Phys. Rev. B, **56**, 12482, (1997).

[75] F. J. Giessibl, G. Binnig, "Investigation of the (001) cleavage plane of potassium bromide with an atomic force microscope at 4.2 K in ultra-high vacuum", Ultramicrosopy, **42**, 281, (1992).

[76] D. P. E. Smith, G. Binnig, C. F. Quate, "Atom point-contact imaging", Appl. Phys. Lett., **49**, 1166, (1986).

[77] H. J. Mamin, E. Ganz, D. W. Abraham, R. E. Thomson, J. Clarke, " Contamination-mediated deformation of graphite by scanning tunneling microscope", Phys. Rev. B, **34**, 9015, (1986).

[78] Y. Sugawara, M. Ohta, H. Ueyama, S. Morita, "Defect motion on an InP(110) surface observed with noncontact atomic force microscopy", Science **270**:1647 (1995).

[79] A. Schwarz, W. Allers, U. D. Schwarz, R. Wiesendanger, "the In and As sublattice on InAs(110)-(1×1) with dynamic scanning force microscopy", Appl Surf. Sci., **140**, 293, (1999).

[80] M. Bammerlin, R. Lthi, E. Meyer, A. Baratoff, J. L, M. Guggisberg, Ch. Gerber, L. Howald, H. J. Gntherodt. Probe Microscopy, 1, 3, (1997).

[81] K. Fukui, H. Onishi, Y. Iwasawa ,"Atom-resolved image of the TiO_2(110) surface by noncontact atomic force microscopy", Phys. Rev. Lett. **79**, 4202,(1997).

[82] S. Orisaka, T. Minobe, T. Uchihashi, Y. Sugawara, S. Morita, "The atomic resolution imaging of metallic Ag(111) surface by noncontact atomic force microscope", Appl. Surf. Sci., **140**, 243, (1999).

[83] C. Loppacher, M. Bammerlin, M. Guggisberg, F. Battiston, R. Bennewitz, S. Rast, A. Baratoff, E. Meyer, H.J. Gntherodt," Phase variation experiments in noncontact dynamic force microscopy usinf pase loocked loop techniques", Appl. Surf. Sci., **140**, 287, (1999).

[84] K. Kobayashi, H. Yamada, T. Horiuchi,,K. Matsushige, "Investigation of C_{60} molecules deposited on Si(111) by noncontact atomic force microscopy", Appl. Surf. Sci., **140**, 281, (1999).

[85] T. Minobe, T. Uchihashi, T. Tsukamoto, S. Orisaka, Y. Sugawara, S. Morita, "Distance dependence of noncontact-AFM image contrast on Si(1110-$\sqrt{3} \times \sqrt{3}$-Ag structure", Appl. Surf. Sci., **140**, 298, (1999).

[86] W. Allers, A. Schwarz, U. D. Schwarz, R. Wiesendanger, "Dynamic scanning force microscopy at low temperature on a van der Waals surface: graphite (0001)", Appl. Surf. Sci., **140**, 247, (1999).

[87] P. Güthner, "Simultanious imaging of Si(111)-7×7 with atomic resolution in scanning tunneling microscopy, atomic force microscopy, and atomic force microscopy noncontact mode", J. Vac. Sci. Technol. B, **14**, 2428, (1996).

[88] I. Y. Sokolov, G. S. Henderson, F. J. Wicks, "Model dependence of AFM simulations in noncontact mode", Surf. Sci., **381**, 1, L558, (1997).

[89] N. Nakagiri, M. Suzuki, K. Okiguchi, H. Sugimura, "Site discrimination of adatoms in Si(111)-(7×7) by noncontact atomic force microscopy", Surf. Sci., **373**, pL329, (1997).

[90] Y. Sugawara, H. Ueyama, T. Uchihashi, M. Ohta, Y. Yanse, T. Shigematsu, M. Suzuki, S. Morita. Mat. Res. Soc. Symp. Proc., 442, 15, (1997).

[91] H. Ö. Özer, S. O'Brien, and J. B. Pethica, "local force gradient on Si(111) during simultaneous scanning tunneling/atomic force microscopy", Appl. Phys. Lett., **90**, 133110 (2007).

[92] J. Chen, R. J. Hamers, "Role of atomic force in tunneling-barrier measurements" J. Vac. Sci. Technol. B, **9**, 2, 503,(1991).

[93] S. Ciraci, "Atomic-scale tip-sample interactions and contact phenomena", Ultramicroscopy, **42**, 16, (1992).

[94] A. H. R. Clarke, J. B. Pethica, J. A. Nieminen, F. Besenbacher, E. Lgsgaard, I. Stensgaard., " Quantitative scanning tunneling microscopy at atomic resolution: influence of forces and tip configuration", Phys. Rev. Lett., **76**, 1276, (1996).

[95] N.A. Burnham, R. J. Colton,"Measuring the nanomechanical properties and surface forces of meterials using an atomic force microscope", J. Vac. Sci. Technol. A, 7, 4, 2906, (1989).

[96] S. P. Jarvis, H. Yamada, S.-I. Yamamoto, H. Tokumoto, , J. B. Pethica, "Direct mechanical measurement of interatomic potential", Nature, **384**, 247, (1996).

[97] G. Cross, A. Schirmeisen, A. Stalder, P. Grtter, M. Tschudy, U. Drig., "Adhesion interaction between atomically defined tip and sample", Phys. Rev. Lett., **80**, 4685, (1998).

[98] B. Gotsmann, B. Anczykowski, C. Seidel, H. Fuchs, "Determination of tip-sample interaction forces from measured dynamic force spectroscopy curves", Appl. Surf. Sci., **140**, 3-4, 314, (1999).

[99] A.W. Dunn, P. Moririty, P. H. Beton," Nanometer scale patterning of C_{60} multilayers using molecular manipulation, Journal of Vacuum Science and Technology", Part A Vacuum, Surfaces and Films, **15(3)**, 1478, (1997).

[100] Y. Sugimoto, M. Abe, S. Hirayama, N. Oyabu, O. Custance, and S. Morita, "Atom inlays performed at room temprature using atomic force microscopy", Nature Mat., **4**, 156 (2005).

[101] E. Gnecco, R. Bennewitz, T. Gyalog,Ch. Loppacher, M. Bammerlin, E. Meyer and H. J. Güntherodt, "Velocity dependence of atomic friction", Phys. Rev. Lett. **84**, 1172, (2000).

[102] L. Howald, E. Meyer, R. Lüthi,H. Haefke,R. Overney,H. Rudin and H. J. Güntherodt, "Multifunctional probe microscope for facile operation in ultrahigh vacuum", Appl. Phys. Lett., **63**, 117, (1993).

[103] L. Howald, R. Lüthi, E. Meyer, G. Gerth,H. Haefke, R. Overney and H. J. Güntherodt, "Friction force microscopy on clean surfaces of NaCl, NaF, and AgBr", J. Vac. Sci. Technol. B, **12**, 2227, (1994).

[104] R. Lüthi, E. Meyer, H. Haefke, L. Howald, W. Gutmannsbauer, M. Guggisberg, M. Bammerlin and H. J. Güntherodt, " Nanotribology: An UHV-SFM study on thin films of C_{60} and AgBr", Surf. Sci. **338**, 247, (1995).

[105] R. Lüthi, E. Meyer, M. Bammerlin,L. Howald, H. Haefke,T. Lehmann, C. Loppacher, H. J. Güntherodt, T. Gyalog and H. Thomas, " " , J. Vac. Sci. Technol. B, **14**, 1280, 1996

[106] R. Bennewitz, E. Gnecco, T. Gyalog and E. Meyer," Atomic friction studies on well-defined surfaces",Tribol. Lett., **10**, 51, (2001).

[107] M. R. Sorensen, K. W. Jacobsen and P. Stoltze, "Simulations of atomic-scale sliding friction", Phys. Rev. B, **53**, 2101, (1996).

[108] G. J. Germann, S. R. Cohen, G. Neubauer,G. M. McClelland and H. Seki, "Atomic scale friction of a diamond tip on diamond (100) and (111) surface", J. Appl. Phys. **73** 163,(1993).

[109] R. J. A. van den Oetelaar and G. F. J. Flipse, "Atomic scale friction on diamond(111) studied by ultra-high vacuum atomic force microscopy", Surf. Sci., **384**, L828,(1997).

[110] S. Fujisawa, E. Kishi, Y. Sugawara and S. Morita, "Atomic-scale friction observed with a two-dimensional fritional-force microscope", Phys. Rev. B, **51**, 7849, (1995).

[111] S. Morita, S. Fujisawa and Y. Sugawara, "Spatially quantized friction with a lattice periodicity", Surf. Sci. Rep., **23**, 3, (1996).

[112] T. Gyalog, M. Bammerlin, R. Lüthi, E. Meyer and H. Thomas, "Mechanism of atomic friction ", Europhys. Lett., **31**, 269, (1995).

[113] H. Kawakatsu and T. Saito, "Scanning force microscopy with two optical levers for detection of deformations of the cantilever", J. Vac. Sci. Technol. B, **14**, 872, (1996).

[114] T. Bouhacina,J. P. Aimé, S. Gauthier, D. Michel and V. Heroguez, "Tribological behavior of a polymer grafted on silanized silica probed with a nanotip", Phys. Rev. B, **56**, 7694, (1997).

[115] O. Zwörner, H. Hölscher,U. D. Schwarz and R. Wiesendanger, " The velocity dependence of friction forces in point contact friction", Appl. Phys. A, **66**, S263, (1998).

[116] M. Hirano, K. Shinjo, R. Kaneko and Y. Murata, "Anisotropy of frictional forces in muscovite mica", Phys. Rev. Lett.,**67** 2642, (1991).

[117] R. M.Overney,H. Takano, M. Fujihira,W. Paulus and H. Ringsdorf, "Ansiotropy in friction and molecular stick-slip motion", Phys. Rev. Lett., **72** 3546, (1994).

[118] H. Takano and M. Fujihira,"Study of molecular scale friction on stearic acid crystal by friction force microscopy", J. Vac. Sci. Technol. B, **14**, 1272, (1996).

[119] M. Liley, D. Gourdon, D. Stamou, U. Meseth Meseth, T. M. Fischer,C. Lautz, H. Stahlberg, H. Vogel,N. A. Burnham and C. Duschl, "Friction anisotropy of a comliant monolayer induced by a small molecular tilt", Science, **280**, 273, (1998).

[120] P. E. Sheehan and C. M. Lieber, "Nanotribology and nanofabrication of MoO_3 structure by atomic force microscopy", Science, **272**, 1158, (1996).

[121] M. R. Falvo,R. M. Taylor, A. Helser, V. Chi, F. P. Brooks, S. Wahburn and R. Superfine, " ", Nature, **397**, 236, (1999).

[122] M. R. Falvo, J. Steele, R. M. Taylor and R. Superfine, "Evidence of commensurate contact and rolling motion: AFM manipulation stdies of carbon nanotubes on HOPG",Tribol. Lett., **9**, 73, (2000).

[123] A. L. Weisenhorn, P. Maivald,H. J. Butt and P. K. Hansma. "Measuring adhision, attraction, and repultion between surfaces in liquid with an atomic force microscope,Phys. Rev. B., **45**, 11226, (1992).

[124] M. Binggeli and C. M. Mate, "influence of capillary condensation of water on nanotribology studied by force microscopy", Appl. Phys. Lett., **65**, 415,(1994).

[125] F. G. Giessibl, M. Herz,J. Manhart, "Friction traced to the single atom", PNAS, **99**, 12006 (2002).

[126] O. Pfeiffer, R. bennewitz, A. Baratoff, and E. Meyer, "Lateral force measurement in dynamic force microscopy", Phys. Rev. B,**65**, 161403, (2002).

[127] S. Kawai, S. Kitamura, D. Kobayashi, H. Kawakatsu, "Dynamic lateral force microscopy with true atomic resolution", Appl. Phys. Lett., **87**, 173105, (2005).

[128] Nanomagnetics Instrument Limited, Sutie 290, 266 Banbury Road, Oxford OX2 7DL, UK.

[129] Staveley Sensors Inc. EBL#2, Stevely Sensors Inc., 91 Prestige Park Circle, East Hartford, CT 06108, USA.

[130] D. Rugar, H. J. Mamin, and P. Guethner,"Improved fiber-optic interferometer for atomic force microscopy ", Appl. Phys. Lett., **55**, 2588, (1989).

[131] H. Ö. Özer, Ph.D. Thesis, Bilkent University, (2001).

[132] ILFORD PQ Universal Photographic film developer.

[133] EPOTEK H21D Conductive adhasive.

[134] F. J. Giessibl, M. Tortonese, "Self-oscillation mode for frequency odulation noncontact atomic force microscopy", Appl. Phys. Lett. **70**, 2529 (1997).

[135] J. P. Cleavland, B. Anczykowski, A. E. Schmid, V. B. Elings, "Energy dissipation in tapping-mode atomic force microscopy", Appl. Phys. Lett. **72**, 2613 (1998).

[136] Ch. Loppacher, M. Guggisberg, O. Pfeiffer, E. Meyer, M. Bammerlin, R. Lüti, R. Schlittler, J. K. Gizewski, H. Tang, C. Jachim," Direct determination of energy required to operate a single molecule switch", Phys, Rev. Lett., **90**, 66107, (2003).